


This is to certify that the
dissertation entitled

Nonlinear imaging with femtosecond laser pulses

presented by

Yves Coello

has been accepted towards fulfillment
of the requirements for the

Doctoral degree in Chemistry

Major Professor's Signature

6-17-10

Date

NONLINEAR IMAGING WITH FEMTOSECOND LASER PULSES

By

Yves Coello

A DISSERTATION

Submitted to
Michigan State University
in partial fulfillment of the requirements
for the degree of

DOCTOR OF PHILOSOPHY

Chemistry

2010

ABSTRACT

NONLINEAR IMAGING WITH FEMTOSECOND LASER PULSES

By

Yves Coello

The high peak powers delivered by femtosecond laser pulses easily induce nonlinear optical processes which are useful for a variety of applications, including biological imaging. This dissertation presents various contributions to the development of nonlinear imaging with femtosecond laser pulses.

The spectral phase distortions that femtosecond laser pulses suffer due to dispersion as they transmit through microscope objectives have hindered the application of sub-50 fs pulses in nonlinear imaging. Here, accurate spectral phase characterization of such pulses was accomplished using multiphoton intrapulse interference phase scan (MIIPS). As a result, pulse compression to the theoretical transform-limited duration at the focal plane was demonstrated, including the challenging case of 4.3 fs pulses. These MIIPS developments will allow taking advantage of sub-50 fs pulses for nonlinear imaging. In addition, dispersion measurements of optical media with unprecedented accuracy were obtained using MIIPS. This information is critical for pulse propagation models.

Two-photon spectra of fluorescent dyes are necessary for the most popular nonlinear imaging method, two-photon laser scanning fluorescence microscopy. In this dissertation, a fast and automated approach able to measure two-photon spectra of fluorophores by pulse shaping ultrabroad-bandwidth femtosecond laser pulses is demonstrated. The approach is particularly valuable given that it is suitable for non-laser expert use.

Finally, direct non-resonant femtosecond laser desorption and ionization were applied in the development of a new atmospheric pressure mass-spectrometric imaging approach using amplified femtosecond pulses. These results, which show unprecedented spatial resolution, open new possibilities for the use of femtosecond laser pulse in biological imaging.

ACKNOWLEDGEMENTS

The work presented here is the result of a learning process that has been greatly enriched through interactions with many people that shared with me their experience and knowledge and offered me their help and support. First of all, I want to thank my advisor Prof. Marcos Dantus for providing me with interesting and challenging research projects, offering me useful suggestions through frequent scientific discussions and financially supporting me during my graduate studies. I am also thankful to the members of my committee, Profs. John McCracken, James McCusker and Katharine Hunt for their time and advice. I also want to thank past and present members of the Dantus research group: Dr. Vadim Lozovoy, Dr. Igor Pastirk, Dr. Tissa Gunaratne, Dr. Haowen Li, Dr. D. Ahmasi Harris, Dr. Dmitry Pestov, Dr. Bingwei Xu, Dr. Scott Smith, Jess Gunn, Xin Zhu, Paul Wrzesinski, Christine Kalcic, and Marshall Bremer. The regular interaction with them in group meetings, conferences, labs and offices has represented a continuous learning experience. Especially, I would like to thank Vadim for his endless suggestions and his lucid perspective. I am also very grateful to Bingwei, with whom I was fortunate to start working with when I just entered the group. He was very kind and patient answering innumerable questions about femtosecond lasers, optics and pulse shapers at that time. As a result of a fruitful collaboration, Vadim, Bingwei and I coauthored a number of research publications. I was also very lucky to have the advice of two mass spectrometry experts,

Profs. A. Daniel Jones and Gavin Reid. In particular, help and suggestions provided by Prof. Jones were critical for the progress of the imaging mass spectrometry project, which I concentrated on during the last years of my graduate studies. I would also like to thank the College of Natural Sciences for providing me the Dissertation Completion Fellowship in the summer of 2010.

TABLE OF CONTENTS

LIST OF TABLES

LIST OF FIGURES

LIST OF ABBREVIATIONS

BP	Binary phase
CPA	Chirped pulse amplification
CR	Contrast ratio
FROG	Frequency resolved optical gating
GDD	Group delay dispersion
GVD	Group velocity dispersion
HPTS	8-hydroxypyrene-1,3,6-trisulfonic acid
KDP	Potassium dihydrogen phosphate
LC	Liquid crystal
MII	Multiphoton intrapulse interference
MIIPS	Multiphoton intrapulse interference phase scan
NA	Numerical aperture
Nd:YVO_4	Neodymium doped yttrium vanadate
NLO	Nonlinear optical
SHG	Second-harmonic generation
SLM	Spatial light modulator
S/N	Signal-to-noise ratio
SPIDER	Spectral phase interferometry for direct electric-field reconstruction

Ti:Sa	Titanium-doped sapphire
TL	Transform-limited
TPA	Two-photon absorption
TPE	Two-photon fluorescence excitation
TPLSM	Two-photon laser scanning fluorescence microscopy (TPLSM)

Introduction

Ultrashort pulse generation has progressed significantly during the last decades. Commercial NIR (near-infrared) femtosecond laser systems are now able to generate pulses with typical time durations in the range 10-100 fs. Their inherent brevity makes these pulses useful to study the atomic-scale dynamics of molecular systems [1]. The average power that a femtosecond laser beam carries is actually concentrated in the femtosecond time duration of the pulses constituting the pulse train. As a consequence, femtosecond laser pulses give rise to extremely high peak powers, which typically fall in the range 10^4-10^6 W for a non-amplified system. When such a laser beam is focused, peak power densities of 10^9-10^{12} W/cm^2 are obtained at the focal plane. These peak power densities are high enough to generate nonlinear optical (NLO) processes that are useful for many applications, including biological imaging. For instance, two-photon absorption (TPA) and second harmonic generation (SHG), which were the first two NLO processes experimentally demonstrated [2, 3], are used today in second-harmonic imaging microscopy [4] and two-photon laser scanning fluorescence microscopy (TPLSM) [5], respectively.

In theory, the use of shorter femtosecond pulses should be advantageous because the nonlinear signal intensity is inversely related to the time duration of the pulses. For instance, for two-photon processes such as two-photon induced fluorescence and SHG, the signal is inversely proportional to the time duration of the pulses given a fixed pulse energy. Even though laser systems generating 10 fs pulses have been commercially available for several years, most multiphoton imaging experiments still employ ~100 fs

pulses [6] because the expected advantages of using shorter pulses, including a 10X increase in signal, have not been experimentally realized until recently [7]. This phenomenon is due to the fact that shorter pulses have a broader spectral bandwidth and thus suffer higher chromatic dispersion that significantly increases their duration after travelling through optical materials such as the microscope objective required to focus the beam. Part of this dissertation (Chapter 3) helps remedy this problem by demonstrating accurate pulse characterization and compression. A related task, the accurate measurement of dispersive properties of optical media, was also demonstrated (Chapter 4). Both contributions will allow exploiting the advantages of using sub-50 fs pulses in nonlinear imaging.

TPLSM, first demonstrated in 1991, is by far the most popular biological imaging technique taking advantage of NIR femtosecond laser pulses. In TPLSM the focused laser beam is scanned across the sample to successively analyze different sample positions. The fluorophores present in the focal volume become excited after two-photon absorption and finally emit fluorescence, which is recorded as a function of position. The corresponding image is then built by plotting the fluorescence intensity as a function of position for one or more fluorophores. The two-photon fluorescence excitation (TPE) spectra of dyes commonly used in TPLSM have been measured in the past years. However, such experiments required the use of complicated optical setups that require the presence of a laser expert [8, 9]. The increasing use of TPLSM in medical and biological research demands the characterization of newly developed dyes. Furthermore, researchers synthesizing new fluorophores would benefit from the availability of a fast and automated method able to measure TPE spectra, suitable for non-laser-expert use.

For these reasons, part of this work concentrates on the development of such a method (Chapter 5).

Amplified femtosecond laser systems offer substantially higher pulse energies. A focused beam from a commercial amplified system generates peak power densities higher than 10^{13} W/cm^2, which are enough to ablate and ionize molecules from surfaces. Part of this dissertation (Chapter 6) explores the use of amplified femtosecond pulses for atmospheric pressure mass spectrometry imaging, which allows obtaining chemically resolved images of a variety of samples.

The dissertation is organized as follows. Chapter 1 briefly presents fundamental concepts that are present throughout the dissertation. The content of this chapter is intended to provide a better understanding of the subsequent chapters, especially for readers unfamiliar with femtosecond laser pulses, nonlinear optical processes and the spectral phase. Chapter 2 presents the main experimental tools employed for this work: femtosecond laser systems, pulse shapers and the phase measurement and correction method multiphoton intrapulse interference phase scan (MIIPS). Chapter 3 demonstrates accurate pulse characterization and compression results obtained with MIIPS, including the challenging compression of sub-5fs pulses. Chapter 4 presents MIIPS dispersion measurements of optical media with unprecedented accuracy. Chapter 5 demonstrates a fast and automated method able to measure TPE spectra of fluorophores by pulse shaping ultrabroad-bandwidth femtosecond laser pulses. Finally, Chapter 6 presents the use of femtosecond laser desorption ionization for mass spectrometry imaging at ambient conditions with unprecedented spatial resolution.

Chapter 1

Preliminary concepts

A number of important definitions appearing throughout this dissertation will be introduced in the following sections.

1.1 Ultrashort laser pulses and spectral phase

An ultrashort laser pulse is constituted by a number of optical frequencies. The time duration and frequency bandwidth of a pulse are related by the time-bandwidth product, which states that $\Delta t\ \Delta\nu \geq K$, where Δt and $\Delta\nu$ are the full width at half maximum (FWHM) of the temporal intensity and spectrum, respectively, and K is a constant that depends on the shape of the temporal intensity [10]. What determines how large $\Delta t\ \Delta\nu$ is with respect to K is the spectral phase of the pulse, which will be described soon.

Mathematically, an ultrashort pulse can be defined by its electric field $\varepsilon(t)$, which is a real quantity. However, the frequency domain description of a pulse will be used extensively in this dissertation. The frequency domain electric field of the pulse is defined as the Fourier transform of $\varepsilon(t)$,

$$\varepsilon(\omega) = |\varepsilon(\omega)|\exp[i\varphi(\omega)] \equiv \int_{-\infty}^{+\infty} \varepsilon(t)\exp[i\omega t]dt, \qquad (1.1)$$

where $\varphi(\omega)$ is the spectral phase. $\varepsilon(\omega)$ typically has nonzero regions for both positive and negative frequencies. Both regions contain equivalent information because $\varepsilon(t)$ is real. In fact, $\varepsilon(\omega)=\varepsilon^*(-\omega)$ where the asterisk indicates complex conjugate. It is convenient to define $E(\omega)\equiv\varepsilon(\omega)$ for $\omega\geq 0$ and $E(\omega)\equiv 0$ everywhere else. The inverse Fourier transform of $E(\omega)$ is

$$\frac{1}{2\pi}\int_{-\infty}^{+\infty} E(\omega)\exp[-i\omega t]d\omega \equiv E(t). \qquad (1.2)$$

$E(t)$ is not a real function because we eliminated the nonzero negative frequency region in $E(\omega)$. However the real field $\varepsilon(t)$ can be obtained from $E(t)$ using the equation $E(t)+E^*(t)=\varepsilon(t)$. $E(\omega)$ and $E(t)$ are the functions that will be used for the rest of this dissertation.

The temporal intensity of the pulse $I(t)$ is proportional to the squared magnitude of $E(t)$. So, if we only care about the shape of $I(t)$ we can write,

$$I(t) = |E(t)|^2. \qquad (1.3)$$

Similarly, the spectrum or spectral intensity of the pulse $S(\omega)$ is directly proportional to the squared magnitude of $E(\omega)$. So, we can write

$$E(\omega) = \sqrt{S(\omega)}\exp[i\varphi(\omega)], \qquad (1.4)$$

which provides the electric field $E(\omega)$ in terms of the spectrum $S(\omega)$ and the spectral phase $\varphi(\omega)$. While the magnitude of $E(\omega)$ can be easily measured with a spectrometer, the spectral phase has been traditionally much more difficult to measure. This interesting issue will be discussed in section 2.3. Note that according to Equation 1.4, the spectrum and the spectral phase together are sufficient to completely characterize an ultrashort pulse.

The spectral phase is the relative phase that different frequency components of the pulse carry. A variation in $\varphi(\omega)$ is directly reflected in the temporal intensity of the pulse, as will be illustrated in the next section. It can be shown that for a given spectrum the pulse achieves its minimum time duration when $\varphi(\omega)$ is a linear function of frequency.

Such a pulse is called transform-limited (TL). For a TL pulse, the equality in the time bandwidth product is satisfied ($\Delta t\ \Delta \nu = K$).

Spectral phase distortions are introduced by dispersion [11]. Material dispersion is the most usual and well-known class of dispersion and occurs because the refractive index of materials is frequency-dependent. As a consequence, different frequency components of a laser pulse travel with different velocities and the pulse changes its temporal intensity as it propagates through the medium. A more detailed discussion about material dispersion and its measurement will be presented in chapter 4. Material dispersion introduces mainly quadratic phase distortions, which correspond to a linear variation of frequency with time. In this case, the pulse is said to be linearly chirped. Higher-order (>2) spectral phase distortions introduced by material dispersion become more important as the pulse duration decreases (<50 fs). Spectral phase distortions are introduced by material dispersion in the laser system itself as well as by propagation of the laser pulse through different optical elements present in the experimental setup such as lenses, microscope objectives, filters, beamsplitters and cuvettes. Introducing or changing any of these elements from the optical setup affects the spectral phase of the pulses and therefore the outcome and reproducibility of an experiment unless a method able to characterize and correct the spectral phase distortions is used. Multiphoton intrapulse interference phase scan (MIIPS), which will be described in section 2.3, is a method useful for such purpose. MIIPS is based on multiphoton intrapulse interference.

1.2 Multiphoton intrapulse interference (MII)

Nonlinear optical (NLO) processes depend on the spectral phase of the laser pulses that generated them. By NLO processes we refer here to multiphoton excitation of

chemical systems (e.g. two-photon absorption in molecules) or to generation of nonlinear optical signals in optical media (e.g. second-harmonic generation, SHG, in a crystal). The dependence of NLO processes on the spectral phase was recognized in a number of studies thanks to the development of pulse shaping techniques, which allow controlling the amplitude and phase of ultrashort pulses (section 2.2). In 1992, amplitude modulation and different amounts of chirp (quadratic spectral phase modulation) were used to manipulate the SHG spectrum of the laser pulses and two-photon absorption in Rb atoms [12, 13]. Control of two-photon transitions in Cs atoms was demonstrated using a step spectral phase function (π jump) in 1998 [14, 15]. This observation was explained in terms of constructive or destructive interference between pairs of frequencies within the bandwidth of the laser, which depended on the spectral phase of the pulses, that determined the multiphoton transition probability (by enhancing or supressing it) at a particular frequency corresponding to the transition. The Dantus group realized that the spectral phase modulates the probability for NLO processes at all frequencies in the n^{th}-order nonlinear spectrum of the pulses $S^{(n)}(\omega)$, where n is the order of the NLO process being considered. They demonstrated control of two- and three-photon transitions in large molecules in solution and control of the SHG spectrum with sinusoidal spectral phases [16]. The phenomenon was named MII and was further studied in subsequent papers [17, 18].

To understand MII let us consider SHG, a two-photon optical process relevant for MIIPS. In SHG, an input wave interacting with a nonlinear medium, typically a crystal, generates an output wave with twice the optical frequency (thus, SHG is also known as frequency doubling). An ultrashort pulse contains a number of different frequencies and

thus different pathways exist for the frequency doubling process. In general, a pair of photons with frequencies $\omega - \Omega$ and $\omega - \Omega$, where Ω is a frequency detuning, can combine and generate a photon at frequency 2ω. Mathematically, The SHG spectrum $S^{(2)}(2\omega)$ is given by

$$S^{(2)}(2\omega) \propto \left| \int E(\omega+\Omega) E^{*}(\omega-\Omega) d\Omega \right|^2 \qquad (1.5),$$

where $E(\omega)$ is the field of the pulses [17]. Multiple different frequency pairs $\omega - \Omega$ and $\omega - \Omega$ in the spectrally broad pulses provide multiple pathways that give rise to interference. This interference is accounted for by integration over all possible Ω. All three words in MII are essential: it is the interference of the field with itself (intrapulse) taking place in a multiphoton process. To make evident that such interference depends on the spectral phase we can rewrite $E(\omega)$ in terms of its amplitude and phase and obtain

$$S^{(2)}(2\omega) \propto \left| \int \left| E(\omega+\Omega) \right| \left| E(\omega-\Omega) \right| \exp\left[i\left(\varphi(\omega+\Omega) + \varphi(\omega-\Omega) \right) \right] d\Omega \right|^2 \qquad (1.6).$$

Figure 1.1 illustrates the MII process for SHG. In the left panel the spectral phase $\varphi(\omega)$ is constant (TL pulse). Consequently, for any frequency ω in the bandwidth of the pulse the complex exponential term in Equation 1.6 is constant and all frequency pairs interfere constructive to maximize the SHG spectrum $S^{(2)}(2\omega)$. In the right panel, the spectral phase $\varphi(\omega)$ is a sine function with its inversion center at ω_1. Therefore, the complex exponential term in Equation 1.6 is constant for all frequency pairs around ω_1 and all frequency pairs around ω_1 interfere constructive to maximize the SHG spectrum $S^{(2)}(2\omega)$ at $2\omega_1$. In contrast, for any other frequency $\omega_2 \neq \omega_1$ the exponential term in

Equation 1.6 is frequency dependent and different degrees of destructive interference take place giving rise to low signal.

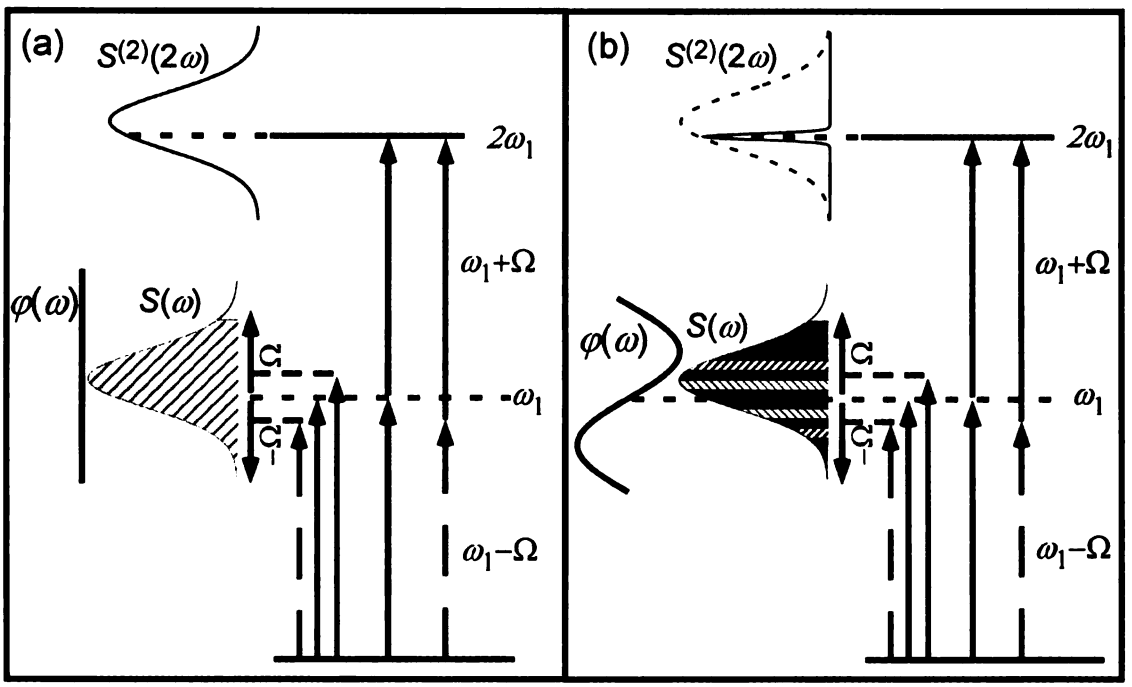

Figure 1.1. Multiphoton intrapulse interference for SHG. (a) illustrates MII for the case of a TL pulse, with a constant spectral phase $\varphi(\omega)$. Frequency pairs (ω_1,ω_1) and $(\omega_1-\Omega, \omega_1+\Omega)$ in the fundamental spectrum $S(\omega)$ interfere constructively to produce maximum intensity in the SHG spectrum $S^{(2)}(2\omega)$ at $2\omega_1$. Constructive interference occurs for any frequency ω_1 within the bandwidth of the pulse because all frequency pairs are in phase. As a consequence the SHG signal is maximized for all frequencies and the spectrum $S^{(2)}(2\omega)$ shown at the top is obtained. The uniform filling under $S(\omega)$ indicates that the spectral phase is constant. Note that frequencies in the unfilled part of the spectrum do not contribute to the signal at $2\omega_1$ because no frequencies in the lower frequency part of the spectrum can pair with them. (b) illustrates MII for a sinusoidal spectral phase $\varphi(\omega)$ with its inversion center at ω_1. In this case, frequency pairs (ω_1,ω_1) and $(\omega_1-\Omega, \omega_1+\Omega)$ in the fundamental spectrum $S(\omega)$ interfere constructively to produce maximum intensity in the SHG spectrum $S^{(2)}(2\omega)$ at $2\omega_1$. For any other frequency $\omega_2 \neq \omega_1$ the SHG is not maximized because destructive interference takes place. As a consequence the spectrum $S^{(2)}(2\omega)$ shown at the top is obtained. Note that the sum of the phases of frequency pairs under $S(\omega)$ which show the same pattern is a constant. Thus, constructive interference takes place at ω_1.

Let us now consider the effect of simple spectral phases on the SHG spectrum and the temporal intensity of a pulse. A linear phase function only advances or delays a pulse in time, but it does not have any effect on the SHG spectrum. The effect of quadratic, cubic and sinusoidal spectral phases is simulated in Figure 1.2. The fundamental spectrum (same for all cases) and phase are shown in the left column, the simulation of the temporal intensity of the pulses *I(t),* calculated using Equation 1.3, is shown in the center column, and the SHG spectrum is shown in the right column. The SHG spectra were simulated using

$$S^{(2)}(\omega) = \left| \int E^2(t) \exp[i\omega t] dt \right|^2, \qquad (1.7)$$

which allows to calculate the SHG spectrum by Fourier transforming $E^2(t)$ [19]. The thin lines in the center and right columns correspond to the TL case and are shown for comparison. A quadratic spectral phase (or chirp, Figure 1.2a) temporally broadens the pulse and reduces the intensity of $S^{(2)}(2\omega)$ without changing its shape. A cubic spectral phase (Figure 1.2b) temporally broadens the pulse and creates subpulses. It has a significant effect on the shape of $S^{(2)}(2\omega)$ and generates a maximum in the spectrum that reaches the intensity of the TL case at the frequency corresponding to inversion center of the phase. The intensity at other frequencies is relatively low. A sinusoidal spectral phase (Figure 1.2c) has an effect similar to that of a cubic phase. However, given that it does not diverge toward infinity its experimental implementation is easier (a cubic phase may require extremely high retardations at the edges of the spectrum). Again, the maximum in $S^{(2)}(2\omega)$ occurs at the frequency corresponding to inversion center of the phase and the signal is minimized elsewhere. In contrast, TL pulses maximize SHG (and any NLO

process) at all frequencies, but without any selectivity. MII principles have been used to design shaped pulses able to control NLO processes [19].

In general, any spectral phase with inversion center at ω will generate SHG signal as intense as the corresponding to a flat phase (TL case) at frequency 2ω in a similar way to the sinusoidal and cubic spectral phases described before. However, an approximation that will become useful later states that the condition $\varphi''(\omega)=0$ is enough to have a maximum at 2ω. In fact, if we make a Taylor series expansion of the phases at positive and negative detuning in Equation 1.6 we obtain

$$\varphi(\omega+\Omega)=\varphi(\omega)+\varphi'(\omega)\Omega+\tfrac{1}{2}\varphi''(\omega)\Omega^2+\tfrac{1}{6}\varphi'''(\omega)\Omega^3+\ldots \qquad (1.8)$$

$$\varphi(\omega-\Omega)=\varphi(\omega)+\varphi'(\omega)(-\Omega)+\tfrac{1}{2}\varphi''(\omega)(-\Omega)^2+\tfrac{1}{6}\varphi'''(\omega)(-\Omega)^3+\ldots \qquad (1.9)$$

Therefore,

$$\varphi(\omega+\Omega)+\varphi(\omega-\Omega)=2\varphi(\omega)+\varphi''(\omega)\Omega^2+\ldots \qquad (1.10)$$

According to Equation 1.6, $S^{(2)}(2\omega)$ is maximized when $\varphi(\omega+\Omega)+\varphi(\omega-\Omega)$ is constant. Equation 1.10 states that $\varphi(\omega+\Omega)+\varphi(\omega-\Omega)$ is a constant when $\varphi''(\omega)=0$, if we ignore terms of even order $n\geq 4$. Therefore, to first approximation, $S^{(2)}(2\omega)$ is maximized when $\varphi''(\omega)=0$.

The simulations shown in Figure 1.2 illustrate the fact that the spectral phase has a critical effect on the outcome of NLO processes. For this reason, a method able to characterize and correct the spectral phase distortions of femtosecond laser pulses at the target position is necessary to achieve optimal and reproducible experimental results. MII principles have been the basis for the development of such a method (section 2.3).

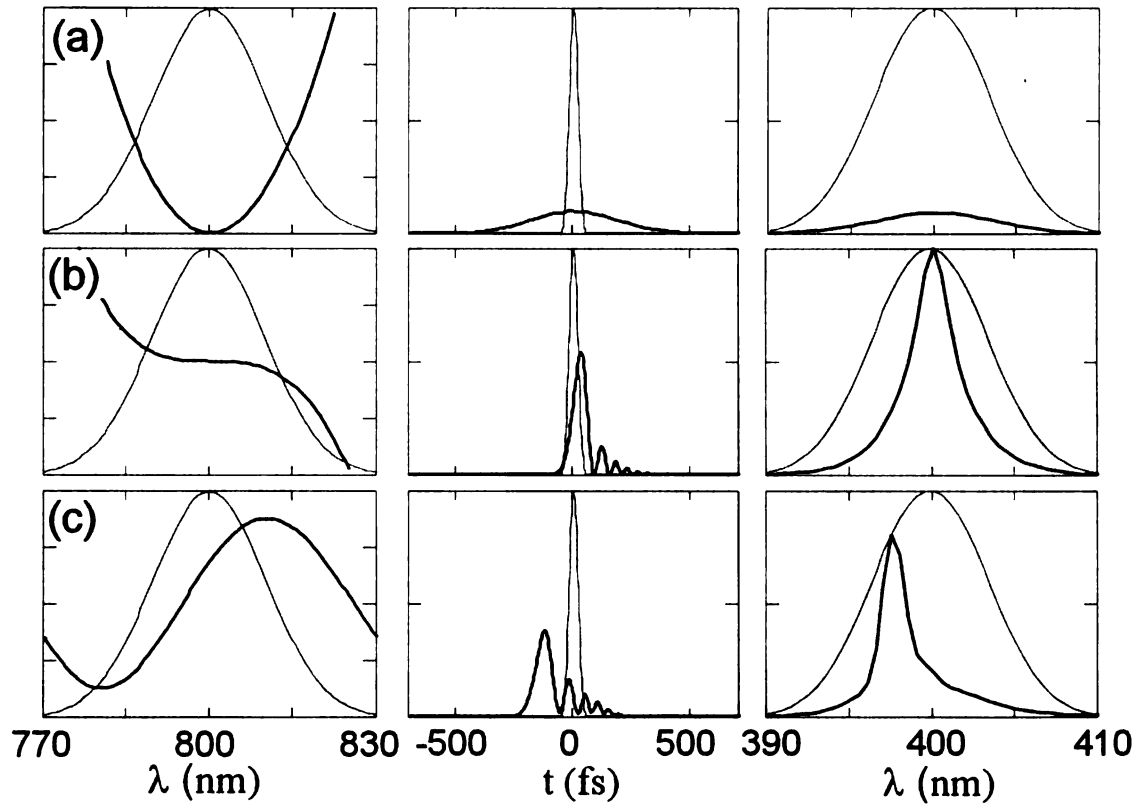

Figure 1.2. Effect of the spectral phase on the temporal intensity and the SHG spectrum of a pulse. The left column shows the spectrum (thin line) and spectral phase of the pulse (thick line). The center and right columns show simulations of the temporal intensity and SHG spectrum of the pulse (thick line). Simulations for the TL case are shown for comparison (thin lines). (a) A quadratic spectral phase broadens the pulse and reduces the SHG spectral intensity without altering the spectral shape. (b) A cubic spectral phase broadens the pulse and creates subpulses, and alters the SHG spectral shape creating a maximum at the frequency corresponding to inversion center of the phase. (c) A sinusoidal spectral phase has an effect similar to a cubic phase. The spectral phase functions simulated were $\varphi(\omega)=3000\text{fs}^2(\omega-\omega_0)^2$, $\varphi(\omega)=16667\text{fs}^3(\omega-\omega_0)^3$, and $\varphi(\omega)=1.5\pi\cos[35\text{fs}(\omega-\omega_0)+\pi/3]$, respectively, where ω_0 is the center frequency of the spectrum.

Chapter 2

Experimental Tools

2.1 Femtosecond laser systems

The first sub-picosecond laser pulses were produced in the mid-1970's using organic dyes as the gain medium [20], more than a decade after the first experimental demonstration of the laser [21]. These dye-lasers dominated ultrashort pulse generation research until the late 1980's and achieved their shortest pulse duration of 6 fs after external pulse compression in 1987, a world record not surpassed for about 10 years [22]. The dominance of dye lasers ended soon after the discovery of Titanium-doped sapphire (Ti^{3+}:Al_2O_3), usually abbreviated as Ti:Sa, a new solid-state laser material that had the necessary broad gain bandwidth to support femtosecond laser pulses and provided long term stability, unlike the dye-based laser systems that preceded it [23]. Since the early 1990's ultrashort pulse generation with Ti:Sa lasers has progressed significantly [24]. Pulses as short as 5 fs have been produced directly from a Ti:Sa laser oscillator with dispersion compensating mirrors in 2001 [25], and with external compression these pulses reached the world record duration of 4.3 fs in 2005 [26]. Even until today, no other laser material has produced pulses shorter than 6 fs.

Two different Ti:Sa femtosecond lasers systems, which are described in the following sections, were employed for the experiments presented in this dissertation.

2.1.1 Ultrabroad-bandwidth Ti:Sa femtosecond laser oscillator

This is a commercial laser system (Venteon Pulse 1, Nanolayers GmbH) whose design is based on the Ti:Sa oscillator with dispersion compensating mirrors mentioned earlier [25]. Intracavity temporal pulse broadening is controlled by a combination of

chirped mirrors and a BaF_2 wedge pair. This system, pumped by a Nd:YVO_4 laser (Verdi-5, Coherent), generates ~1 nJ laser pulses at 78 Mhz with a spectrum spanning more than 400 nm (from 620 to 1050 nm). This frequency bandwidth is broad enough to support a time duration of 4.3 fs. Figure 1.1 shows a scheme of the laser oscillator setup.

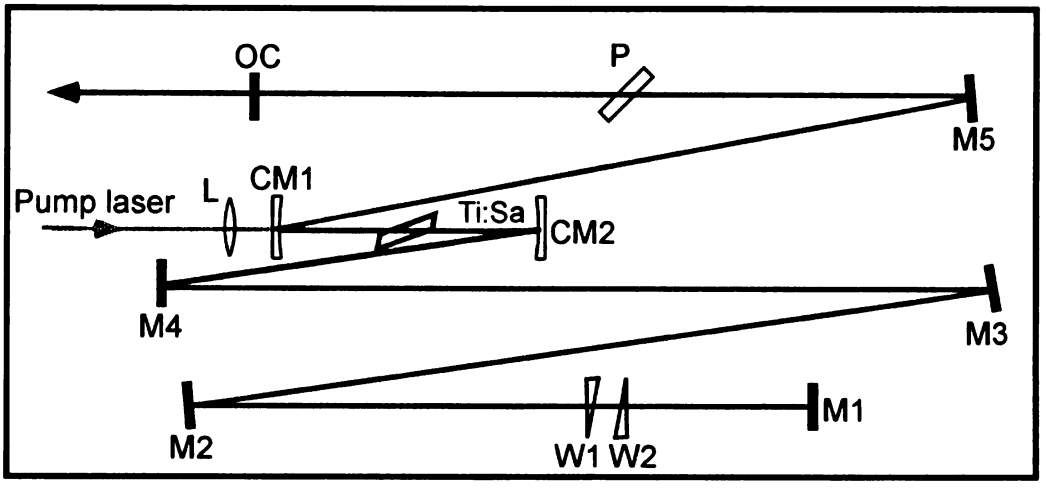

Figure 2.1. Ultrabroad-bandwidth Ti:Sa femtosecond laser oscillator setup. L: lens, CM1 and CM2: curved dispersion compensating mirrors, M1-M5: dispersion compensating mirrors, Ti:Sa: Ti:Sa crystal, W1- W2: dispersion compensating BaF_2 wedges, P: BaF_2 plate, and OC: output coupler.

After external pulse compression, as described in section 3.2, 4.3 fs pulses were produced with this laser system matching the shortest pulse duration ever obtained directly from a laser oscillator [27]. These compressed pulses were then used for the experiments reported in chapters 4 and 5.

2.1.2 Ti:Sa regenerative amplifier

Femtosecond laser pulses generated by a Ti:Sa laser oscillator, typically with a few nJ of energy per pulse, are suitable for weak-field studies such as multiphoton spectroscopy (see chapter 4) or two-photon laser scanning fluorescence microscopy [7]. However, strong-field experiments such as laser-induced ionization and fragmentation

require substantially higher pulse energies and therefore laser pulse amplification is required [28].

The regenerative amplifier is a device used for laser pulse amplification in which multiple passes of the pulse through the gain medium, a Ti:Sa crystal in this case, are achieved by placing the gain medium in an optical resonator together with an optical switch that lets the laser pulse out once the desired number of round trips in the resonator (possibly hundreds) is completed. The peak intensity of the laser pulse being amplified can become so high that detrimental nonlinear effects may distort the laser pulse or destruction of the gain medium or other optical element can take place. These problems can be prevented by the use of the chirped-pulse amplification (CPA) technique [29]. In CPA the pulses are temporally stretched to a much longer duration (typically from under 100 fs to ~100 ps) using a strongly dispersive device, such as a grating pair, before passing through the amplifier. As a consequence of the substantial temporal broadening produced by the stretcher, the peak intensity of the pulses is severely reduced (~3 orders of magnitude) and the detrimental effects mentioned earlier are avoided. The stretched pulses enter the amplifier where several passes through the amplification medium (typically 4-50 passes with a gain of 2-100 per pass) provide 6-9 orders of magnitude increase in the energy [30]. After the amplifier, a compressor, typically a grating pair, is used to recompress the pulses to a duration similar to that of the initial input pulses (seed pulses) and therefore a very high peak intensity is produced (Figure 2.2a).

For the experiments described in chapter 5 we used a regenerative amplifier (Legend USP, Coherent) seeded by a Ti:Sa oscillator (Micra, Coherent). This amplified

femtosecond laser system, depicted in Figure 2.2, generates 45 fs pulses at 1 kHz with energies up to ~1 mJ/pulse.

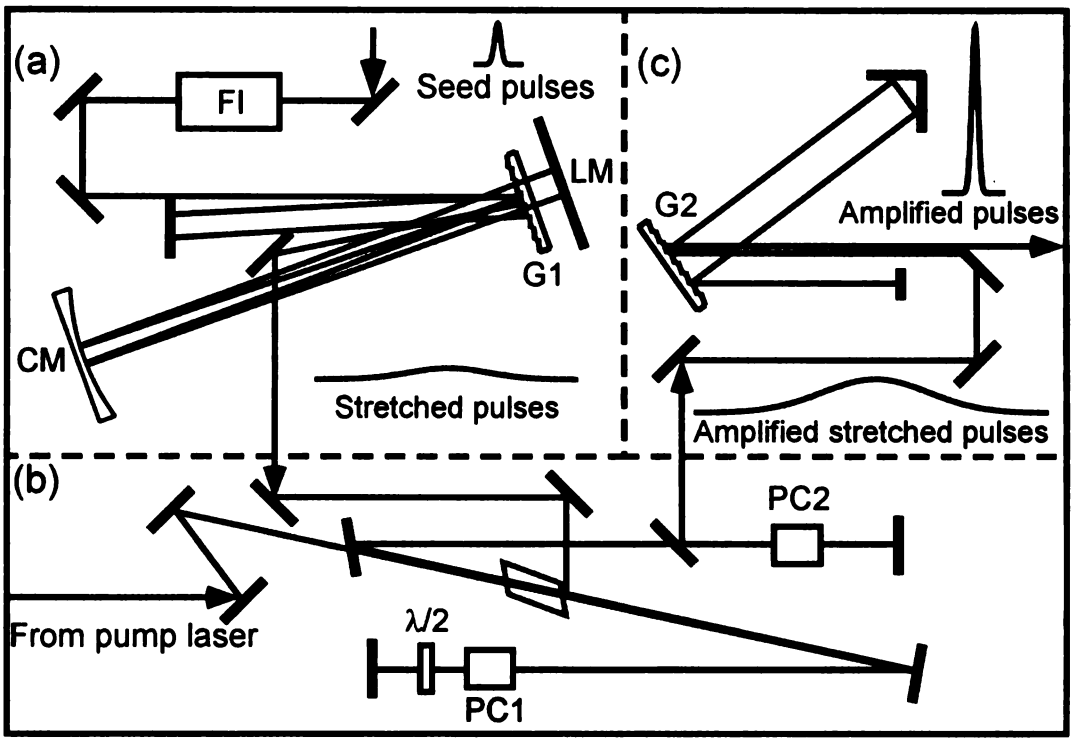

Figure 2.2. Ti:Sa regenerative amplifier setup. The amplifier is composed by the following three elements: (a) Grating-based stretcher, in which the seed pulses are stretched to a much longer duration, (b) regenerative amplifier, where the stretched pulses are amplified, and (c) grating-based compressor, where the amplified pulses are recompressed and a high peak intensity is produced. The curves illustrate the laser pulse shapes at different stages of the amplification process. FI: Faraday isolator, G1 and G2: grating, CM: curved mirror, LM: long mirror, PC1 and PC2: Pockels cells, and λ/2: half-wave plate.

2.2 Pulse shapers

Pulse shapers are devices able to manipulate laser pulses according to the user specification and thus have become an important tool to control laser-driven processes. While some simple pulse shaping tasks such imposing a quadratic spectral phase (chirp) on a pulse can be carried out with passive optics such as prism- or grating-based compressors, more complex pulse shaping tasks -such as imposing higher order (>2) polynomial or sinusoidal spectral phases- require the use of programmable pulse shapers.

Applications of programmable pulse shapers include femtosecond laser pulse characterization and compression (chapter 2), control of nonlinear optical processes [19, 31], nonlinear microscopy [7, 32], and coherent control of physicochemical processes [33, 34]. Programmable pulse shapers can be divided in two categories according to the domain, time or frequency, in which the laser pulses are manipulated. Acousto-optic programmable dispersive filters (AOPDF) shape pulses in the time domain using a time-dependent acoustic signal in a crystal (typically TeO_2) in which the pulses propagate to control both the amplitude and phase of the optical pulses [35]. Fourier-transform pulse shapers manipulate pulses in the frequency domain by spatial masking of the spatially dispersed frequency spectrum of the pulses [36]. In simple terms these devices advance or retard individual frequency components within the pulse. A more detailed description of the Fourier-transform pulse shaper, the one used throughout this dissertation, is given in the following paragraphs.

Figure 2.3 shows the Fourier-transform pulse shaper apparatus, which consists of a pair of diffraction gratings and a pair of lenses arranged in a configuration known as "4*f* configuration" or "zero dispersion pulse compressor", and a spatial light modulator (SLM) placed at the focal plane. The frequency components of the input beam are angularly dispersed by the first diffraction grating (a prism can also be used) and then focused by the first lens (a focusing mirror can also be used). Note that the frequency components of the pulse are spatially separated along one dimension at the focal plane of the lens, known as the Fourier plane of the pulse shaper. The second lens and grating recombine the frequency components and a single collimated output beam is obtained. In the absence of the SLM the output should be identical to the input pulse (therefore the

name "zero dispersion pulse compressor"). In a Fourier-transform pulse shaper a SLM is placed at the Fourier plane to manipulate the spatially dispersed frequency components of the beam. Three kinds of SLM have been the most widely used in Fourier-transform pulse shapers. A purely reflective phase shaper can be implemented with a deformable

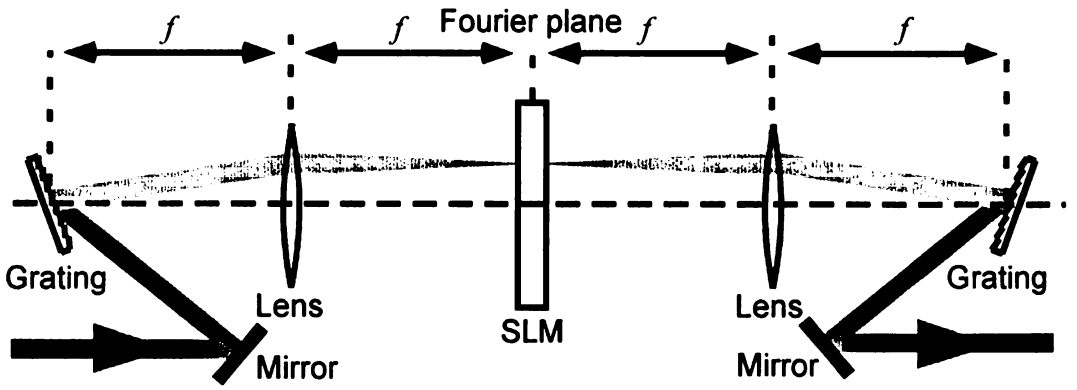

Figure 2.3. Scheme of a Fourier-transform pulse shaper. The frequency components of the input beam are angularly dispersed by a grating and focused by a lens. An SLM is placed at the focal plane (Fourier plane), where frequency components are spatially separated along one dimension, to manipulate them and obtain user-designed shaped output pulses. The second half of the shaper recombines the frequency components of the light and a collimated output beam is obtained. The setup is known as 4*f* because the optical components are separated a distance equal to the focal length of the lens (*f*).

mirror, a device consisting of a number of independently controlled mirrors, placed at the Fourier plane [37, 38]. This kind of SLM has a small loss, but the number of optical elements is typically small and the device is not able to provide amplitude control. An acousto-optic crystal can also be used as an SLM in a 4*f* setup [39, 40]. In this device an acoustic wave produces changes in the refractive index of the crystal that manipulate the spectral phase of the pulses. This kind of SLM is not limited by the number of pixels, but its efficiency can be lower than 40%. The most popular kind of SLM is the liquid crystal (LC) SLM, the device used throughout this dissertation. A LC SLM is basically a thin

layer of nematic liquid crystal sandwiched between two pieces of glass, with the inside surface of each piece coated with a thin and transparent electrically conducting material patterned into a number of separate electrodes, called pixels. When an electric field is applied to a pixel, the liquid crystal molecules tilt causing a change of the refractive index. The liquid crystal is birefringent, therefore the applied voltage can introduce pure phase retardation or a combination of phase retardation plus polarization rotation depending on the polarization of the incoming light with respect to the liquid crystal axis. Both situations are useful for pulse shaping purposes. In a phase-only LC SLM a single LC layer is used and the polarization of the input light is such that pure phase retardation is introduced [41, 42]. In a phase-amplitude LC SLM two layers of LC with perpendicular optical axes at 45° respect to the polarization of the input light are combined with an output polarizer to manipulate both the amplitude and phase of the input beam [43]. Amplitude control is then provided by the attenuation that light suffers after travelling through the output polarizer, which depends on the degree of polarization rotation that took place. If no output polarizer is used the polarization of the output pulse can be shaped and pulses with a frequency-dependent polarization can be synthesized [44]. Such pulses have been applied for coherent control applications [45, 46].

The transmission dependence on polarization described before is also useful for calibration purposes of both phase-only and phase-amplitude pulse shapers. Detailed calibration procedures have been described elsewhere [33, 36]. Very briefly, a voltage scan on the SLM results on a transmission curve for each pixel, which can be used for calibration purposes. Due to the broad frequency bandwidth of the laser systems used in

this dissertation and the frequency dependence of the refractive index, an automated pixel by pixel calibration was required for the pulse shapers.

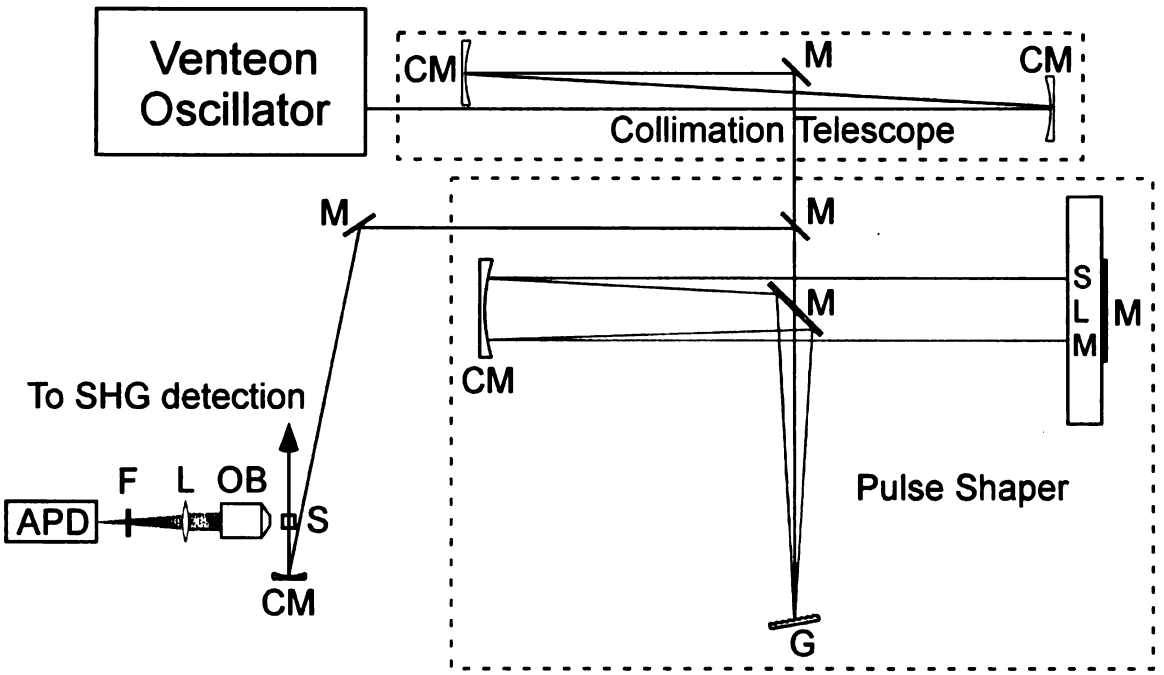

Figure 2.4. Scheme of pulse shaper I. The beam was first directed to a 1:2.5 telescope consisting of two spherical mirrors (CM) and a pinhole (P) placed at the focal point of the first spherical mirror. The all-reflective folded pulse shaper consisted of a spherical mirror (CM), mirrors (M), grating (G) and SLM.

In this dissertation a folded all-reflective pulse shaper design was used, as shown in Figure 2.4. In this case a retro-reflection mirror is placed behind the SLM. This design has two advantages with respect to the linear 4*f* setup depicted in Figure 2.3. First, it occupies half of the space. Second, it doubles the phase retardance that the shaper can introduce because light goes through the SLM twice. The output beam needs to be displaced vertically so that input and output beams can be separated. Two different pulse shapers based on this design were used:

Pulse shaper I, shown in Figure 2.4, was used with the ultrabroad-bandwidth source described in section 2.1.1. Before entering the pulse shaper, a 1:2.5 telescope was used to

collimate and expand the beam to 4 mm diameter for optimal pulse shaping resolution. In addition, a 150 μm diameter pinhole was placed at the focal point of the first spherical mirror to clean up the beam. The main components of the pulse shaper were an enhanced-aluminum coated 150-lines-per-mm grating (Newport), a 762-mm–focal-length gold-coated spherical mirror, and a 640-pixel dual-mask SLM (CRI, SLM-640).

Pulse shaper II (not shown), was used with the amplified described in section 2.1.2 between the Micra oscillator and the Legend USP amplifier. The main components of the pulse shaper were an enhanced-aluminum coated 300-lines-per-mm grating (Newport), a 508-mm–focal-length spherical mirror, and a 128-pixel SLM (CRI, SLM-128).

Commercial SLM's such as those described here provide a retardance of ~4π. When a larger retardance is required the phase is wrapped or folded into separate 2π segments.

The pulse shapers described before were used throughout this dissertation to characterize and compress pulses (chapters 3 and 6), to perform chromatic dispersion measurements of materials (chapter 4) and to generate shaped pulses to measure two-photon fluorescence excitation spectra of fluorophores (chapter 5).

2.3 Multiphoton intrapulse interference phase scan (MIIPS)

The ability to measure and correct femtosecond laser phase distortions is critical to obtain optimal and reproducible experimental results in the sub-50-fs regime. MIIPS is a single-beam method based on phase shaping that provides both capabilities with unprecedented simplicity and accuracy. The following description of MIIPS has been adapted from Y. Coello, V. V. Lozovoy, T. C. Gunaratne, B. Xu, I. Borukhovich, C. H. Tseng, T. Weinacht and M. Dantus. "Interference without an interferometer: a different

approach to measuring, compressing, and shaping ultrashort laser pulses". J. Opt. Soc. Am. B 25, A140 (2008) [27].

Pulse compression, shaping, and characterization at the laser target are of critical importance to ensure reproducible femtosecond laser applications, which now include: biomedical imaging, metrology, micromachining, analytical chemistry, material processing, photodynamic therapy, surgery, and even dentistry. In principle, the Fourier transform of the ultrashort electromagnetic pulse spectrum provides its temporal duration. This statement is accurate when the pulse is transform-limited (TL); i.e., all frequency components in its bandwidth have the same phase. The actual pulse duration of ultrashort pulses is always greater than that of the TL pulse because of phase distortions that arise from optics and from transmission through any medium other than vacuum. Here we use the ratio τ/τ_{TL} as a parameter to characterize the quality of the pulse, where τ and τ_{TL} are the time durations of the measured and TL pulses, respectively. Strictly speaking, root-mean-square time durations should be used for τ; however, the generalized approach is to use the FWHM time duration for simplicity. The τ/τ_{TL} parameter is similar to the M^2 parameter used in optical design, giving the ratio between the measured value versus the theoretical optimum. Typical values for τ/τ_{TL} range from 1.1 for well-tuned systems to less than 1.5 for most advertised commercial systems, and finally from 10 to 100 when pulses are broadened by optics such as high-numerical-aperture microscope objectives.

Ultrashort pulse broadening is a serious problem affecting every application. One can divide approaches to dealing with it into two broad categories: direct compression and phase measurement followed by compensation. For the former approach, phase distortions are minimized without being measured; the latter depends on accurate phase

measurement followed by accurate compensation. The most common approaches to pulse compression are illustrated schematically in Figure 2.5a through 2.5c. The early incorporation of compressors consisting of gratings, prisms, and their combination led to the great advancements in femtosecond technology during the early eighties, culminating in the production of 6 fs pulses [22]. This approach, which requires one or more laser experts, is illustrated in Figure 2.5a. A second characterization-free approach uses a computer-controlled pulse shaper and an optimization algorithm that takes the integrated second harmonic generation (SHG) intensity from the laser pulses as the feedback in a closed loop [47, 48], as it is illustrated in Figure 2.5b. In both of these characterization-free cases, success depends on the noise level of the laser system. The pulse-to-pulse stability of the SHG output is typically 2-6%, assuming laser fluctuations of 1-3% in the fundamental. Because $\tau/\tau_{TL}=I_{SHG\text{-}TL}/I_{SHG}$, measurement-free approaches could reach τ/τ_{TL} values as low as 1.02-1.06 provided the algorithm is given sufficient time to converge. For many cases this level of performance is sufficient, and using a prism/grating compressor or even a simple uncalibrated pulse shaper with feedback will accomplish the task.

If $\tau/\tau_{TL}<1.1$ is consistently required, such as when the ultrashort pulses are used to study optical properties of materials, an actual measurement of the pulses is required. The simplest situation arises when well-characterized pulses, such as TL pulses, are used for measuring phase-distorted pulses. In this situation, the unknown phase distortions can be calculated from the interferogram between the unknown and the reference pulses. Unfortunately, well-characterized pulses are not usually available. It has also been shown theoretically and experimentally that, through an iterative algorithm, one can determine

the pulse field from a fringe resolved autocorrelation and the spectrum of the pulse [49]. However, this algorithm is rarely used. A more common approach is to retrieve the unknown phase using an autocorrelator/interferometer-based technique such as frequency resolved optical gating (FROG) [50, 51] or spectral phase interferometry for direct electric-field reconstruction (SPIDER) [52, 53], and to use the knowledge of the retrieved phase and a calibrated pulse shaper for pulse compression [35, 54-56]. This approach is illustrated in Figure 2.5c.

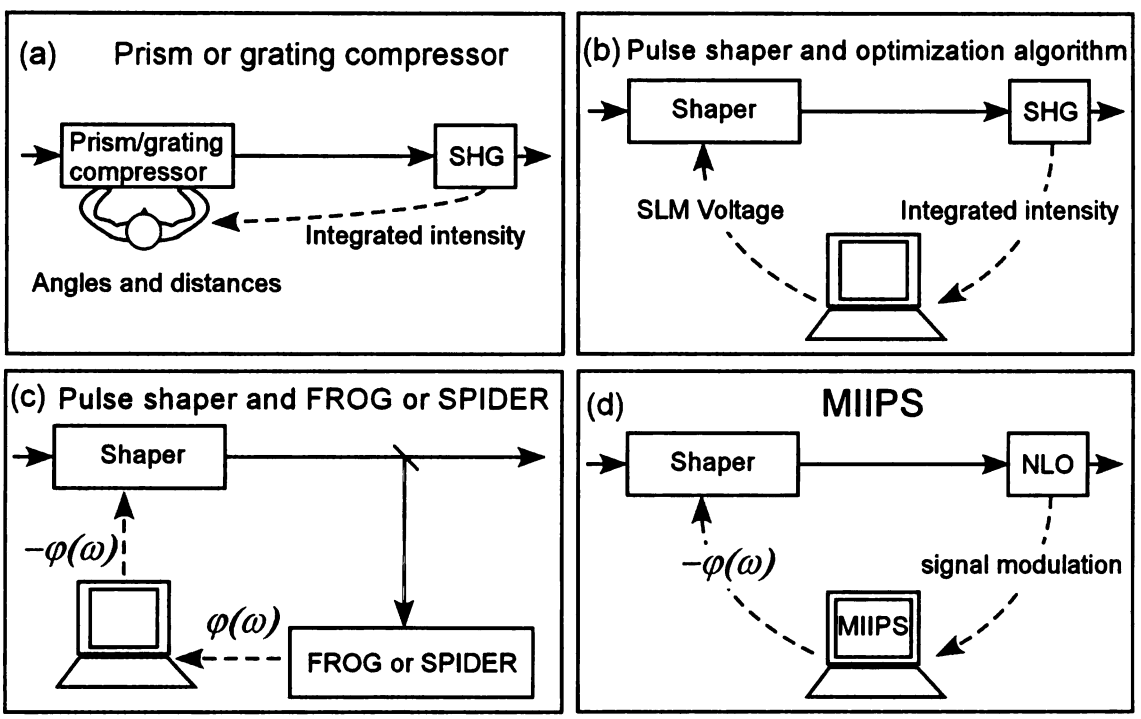

Figure 2.5. Pulse compression approaches. (a) Manual prism/grating compressor adjustment. (b) Optimization algorithm using the SHG signal as feedback. These two approaches do not require spectral phase measurements. (c) Measurement and correction using FROG or SPIDER as the characterization technique. (d) MIIPS. Measurement and correction are seamlessly integrated in a compact setup. NLO, nonlinear optical medium.

Here we discuss a different approach, called multiphoton intrapulse interference phase scan (MIIPS) [18, 57-59], to accurately measure and correct the unknown phase

distortions of the pulses, while avoiding the use of autocorrelation or interferometry, as is illustrated in Figure 2.5d.

We start our discussion by remembering the effect of the different terms of a Taylor expansion of the spectral phase $\varphi(\omega)$ on the time profile of an ultrashort pulse.

$$\varphi(\omega) = \varphi_0 + \varphi_1(\omega - \omega_0) + \tfrac{1}{2}\varphi_2(\omega - \omega_0)^2 + \tfrac{1}{6}\varphi_3(\omega - \omega_0)^3 \cdots \quad (2.1)$$

The zeroth order phase φ_0 (sometimes called absolute phase) determines the relative position of the carrier wave with respect to the pulse envelope. In most cases, the φ_0 term is of little interest. This is due to the fact that when the pulse is many carrier-wave cycles long, which is the most common situation, a change in φ_0 has a very small effect on the pulse field. None of the pulse characterization methods mentioned in this paper is able to measure the zeroth order phase. The first order phase φ_1 corresponds to a shift of the pulse envelope in time. Given that the interest is typically centered on the pulse shape, and not on the arrival time of the pulse, the φ_1 term is also of little interest. The second and higher order terms do have an effect on the time profile of the pulses. From the above discussion, it becomes clear that it is the second derivative of the spectral phase $\varphi''(\omega) = \varphi_2 + \varphi_3(\omega - \omega_0)\cdots$, the parameter that determines the pulse shape.

MIIPS measures $\varphi''(\omega)$ by successively imposing a set of parameterized (p) reference spectral phases $-f(\omega,p)$ to the pulses with unknown phase distortion $\varphi(\omega)$ and acquiring the corresponding nonlinear optical (NLO) spectra, for example SHG. The total second-derivative of the spectral phase is then $\varphi''(\omega)$-$f''(\omega,p)$ and maximum SHG

intensities will take place at frequencies that satisfy $\varphi''(\omega)$-$f''(\omega,p)$=0, as demonstrated using multiphoton intrapulse interference (MII) principles in Section 1.2. In second derivative space, the set of reference functions $f''(\omega,p)$ can be visualized as a grid used to map the unknown $\varphi''(\omega)$, *i.e.* to find which $f''(\omega,p)$ intersects $\varphi''(\omega)$ at any desired frequency ω_i. The required reference function is simply the one that maximizes the NLO local signal, *i.e.*

$$\varphi''(\omega_i)=f''(\omega_i,p_{max}(\omega_i)), \qquad (2.2)$$

where $p_{max}(\omega_i)$ is the parameter in the reference phase function for which the NLO signal is maximized at ω_i.

The simplest grid for mapping the unknown second derivative of the phase consists of constant functions $f''(\omega,p)=p$ (Figure 2.6a) [60], which correspond to different amounts of linear chirp. In this case, different amounts of linear chirp can be imposed on the pulses using passive or adaptive optics. For each reference phase, a NLO spectrum is plotted as a function of p in a two dimensional contour map (Figure 2.6c). The feature of interest is $p_{max}(\omega)$, which can be visualized drawing a line through the maxima in the contour plot (solid curve in Figure 2.6c). The spectral phase information is directly obtained by finding $p_{max}(\omega)$ and using Equation 2.2. In the case of chirp MIIPS, Equation 2.2 reads $\varphi''(\omega)=f''(\omega,p_{max}(\omega))=p_{max}(\omega)$. Therefore, the unknown $\varphi''(\omega)$ is directly obtained from the contour plot without any mathematical retrieval procedure, as shown in Figure 2.6c [60].

If an adaptive pulse shaper is used, the number of possible reference functions that can be used is unlimited. Sinusoidal reference spectral phases $f(\omega,\delta)=\alpha\sin[\gamma(\omega-\omega_0)-\delta]$, where δ is a parameter scanned across a 4π range, have been extensively used [18, 58, 59]. When the NLO signal is plotted as a function of ω and $f''(\omega,p)$, the results obtained from applying any type of reference phase function reveal the unknown $\varphi''(\omega)$ by finding the line that goes through the maxima in the contour plot. Figures 2.6d through 2.6f illustrate the case of sinusoidal reference functions. The dashed lines in Figure 2.6d correspond to the second derivative of the reference functions, $f''(\omega,\delta)= -\alpha\gamma^2\sin[\gamma(\omega-\omega_0)-\delta]$. The sinusoidal MIIPS approach has been described in great detail elsewhere [19, 59]. Experimental measurements using both chirp and sinusoidal MIIPS are presented in this dissertation.

A MIIPS scan takes between 5 and 15 s depending on the device used to introduce the reference phases and the number of phases used. Although not necessary in all cases, an iterative measurement-compensation routine can be used to achieve the maximum possible accuracy, especially in the case of complex spectral phases [19, 59, 60]. Double integration of the measured $\varphi''(\omega)$ results in $\varphi(\omega)$. Once $\varphi(\omega)$ is obtained, the introduction of $-\varphi(\omega)$ by the shaper eliminates the measured phase distortions to achieve TL pulses. A comprehensive analysis of the precision and accuracy of MIIPS was carried out in 2006 [59]. Using MIIPS, τ/τ_{TL} values routinely reach the 1.01 level and in some cases are even lower than 1.001.

MIIPS has been used in this dissertation to characterize and compress pulses (chapters 3, 5 and 6) and to perform chromatic dispersion measurements of materials (chapter 4). Other reported applications of MIIPS include standoff chemical detection

[61], coherent control of molecular fragmentation [28], two-photon laser scanning fluorescence microscopy [7, 32], and micromachining [62].

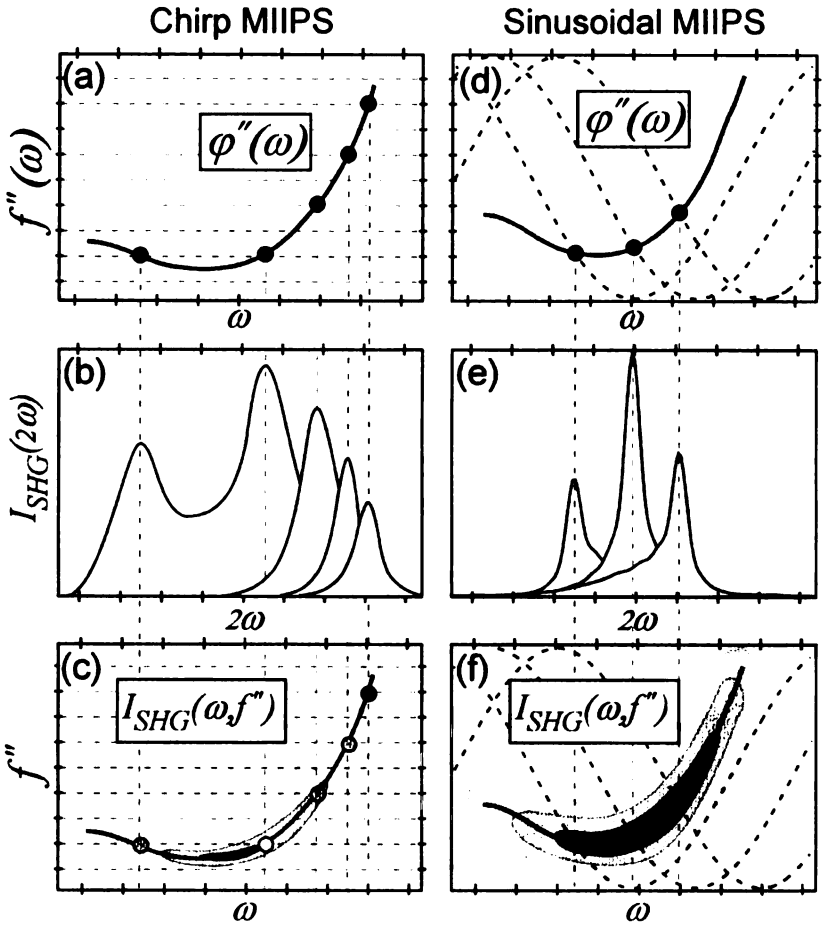

Figure 2.6. Principle of MIIPS. A set of reference functions $f''(\omega,p)$ provides a reference grid that is used to map the unknown phase $\varphi''(\omega)$. (a)-(c) and (d)-(f) illustrate the case of a horizontal and sinusoidal reference grid, respectively. (a) The unknown $\varphi''(\omega)$ (solid line) is probed using a horizontal reference grid (dashed horizontal lines). (b) shows the SHG spectra corresponding to four reference phases. The maximum SHG intensity for every frequency indicates that the corresponding reference chirp value intersected the unknown function at such frequency. (c) shows the corresponding MIIPS trace, a 2D contour plot showing the SHG intensity as a function of ω and p. The line drawn through the maxima in the countour plot directly reveals the unknown $\varphi''(\omega)$. (d) The unknown $\varphi''(\omega)$ (solid line) is probed using a sinusoidal reference grid (dashed curves). (b) shows the SHG spectra corresponding to three reference phases. The maximum SHG intensity for every frequency indicates that the corresponding reference sine function intersected the unknown function at such frequency. (c) shows a 2D contour plot showing the SHG intensity as a function of ω and $f''(\omega,p)$. When the SHG intensity is plotted this way, the line drawn through the maxima in the contour plot directly reveals the unknown $\varphi''(\omega)$.

Chapter 3

Femtosecond laser pulse characterization and compression using MIIPS

The advantages of using femtosecond laser pulses in the sub-50 fs regime cannot be realized if an accurate pulse compression method is not employed. For instance, if 50 and 10 fs TL pulses propagated through 1 cm of quartz, their durations would increase to 54 and 100 fs, respectively. The initially shortest pulse (10 fs) would suffer more extensive pulse broadening (a 10-fold increase in its temporal duration) and would end up being the longest. This example illustrates the fact that pulse broadening becomes more severe as the time duration decreases. This phenomenon occurs because shorter pulses have broader spectral bandwidths and therefore experiment bigger spectral phase distortions due to material dispersion. The lack of an accurate method able to compress the pulses at the sample position by correcting the phase distortions introduced by optical media present in the experimental setup explains the fact that most multiphoton imaging experiments, in which signal is inversely related to the temporal duration of the pulses, still employ ~100 fs pulses [6] even though laser systems generating substantially shorter pulses (<10fs) durations have been commercially available for several years.

This chapter presents results on femtosecond laser pulse characterization and compression using MIIPS, a method that satisfies the above requirements and allows achieving optimal and reproducible results in applications using sub-50 fs pulses. An illustrative example of the potential of MIIPS to enhance nonlinear imaging applications was reported in 2008, when numerous advantages resulting from MIIPS pulse compression were demonstrated for two-photon laser scanning fluorescence microscopy (TPLSM) using 10 fs pulses, including higher fluorescence intensity, deeper sample

penetration, improved signal-to-noise ratio, and less photobleaching. These advantages were not observed if only quadratic phase distortions were compensated for while higher order phase distortions were not [7].

The chapter is organized as follows. Section 3.1 describes selected spectral phase measurements, while section 3.2 demonstrates pulse compression for the two laser systems employed in this dissertation. All SHG spectra simulations were calculated using Equation 1.7.

3.1 Spectral phase measurements

The spectral phase measurement examples presented here were performed using the ultrabroad-bandwidth laser oscillator described in section 2.1.1. Unfortunately, there was no available commercial filter able to separate the SHG from the fundamental spectrum due to very broad bandwidth (almost one octave) of both spectra. A light separation device was built for this purpose. Figure 3.1 shows the setup used for these experiments, which includes the device for SHG generation, separation and detection. After pulse shaper I (section 2.2) the beam is focused by a 200-mm-focal-length silver-coated spherical mirror (SM) onto a 20μm KDP (potassium dihydrogen phosphate) crystal (C) to generate the SHG signal. Both the fundamental (dashed line) and SHG (solid line) beams are collimated by lens L1 and then directed to the separation device, a quartz-prism-based folded 4*f* Fourier Transform pulse shaper. A razor blade (R) was placed at the Fourier plane to block fundamental frequency components while allowing the reflection of the SHG light by the retro-reflection mirror (RM). The output of the separation device was focused by lens L3 into the spectrometer (QE65000, Ocean Optics Inc.). No optical fiber was used to optimize the transmission of SHG light. All lenses were made of quartz and

all mirrors after the crystal were coated with protected aluminum to avoid losing SHG light.

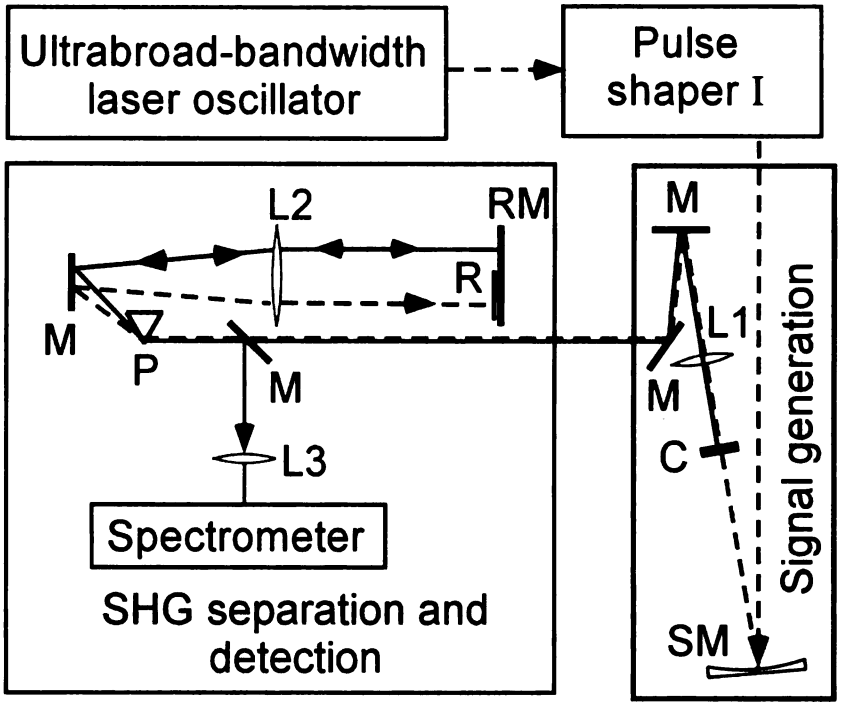

Figure 3.1. MIIPS optical setup for the ultrabroad-bandwidth femtosecond laser system. The beam (dashed line) from pulse shaper I is focused by a spherical mirror (SM) onto a KDP crystal (C) to generate the SHG beam (solid line). Both beams are collimated by lens L1 and directed a quartz-prism-based folded 4*f* Fourier Transform pulse shaper (P: prism, L2: lens, RM: retro-reflection mirror) with a razor blade (R) placed at the Fourier plane to block all fundamental frequency components while allowing the reflection of the SHG light by RM. The output beam from the separation device is focused into the spectrometer by lens L3. M: mirror.

Some of the results presented in this section were originally published in V. V. Lozovoy, B. Xu, Y. Coello and M. Dantus. "Direct measurement of spectral phase for ultrashort laser pulses". Opt. Express 16, 592 (2008).

Quadratic and cubic spectral phases are the most commonly encountered phase distortions because they are introduced by material dispersion (section 1.1). Both correspond to a linear function in second-derivative space. To demonstrate the ability of MIIPS to measure this kind of spectral phase, the cubic function $\varphi(\omega)=500fs^3(\omega-\omega_0)^3$ was

added to TL pulses (how to obtain TL pulses is described in next section) using the pulse shaper and then measured using chirp MIIPS. Figure 3.2 shows experimental (Figure 3.2a) and simulated (Figure 3.2b) chirp MIIPS traces of the pulses. For the simulated spectra, the cubic spectral phase was added to perfectly TL pulses ($\varphi(\omega)$=0).

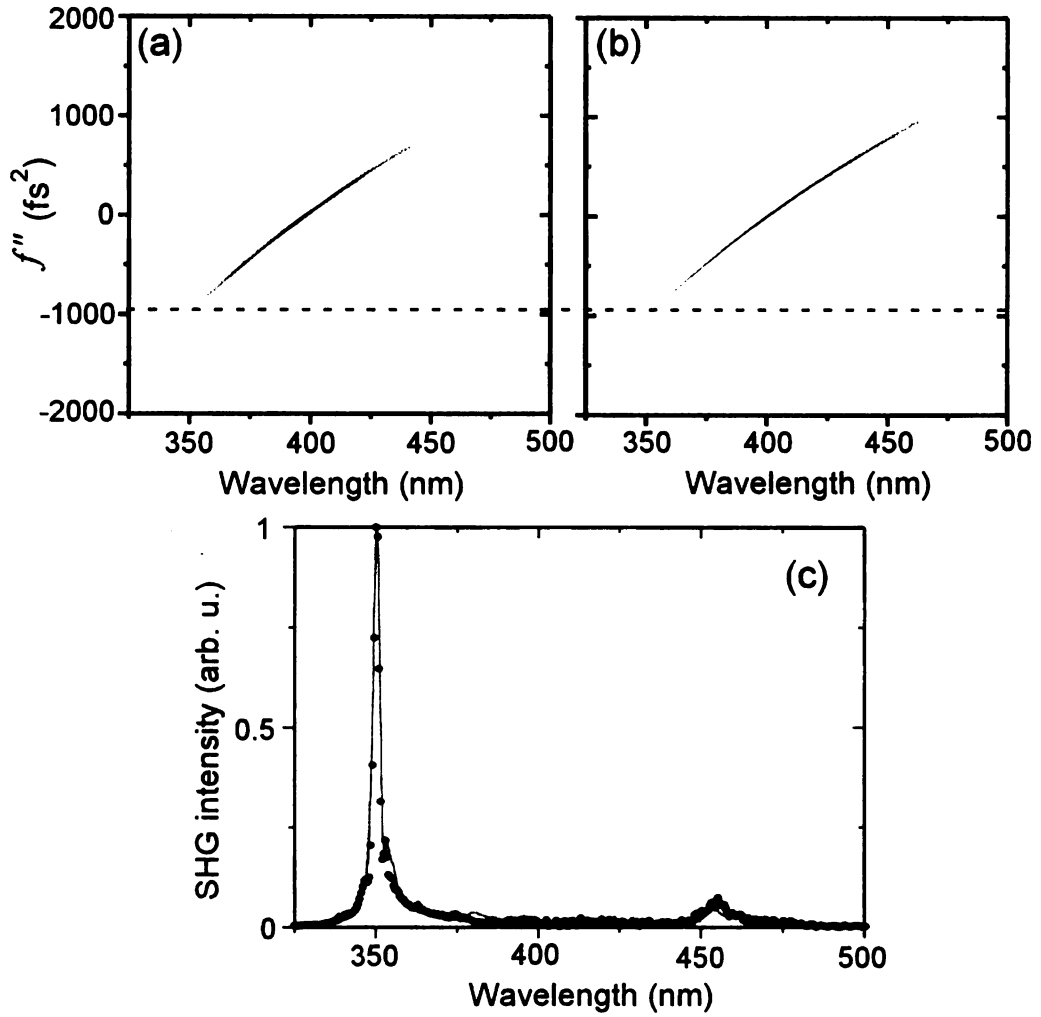

Figure 3.2. Experimental and simulated chirp MIIPS traces demonstrating accurate pulse shaping. The cubic spectral phase defined by $\varphi(\omega)=500fs^3(\omega-\omega_0)^3$ was introduced to TL pulses. (a) Experimental chirp MIIPS trace. (b) Simulated chirp MIIPS trace. The dashed line indicates the chirp reference value used for (c). (c) Experimental (dotted curve) and simulated (gray solid line) SHG spectra corresponding to the dashed line in (a) and (b). The excellent agreement between experiment and simulation demonstrates accurate pulse shaping capability.

For both the experiment and simulation, the chirp reference functions were varied in steps of $5fs^2$. Figure 3.2c shows the experimental and simulated SHG spectra corresponding to the dashed line in Figs. 3.2a and b. The excellent agreement between experimental and simulated results demonstrates accurate pulse shaping. If the cubic and chirp phases were not introduced accurately, this agreement would not be possible.

Figure 3.3a shows the normalized chirp MIIPS trace, in which the maximum SHG intensity for each frequency was set to the same value, to visualize the measured φ'' more clearly. As explained in section 2.3, φ'' is directly obtained from the curve drawn through the maxima in the trace, without any mathematical treatment. Figure 3.3b shows the resulting measured φ'' (dotted line) together with the calculated second-derivative of the introduced phase (solid gray line). Note the agreement between both. The only points that deviate from the expected values correspond to the edges of the fundamental spectrum, where insufficient SHG light is generated. These deviations have little or no effect in the calculated spectral phase, which is obtained after double integration. Figure 3.3c shows the resulting spectral phase $\varphi(\omega)$ (dotted line) together with the introduced one (solid gray line). Note the excellent agreement between both across the whole bandwidth. An independent cross-check can be performed by comparing the experimental and simulated SHG spectrum corresponding to the introduced phase. Figure 3.3d shows that comparison, which confirms the accuracy of the measurement.

The availability of automated pulse shapers has made possible the generation of complex spectral phases, which are used in areas such as coherent control [19, 34] and nonlinear microscopy [7, 18, 32]. To demonstrate the ability of MIIPS to measure

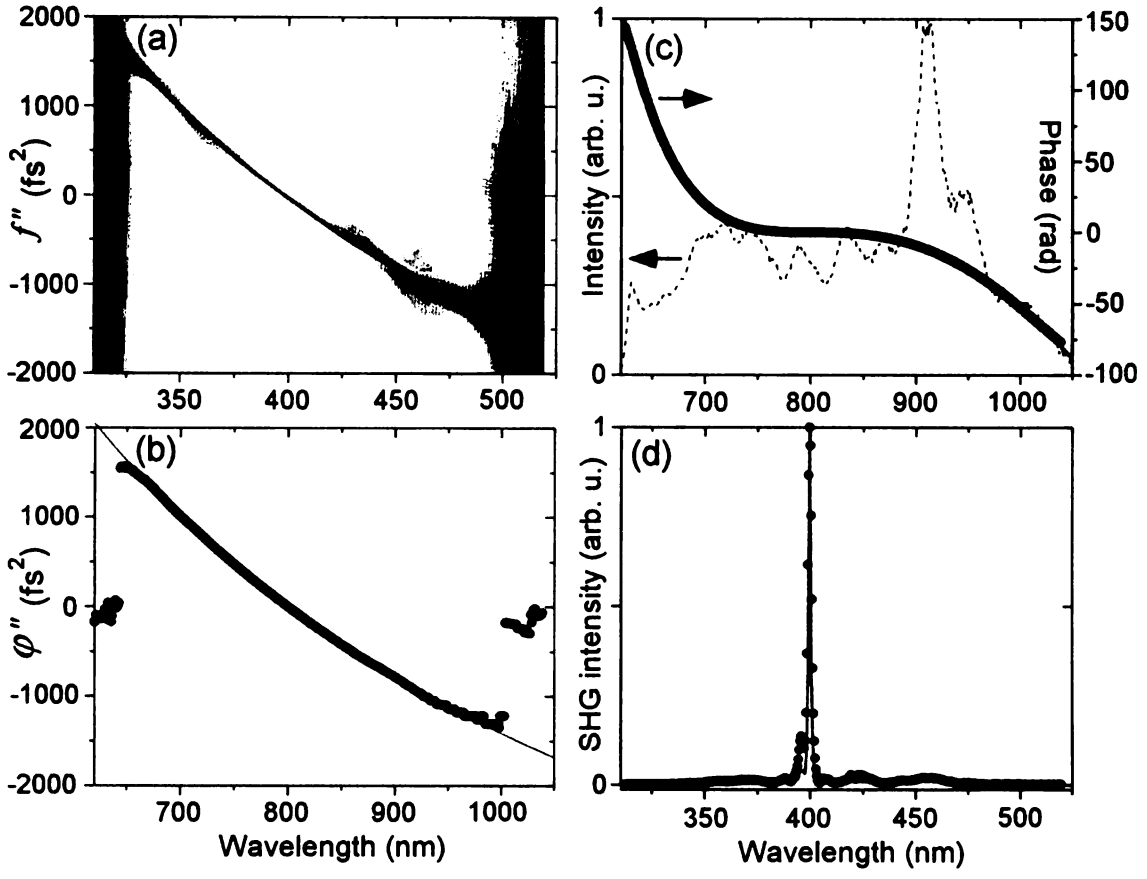

Figure 3.3. MIIPS measurement of a cubic spectral phase. The introduced phase function was $\varphi(\omega)=500fs^3(\omega-\omega_0)^3$. (a) Normalized chirp MIIPS trace. (b) Measured second-derivative of the phase (dotted line), which directly corresponds to the line drawn through the maxima in (a). The calculated second-derivative of the introduced phase (solid gray line) is shown for comparison. (c) Measured (dotted line) and introduced (solid gray line) cubic spectral phase. The agreement across the whole bandwidth is excellent. (d) Measured (dotted line) and simulated (solid gray line) SHG spectrum corresponding to the introduced phase. The agreement confirms the accuracy of the spectral phase measurement.

complex spectral phases, the sinusoidal function $\varphi(\omega)=5\pi sin[7fs\ (\omega-\omega_0)]$ was added to TL pulses using the pulse shaper and then measured using chirp MIIPS. The chirp reference functions were varied in steps of $5fs^2$. Figure 3.4a shows the normalized chirp MIIPS trace, from which φ'' is directly obtained, as shown in Figure 3.4b. Figure 3.4c shows the measured (dotted line) and the introduced (solid gray line) spectral phases.

Finally, Figure 3.4d shows the experimental and simulated SHG spectrum corresponding to the introduced sinusoidal phase. The agreement between the introduced and measured phases illustrates the performance of MIIPS for the case of complex spectral phases.

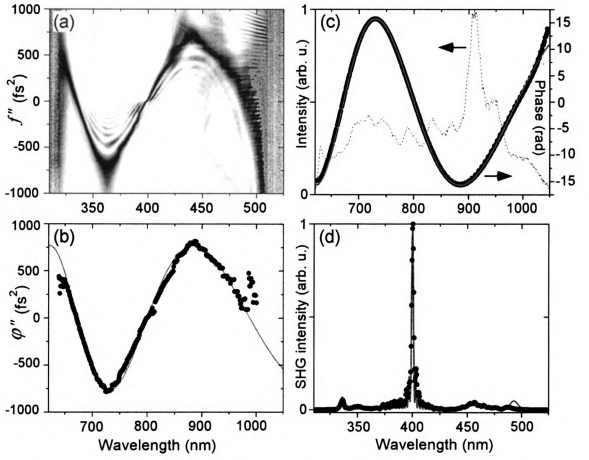

Figure 3.4. MIIPS measurement of a complex spectral phase. The introduced phase function was $\varphi(\omega)=5\pi\sin[7\text{fs}\ (\omega-\omega_0)]$. (a) Normalized chirp MIIPS trace. (b) Measured second-derivative of the phase (dotted line), directly obtained from the trace in (a). The calculated second-derivative of the introduced phase (solid gray line) is shown for comparison. (c) Measured (dotted line) and introduced (solid gray line) cubic spectral phase show an excellent agreement. (d) Measured (dotted line) and simulated (solid gray line) SHG spectrum corresponding to the introduced phase. The agreement confirms the accuracy of the spectral phase measurement.

3.2 Pulse compression

Pulse compression is a straightforward task provided the spectral phase of the pulses is known. As demonstrated in the previous section, MIIPS is able to accurately measure the spectral phase $\varphi(\omega)$ of femtosecond laser pulses. After the measurement, the introduction of $-\varphi(\omega)$ by the shaper eliminates the measured phase distortions to achieve TL pulses.

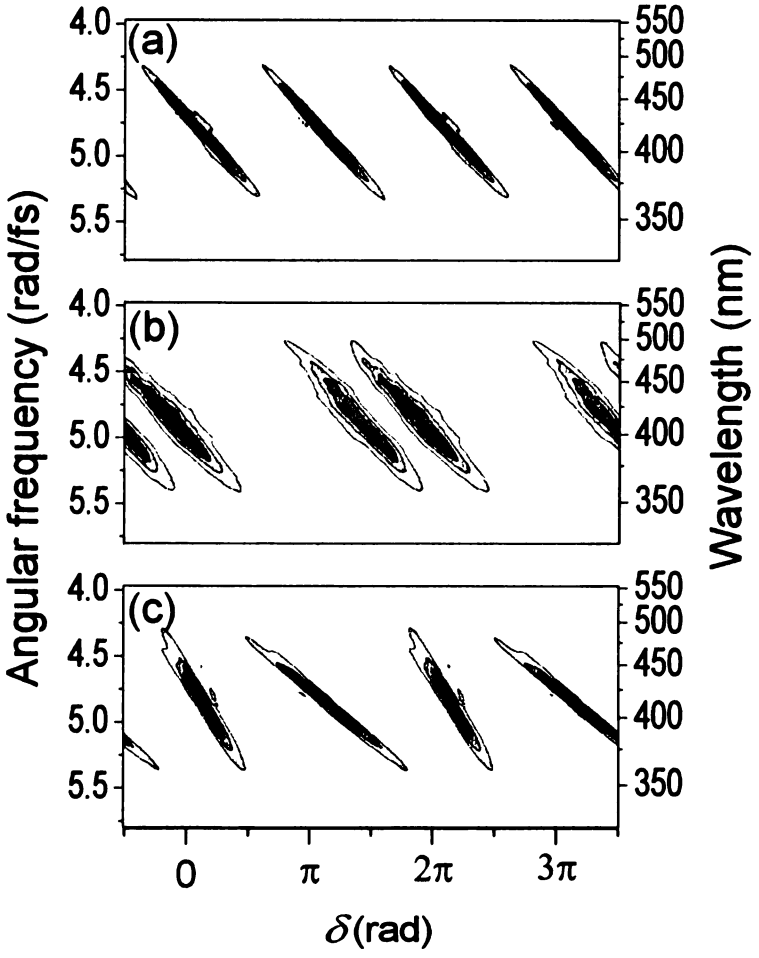

Figure 3.5. Characteristic sinusoidal MIIPS traces. The experiments were performed using the setup depicted in Figure 3.1. (a) Sinusoidal MIIPS trace for TL pulses. The four diagonal features are equally spaced and have the same slope. (b) Sinusoidal MIIPS trace showing the change in spacing between the diagonal features caused by a φ''=120 fs^2 quadratic phase distortion in the frequency domain. (c) Sinusoidal MIIPS trace showing the slope change caused by a φ''' =336 fs^3 cubic phase distortion in the frequency domain.

Pulse compression has been performed routinely on the two laser systems employed in this work using sinusoidal MIIPS. Due to historical reasons, the SHG intensity has been plotted as a function of frequency and the parameter δ rather than as a function of frequency and the reference function in sinusoidal MIIPS traces, *i.e.* $I_{SHG}(\omega,\delta)$ instead of $I_{SHG}(\omega,f(\omega,\delta))$. Consequently, the measured φ'' is not directly visualized in the sinusoidal MIIPS trace, as was described in section 2.3. Instead, diagonal parallel lines separated by π are obtained for $\delta_{max}(\omega)$ when the pulses are transform-limited (Figure 3.5a). Quadratic phase distortions cause a change in the spacing between the lines (Figure 3.5b), and cubic phase distortions cause a change in the inclination of these lines (Figure 3.5c). In these two last cases cases, the changes are proportional to the magnitude and sign of the distortion.

3.2.1. Compression of ultrabroad-bandwidth femtosecond laser pulses

This section describes pulse compression carried out with MIIPS for the laser system described in 2.1.1. The setup depicted in Figure 3.1 was employed. A representative fundamental spectrum of this system is shown in Figures 3.3 and 3.4.

The ability to measure and correct the spectral phase of a femtosecond laser becomes more challenging as the spectral bandwidth increases. Furthermore, when dealing with sub-5 fs pulses, the task represents a significant challenge. Actually, there was a single report on compression of sub-5 fs pulses before 2005 [63] and a couple more appeared in 2005-2006 together with our first report on pulse compression of this laser system [26, 64, 65]. Since that first demonstration [65], pulse compression for this system was achieved routinely in our laboratory.

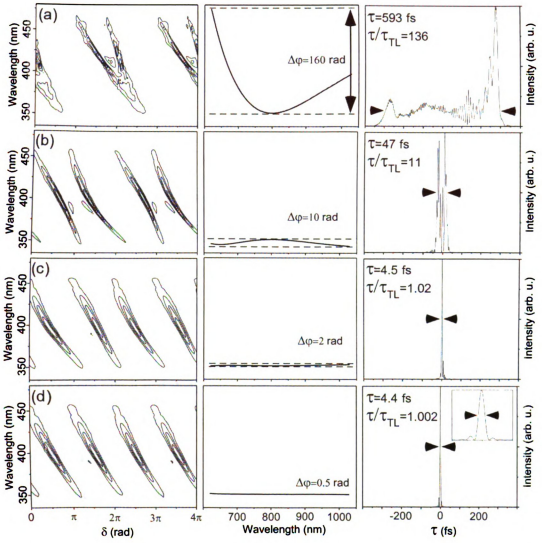

Figure 3.6. MIIPS compression process of ultrabroad-bandwidth femtosecond laser pulses from ~600fs to sub-5fs TL time duration. In this experiment, ultrabroad-bandwidth femtosecond laser pulses with severe spectral phase distortions were characterized and compressed to their TL pulse duration of 4.4 fs using MIIPS. The left, middle and right columns show the sinusoidal MIIPS traces, measured spectral phases and calculated temporal profiles for each MIIPS scan, respectively. (a), (b), (c) and (d) correspond to the first, second, third and fourth MIIPS scans. Note that the first two MIIPS measurement-correction iterations, (a) and (b), are enough to compress the pulses, as revealed by the diagonal parallel features in the MIIPS trace corresponding to the third scan (c), which indicate TL pulses. Quantitatively, the pulses were compressed from τ/τ_{TL}=136 to τ/τ_{TL}=1.02 in the first two scans. After the inverse of the phase distortion measured in the third scan was applied to the pulses, further compression to τ/τ_{TL}=1.002 was obtained, as indicated by the fourth scan (d).

Figure 3.6 illustrates an example pulse compression procedure after initially TL pulses of 4.4 fs duration were temporally broadened by propagating through 2 cm of water. The left, middle and right columns in Figure 3.6 show the MIIPS traces, measured spectral phases and calculated temporal profiles for each scan, respectively. Figure 3.6a corresponds to the first scan. Note that the trace (left panel) indicates the presence of both quadratic and cubic components in the phase distortion because of the spacing and slope of the diagonal features, respectively. The measured spectral phase (middle panel) reveals a distortion spanning 160 rad across the spectrum. The calculated temporal profile (right panel) indicates severe temporal broadening to 593 fs, corresponding to τ/τ_{TL}=136. The inverse of the measured phase is added to the pulses after each scan. Consequently, the MIIPS features are much less distorted in the second scan, corresponding to Figure 3.6b, but still show altered spacing and curvature (left panel). The corresponding spectral phase now spans 10 rad (middle panel) and the FWHM time duration of the pulses is 47 fs (right panel). The resulting diagonal parallel features in the third scan (Figure 3.6c, left panel) indicate that the pulse compression procedure is complete. Note that the MIIPS procedure could have been stopped in the second scan and 4.5 fs pulses, corresponding to τ/τ_{TL}=1.02, would have been obtained after applying the inverse of the measured phase. This level of pulse compression is enough for most applications. However, after a third scan (Figure 3.6c) further pulse compression corresponding to τ/τ_{TL}=1.002 is achieved. The fourth scan was performed only to measure the compression level after the third MIIPS scan.

Slight variations in the fundamental spectrum of the pulses due to different oscillator settings lead to consequent slight variations of the duration of the pulses in the

range 4.3-4.6 fs. The shortest pulse duration achieved with this laser system (4.3fs) matched the shortest pulse duration ever obtained directly from a laser oscillator [26].

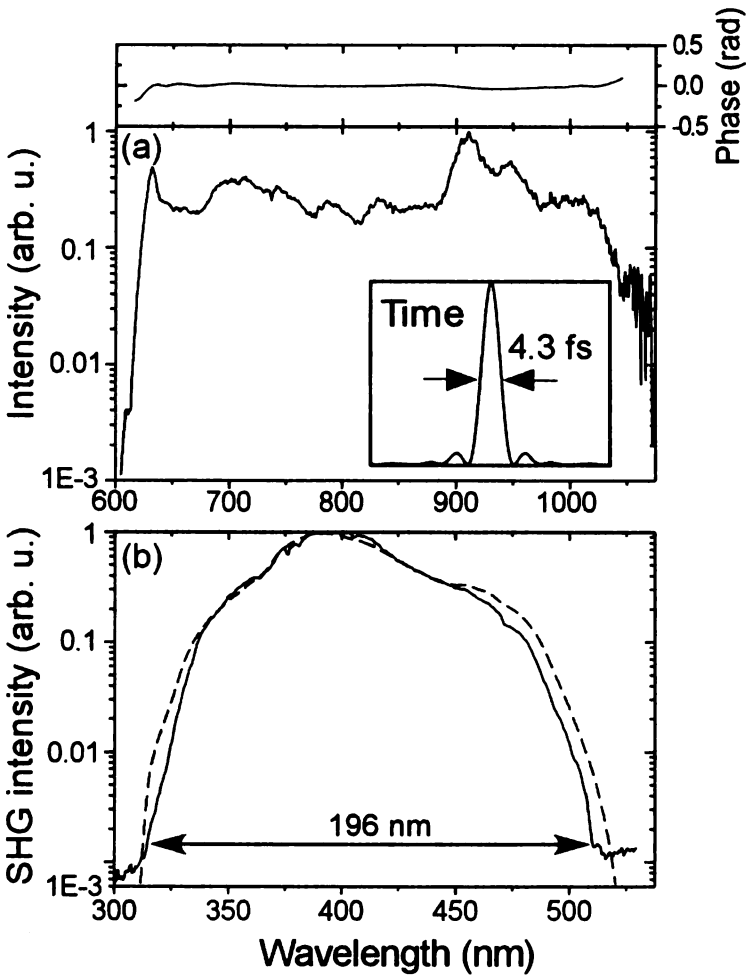

Figure 3.7. Results of MIIPS compression for ultrabroad-bandwidth femtosecond laser pulses. (a) Spectrum of the ultrabroad-bandwidth femtosecond laser pulses. The longer wavelength edge of the spectrum looks noisier than rest because of the lower spectral response of the spectrometer in that region. The spectral phase was corrected within 0.1 rad accuracy across the whole bandwidth (top panel). The resulting FWHM time duration was 4.3 fs (inset), the shortest ever obtained directly from a laser oscillator. (b) Measured SHG spectrum (solid curve) of the pulses after compression, the broadest UV spectrum ever obtained directly from an oscillator and a nonlinear crystal. The simulated SHG spectrum is also shown (dashed curve). The response function of the crystal was not considered in the calculation.

The results shown in Figure 3.7 were originally published in Y. Coello, V. V. Lozovoy, T. C. Gunaratne, B. Xu, I. Borukhovich, C. H. Tseng, T. Weinacht and M. Dantus. "Interference without an interferometer: a different approach to measuring, compressing, and shaping ultrashort laser pulses". J. Opt. Soc. Am. B 25, A140 (2008) [27]. Figure 3.7a shows the fundamental spectrum of the pulses together with the residual spectral phase after MIIPS compression (top panel). The inset shows the calculated temporal profile corresponding to 4.3fs FWHM. The compressed pulses generated the SHG spectrum shown in Figure 3.7b (solid line), the broadest UV spectrum obtained directly from an oscillator and a nonlinear crystal.

The broad UV spectrum generated by the compressed pulses (Figure 3.7b) represents additional solid evidence of successful pulse compression. Even though, an extra independent cross-check of the compression result was performed by comparing the experimental interferometric autocorrelation (IAC, also known as fringe-resolved autocorrelation) [51] of the pulses with the simulated IAC of perfectly TL pulses ($\varphi(\omega)$=0). IAC experiments require splitting the pulse in two, variably delaying one with respect to the other, and spatially overlapping both collinearly propagating pulses in a nonlinear optical medium such as an SHG crystal. This is typically achieved by placing a SHG crystal at the output of a Michelson interferometer. The IAC, obtained plotting the SHG intensity versus time delay, can be used to estimate the time duration of the pulses. Using the pulse shaper, two identical replicas of a pulse separated by variable time delays can be generated and thus an IAC experiment can be performed without the complications that an interferometric setup involves. The pulse shaping functions required for this task have been described elsewhere [27]. Here, the experimental and

simulated IAC of the pulses are shown in Figure 3.8 to further demonstrate successful pulse compression.

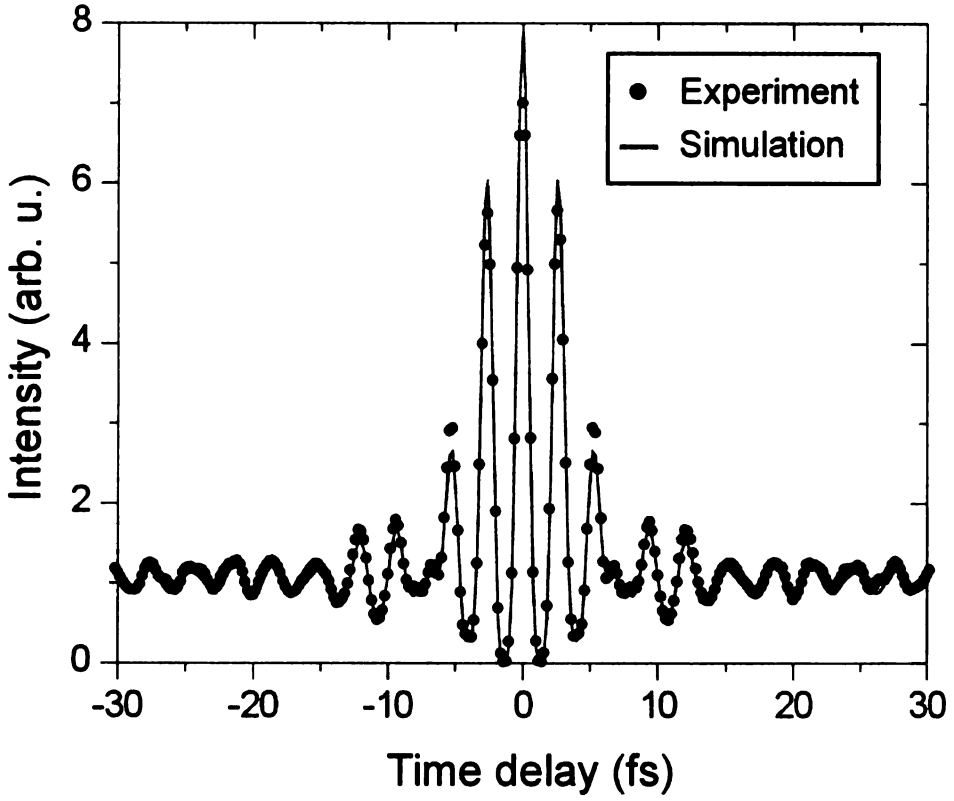

Figure 3.8. Pulse-shaper assisted and simulated IAC of TL sub-5fs laser pulses. The dotted curve shows the experimental pulse-shaper assisted IAC of the compressed pulses, while the solid gray line corresponds to the simulated IAC of perfectly TL pulses ($\varphi(\omega)$=0). The excellent agreement indicates successful and accurate spectral phase correction.

3.2.2. Compression of regeneratively amplified femtosecond laser pulses

This section describes MIIPS spectral phase correction of the amplified laser system described in section 2.1.2. Pulse shaper II (section 2.2) was placed between the laser oscillator and the regenerative amplifier to avoid damage to the SLM due to the high peak intensity of the amplified pulses (Figure 3.9). The goal in this case was to achieve TL pulses after focusing the beam with a 5X a microscope objective, as will be required for the experiments described in chapter 6. The SHG crystal was placed ~1 cm before the

focal plane of the objective to avoid damage to the crystal. In contrast to the SHG separation device required for pulse compression of ultrabroad-bandwidth pulses described previously, in this case a BG40 filter was enough to block the fundamental light while allowing the transmission of SHG light, as shown in the setup depicted in Figure 3.9. The SHG light was collected with an optical fiber and directed to a spectrometer (USB4000, Ocean Optics Inc.).

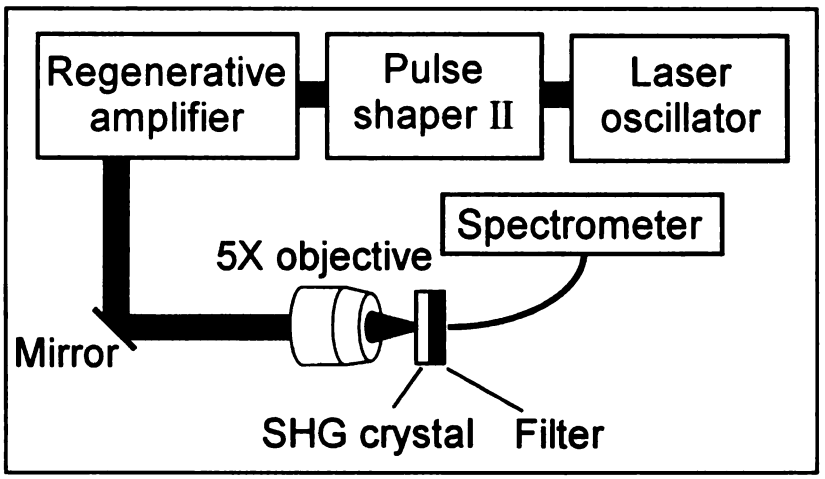

Figure 3.9. Optical setup for MIIPS spectral phase correction of the Ti:Sa regenerative amplifier laser system. The pulse shaper was placed between the laser oscillator and the regenerative amplifier. The amplified pulses were focused with a 5X microscope objective ~1 cm after the SHG crystal to avoid damaging the crystal. The fundamental light was blocked with a filter and the SHG light was collected with an optical fiber and directed to the spectrometer.

Pulse compression for this laser system was performed routinely. Typically, the built-in grating-based compressor in the amplifier was used to precompress the quadratic component of the spectral phase distortions by varying the grating position until the SHG spectrum was maximized at ~400nm. After this precompression step, MIIPS was used to measure and correct the spectral phase. Figure 3.10 shows a representative measured spectral phase together with the spectrum of this laser system. Note that the measured

phase is a cubic function as expected because the quadratic component of the phase distortion introduced by the microscope objective was previously compensated with the grating compressor. After phase correction, ~45 fs TL pulses were obtained and used for the experiments described in chapter 6.

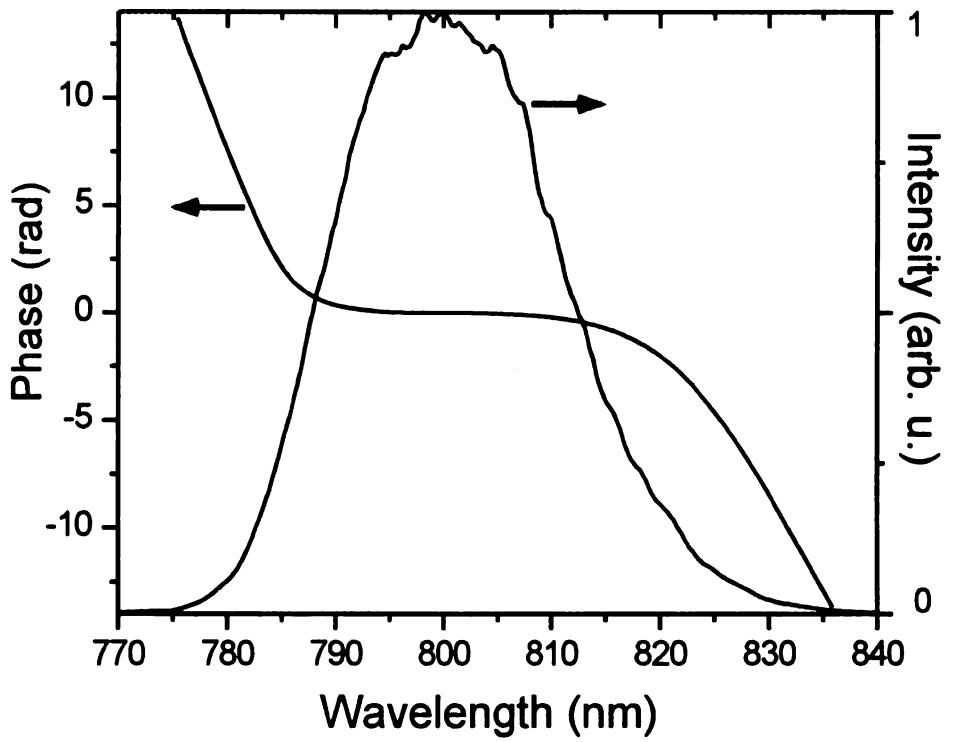

Figure 3.10. MIIPS measurement of the spectral phase distortion introduced by a 5X microscope objective on amplified femtosecond laser pulses. The fundamental spectrum and measured spectral phase are shown. The phase is close to a cubic function because the grating-based compressor in the amplifier was used to correct the quadratic component of the overall phase distortion introduced by the 5X microscope objective. After compensating the measured phase, 45 fs TL pulses were obtained.

3.3 Conclusions

Spectral phase distortions on ultrabroad-bandwidth femtosecond laser pulses, including those introduced by material dispersion, were accurately measured using MIIPS. As a result, these pulses were compressed to their TL duration of 4.3 fs. This challenging example illustrates MIIPS compression performance, which allows taking

advantage of the use of sub-50 fs pulses in a variety of applications, including nonlinear imaging.

Chapter 4

Chromatic dispersion measurements with MIIPS

Knowledge of the dispersion characteristics of optical media is necessary for pulse propagation models. For instance, the dispersion parameters of certain biological tissue allow calculating the amount of temporal broadening that a pulse will suffer after traveling through the tissue. Similarly, the amount of pulse precompression required to achieve TL pulses after propagation through the tissue can be calculated if the dispersion parameters are known. This chapter demonstrates how accurate dispersion measurements of optical media can be obtained using MIIPS. The utility of this kind of measurement is not only important for nonlinear imaging applications of femtosecond laser pulses. For this reason, example measurements relevant for other areas such as surgery are considered here.

The content of this chapter has been adapted from Y. Coello, B. Xu, T. L. Miller, V. V. Lozovoy and M. Dantus. "Group-velocity dispersion measurements of water, seawater, and ocular components using multiphoton intrapulse interference phase scan (MIIPS)". Appl. Optics 46, 8394 (2007) [66].

The increased use of femtosecond lasers requires more accurate measurements of the dispersive properties of media. Here we measure the second and third order dispersion of water, seawater, and ocular components in the range 660-930 nm using MIIPS. Our direct dispersion measurements of water have the highest precision and accuracy to date. We found that the dispersion for seawater increases proportionally to the concentration of salt. The dispersion of the vitreous humor was found to be close to

that of water. The chromatic dispersion of the cornea-lens complex was measured to obtain the full dispersive properties of the eye.

4.1. Introduction

The growing number of femtosecond lasers in industry, medicine, and communications has increased the need for measuring the dispersive properties of media beyond that of glass and quartz. Because of their broad bandwidth, femtosecond lasers are particularly sensitive to chromatic-dispersion characteristics of materials, in particular second-order (k'') and third-order dispersion (k'''), which typically cause pulse broadening.

Pulse duration is a very important parameter in femtosecond laser applications, for example laser micromachining and laser eye surgery, because it determines the peak power density available to ablate the material. If substantial broadening takes place, the ability of the laser to achieve consistent ablation is greatly diminished. In this article we carry direct measurements on the chromatic dispersion of water, seawater, and ocular components.

Femtosecond lasers are routinely used for opening the corneal flap in the bladeless LASIK technique. A number of additional procedures are presently under investigation. In vitro experiments have shown that femtosecond laser ablation may be useful for the treatment of glaucoma by making channels through the trabecular meshwork in the eye without damaging the surrounding tissues. These channels provide a pathway for the release of fluid and may result in a significant intraocular pressure reduction *in vivo* [67]. Femtosecond laser surgery on retinal lesions appears to be a promising treatment for macular degeneration [68]. More recently, intratissue multiphoton ablation in the cornea

has been demonstrated opening the possibility of treating visual disorders without the need of corneal flaps as used for LASIK [69]. Femtosecond laser cuts in the lens without damaging adjacent tissue is being developed for the treatment of presbyopia, a very common disease with no satisfactory treatment presently available [70, 71].

All of the applications above can be greatly improved using the shortest femtosecond laser pulses, taking advantage of the reduced energy required to achieve a specific peak power density. Less energy implies less collateral damage to healthy tissue. However, sub-50-fs pulses undergo significant broadening by transmitting through optical media including ocular components. Therefore, accurate dispersion measurements and a means to eliminate phase distortions, as presented here, will be required to consistently achieve the best results. Conversely, from the point of view of laser eye safety, femtosecond pulses that achieve their shortest duration at the retina pose the greatest risk [72].

We start our discussion by remembering that the wavenumber is defined by $k \equiv \omega n(\omega)/c \equiv 2\pi n(\lambda)/\lambda$, where ω is the angular frequency of light, n is the refractive index of the medium, c is the speed of light in vacuum, and λ is the free-space wavelength of light. The phase retardation that light with frequency ω experiences is given by $\varphi(\omega)=k(\omega)z$, where z is the path length traveled by the light. As a broad-bandwidth femtosecond laser pulse propagates, it undergoes chromatic dispersion ($\varphi'' \equiv d^2\varphi/d\omega^2$), second-order dispersion ($k'' \equiv d^2k/d\omega^2$), and third- order dispersion ($k''' \equiv d^3k/d\omega^3$). For a Gaussian pulse the second-order dispersion k'' is equal to the group-velocity dispersion (GVD$\equiv d(1/\upsilon_g)/d\omega$, where υ_g is the group velocity) [73]. The chromatic dispersion φ'' for a Gaussian pulse is also known as group-delay dispersion (GDD).

Another common definition of group-velocity dispersion is the derivative of the group velocity with respect to wavelength $d\upsilon_g/d\lambda$. This is sometimes a source of confusion because the strictest definition of group-velocity dispersion is $d\upsilon_g/d\omega$. According to either of these definitions the group-velocity and group-delay dispersion are not only functions of the media but also functions of the shape of envelope of the field. Here, we measure φ'' and k'', which depend on the media only.

While the refractive index of materials can be directly measured using a hollow prism arrangement [74], the measurement of k'' is more difficult. It can be calculated using an analytical formula for the index of refraction according to

$$k''(\lambda) = \frac{\lambda^3}{2\pi c^2} \frac{d^2 n(\lambda)}{d\lambda^2} . \tag{4.1}$$

However, because derivatives are very sensitive to noise and more importantly depend on the phenomenological formula used to fit the data, this indirect method has unpredictable precision and accuracy. One of the most accurate methods used to measure dispersive properties is white-light interferometry, where an interferometer is constructed using a broad-bandwidth source of light and the material is introduced in one of the arms [75]. In this case, the phase distortions introduced in the sample arm can be measured directly, and usually after decomposition in a Taylor series, the second derivative φ'' can be extracted. There is also a variety of time-of-flight, phase-shift, interferometric measurement techniques [76]. These methods are limited by their temporal resolution and are time-consuming because they depend on wavelength and/or time scans.

Here we report on the use of MIIPS to measure the second-order dispersion k'' of deionized water and compared it to literature values. We then measured the dependence

of k'' on the concentration of sea salt in water and k'' of the ocular vitreous humor. Finally we measured φ'' of the cornea-lens complex. These two eye components together, the vitreous humor and the cornea-lens complex, account for all the transparent parts of the eye.

4.2. Experimental section

For these experiments we used the ultrabroad-bandwidth femtosecond laser oscillator (section 2.1.1), pulse shaper I (section 2.2) and the SHG generation, separation and detection device described in section 3.1. The detailed setup is shown in Figure 3.1. The laser system used provides measurements of chromatic dispersion in the very broad spectral range without tuning the laser or realigning the optical system.

Before making the measurements, it is important that phase distortions, including those introduced by empty glass cuvettes or slides, are eliminated using MIIPS. Once the phase distortions of the system are eliminated, the desired medium with thickness z is introduced, as shown in Figure 4.1, and its chromatic dispersion φ'' as function of wavelength or frequency is measured using MIIPS.

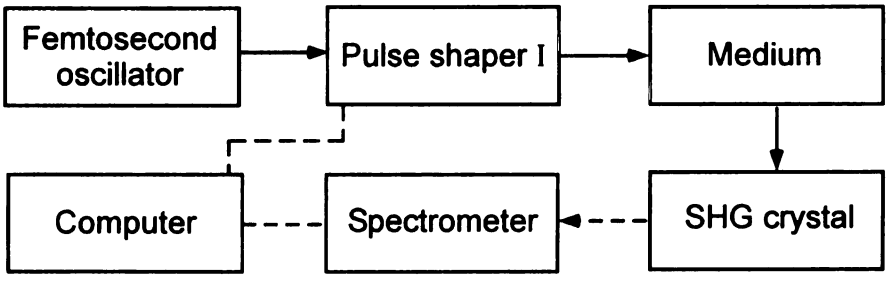

Figure 4.1. Block diagram of the experimental setup for MIIPS GVD measurements. The solid and dashed arrows indicate the propagation of the laser and SHG beam, respectively; the dashed lines indicate computer communication.

An example measurement is presented in Figure 4.2a for the case of different path lengths of water. The lines in Figure 4.2a correspond to a fit of the experimental data set

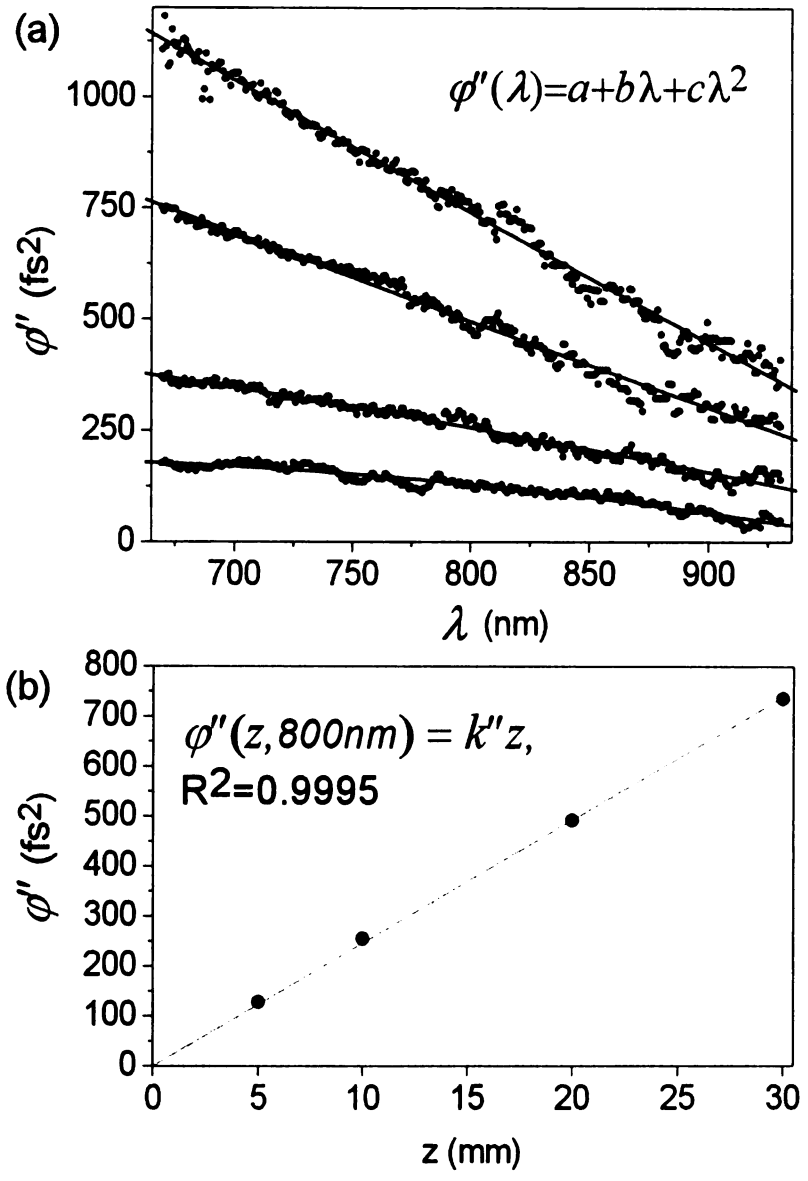

Figure 4.2. Chromatic dispersion as a function of medium thickness. (a) $\varphi''(\lambda)$ data points measured by MIIPS and second-order polynomial fits for water samples of 5, 10, 20 and 30 mm thickness (ascending order). (b) Linear regression of $\varphi''(\lambda)$ at 800 nm.

containing hundreds of points to $\varphi''(\lambda)=a+b\lambda+c\lambda^2$. We confirmed that the results are independent from the fitting function selected. In the MIIPS measurements of φ''we used

γ = 6 fs and α=2π (see section 2.3). For large phase distortions, the first MIIPS iterations were carried out with larger α values (up to 10π), and as the distortions were eliminated, α was reduced. The δ parameter was scanned across the 4π rad range in 128 steps.

Given that the chromatic dispersion varies linearly with the sample thickness, $\varphi'' = k''z$, the second-order dispersion $k''(\lambda)$ was calculated from the slope of the dependence at each wavelength (see Figure 4b). The error bars reported for k'' correspond to the standard deviation of the slopes for three sets of independent experiments.

Deionized water with a room-temperature mean conductivity of 2μS/cm was used in all cases. Artificial seawater was prepared by dissolving Instant Ocean© sea salt in deionized water with concentrations of 35.8 g/L and 107.4 g/L for the 1x and 3x samples respectively. Four glass cuvettes with path lengths of 5, 10, 20 and 30 mm were used for the water and seawater measurements. Fresh (uncured) adult about 18-month-old Holstein cow eyes, that would have otherwise been discarded, were obtained from a slaughterhouse. The vitreous humor was extracted and three glass cuvettes with path lengths of 5, 10, and 20 mm were used for the measurements. A cow cornea-lens complex was extracted and squeezed to approximately 5 mm of thickness with glass slides for the measurements.

4.3. Results

4.3.1. Chromatic dispersion of deionized water

Measurements of $k''(\lambda)$ are presented in Figure 4.3b together with a comparison to earlier measurements and results of calculations based on the knowledge of the index of refraction as a function of frequency. The black dots represent our measurements, the open dots represent measurements using white-light interferometry [77], the solid line

corresponds to the calculated $k''(\lambda)$ values based on a Sellmeier's approximation for the refractive index of distilled water [74], and the dashed line corresponds to the calculated $k''(\lambda)$ values based on a polynomial formula for the refractive index of water adopted by the National Institute of Standards and Technology (NIST) of the USA [78].

Figure 4.3a shows the deviation of the experimental measurements from the calculated dispersion based on the Sellmeier formula (line). Below we provide the Sellmeier formula (Equation 4.2) and the parameters provided by Daimon and Masumura [74] used for our calculations of k'' using Equation 4.1.

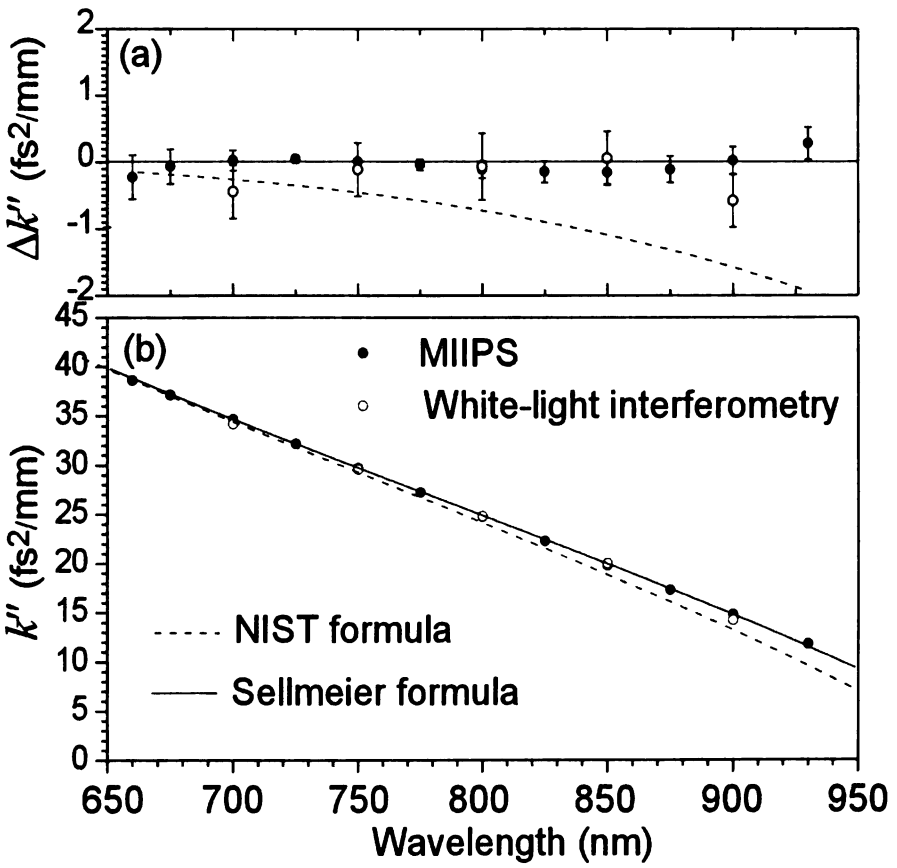

Figure 4.3. Comparison of k'' for water measured by MIIPS and white-light interferometry and calculated using the Sellmeier and NIST dispersion formulas. The upper graph shows the difference of the corresponding values with respect to those calculated using the Sellmeier dispersion formula. For both calculations a temperature of 21.5°C was used.

$$n^2 - 1 = \sum_{i=1}^{4} \frac{A_i}{1 - (\lambda_i / \lambda)^2}, \qquad (4.2)$$

where A_i and λ_i can be associated with effective resonances and are collected in Table 4.1.

Table 4.1. Parameters of the Sellmeier formula for water at 21.5°C

i	A_i	λ_i (nm)
1	0.5689093832	71.486374884
2	0.1719708856	135.099228532
3	0.02062501582	161.992558595
4	0.1123965424	3267.269774598

Experimental values of k'' for water at selected wavelengths are shown in table 4.4.

Based on the measured second-order dispersion we can calculate the third-order dispersion as $k'''(\omega)=dk''/d\omega$. The result of this calculation is presented in Figure 4.4

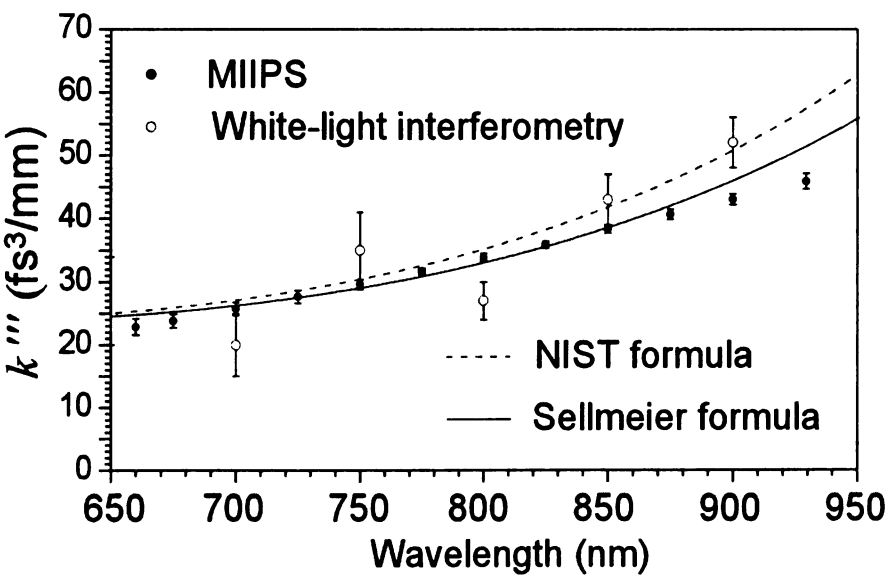

Figure 4.4. Comparison of water third-order dispersion calculated from our measurements, the Sellmeier and NIST dispersion formulas, and obtained using white-light interferometry.

together with the corresponding measurements by white-light interferometry [77] and the calculation based on the Sellmeier [74] and NIST dispersion formulas [78].

4.3.2. Chromatic dispersion of seawater

A difference between the k''s of water and seawater was measured, and the results are shown in Figure 4.5. Furthermore, we found that the increase in k'' when salt is added, $\Delta k''(S)=k''(S)-k''(S=0)$, is directly proportional to the salinity (S) and independent from wavelength. This direct proportionality can also be derived from the formula for the refractive index of seawater proposed by Quan and Fry [79]. They fit the experimental refractive index data for seawater measured by Austin and Halikas [80] to a ten-term empirical formula in the wavelength range 400-700 nm and salinity range 0-35 g/L. The

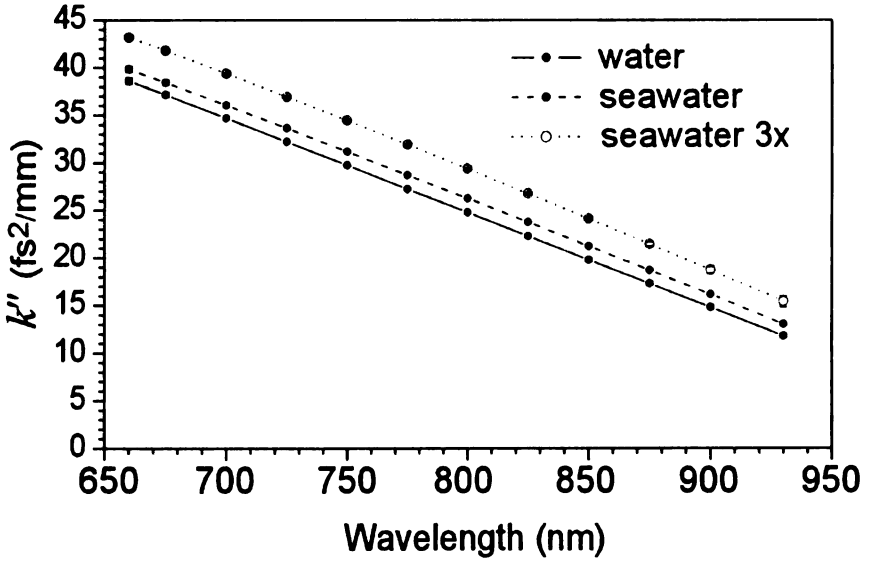

Figure 4.5. Experimental measurements of k'' of water, seawater, and water with 3 times the concentration of salt in seawater (3x). Only a few experimental points were plotted for clarity.

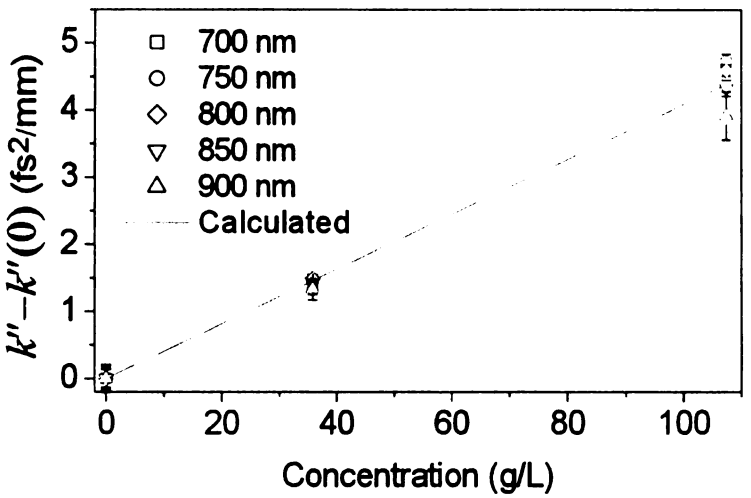

Figure 4.6. Increase in k'' of seawater with respect to deionized water as a function of the concentration of sea salt. The symbols correspond to MIIPS measurements and the line to a calculation based on the refractive index formula for seawater proposed by Quan and Fry. For the calculation the temperature was set at 21.5°C. Note that the calculation has been extended beyond the original range of validity for S (~35 g/L).

resulting formula contains only one term proportional to S and λ ($n(\lambda) \propto S/\lambda$). Since $k''(\lambda) \propto \lambda^3 d^2 n(\lambda)/d\lambda^2$ the formula predicts that $\Delta k''(S)$ is directly proportional to S and independent from λ. In Figure 4.6, we compare the effect of salinity on k'' measured by MIIPS with that calculated using the refractive index formula for seawater in [79].

There seems to be a need for a formula that correctly predicts the wavelength and salinity dependence of k''. We propose that $k''(\lambda)$ can be expressed as follows

$$k''(\lambda) = C_0 + C_1\lambda + C_2\lambda^2 + C_S S, \qquad (4.3)$$

where the coefficients C_0, C_1 and C_2 were calculated from experimental data for deionized water (see Figure 4.5) and the coefficient C_S was calculated using a linear regression for $\Delta k''(S)$ (see Figure 4.6). The parameters of the fit are given in Table 4.2. These values and the errors were calculated using the Origin 6.1 software (OriginLab

Corporation). Experimental values of k'' for seawater at selected wavelengths are shown in table 4.4.

Table 4.2. Seawater parameters for Equation 4.3 in the range 660-930 nm.

C_0	102.42174 ± 0.46809 fs^{2}mm^{-1}
C_1	-0.09476 ± 0.00118 fs^{2}mm^{-1}nm^{-1}
C_2	$-2.88686\times10^{-6} \pm 0.74132\times10^{-6}$ fs^{2}mm^{-1}nm^{-2}
C_S	0.04008 ± 0.00157 fs^{2}mm^{-1} g^{-1} L

4.3.3. Chromatic dispersion of the vitreous humor and the cornea-lens complex

Ocular dispersion data are particularly scarce for near-infrared wavelengths [81, 82]. To help remedy this lack of information we measured the dispersive properties of all the transparent components of the eye, the cornea-lens complex and the vitreous humor (Figure 4.7).

We found that the second-order dispersion k'' of the vitreous humor is very close to that of water, as it is shown in Figure 4.8. The data were fit to a second-order polynomial (Equation 4.4). The parameters of the fit are shown in Table 4.3. Experimental

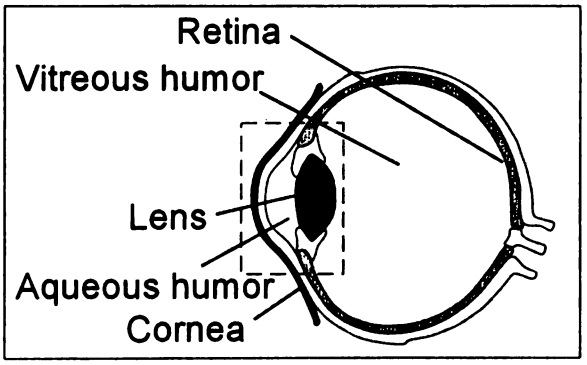

Figure 4.7. Diagram of an eye. The dashed square corresponds to the cornea-lens complex.

measurements of k'' for the vitreous humor at selected wavelengths are shown in Table 4.4.

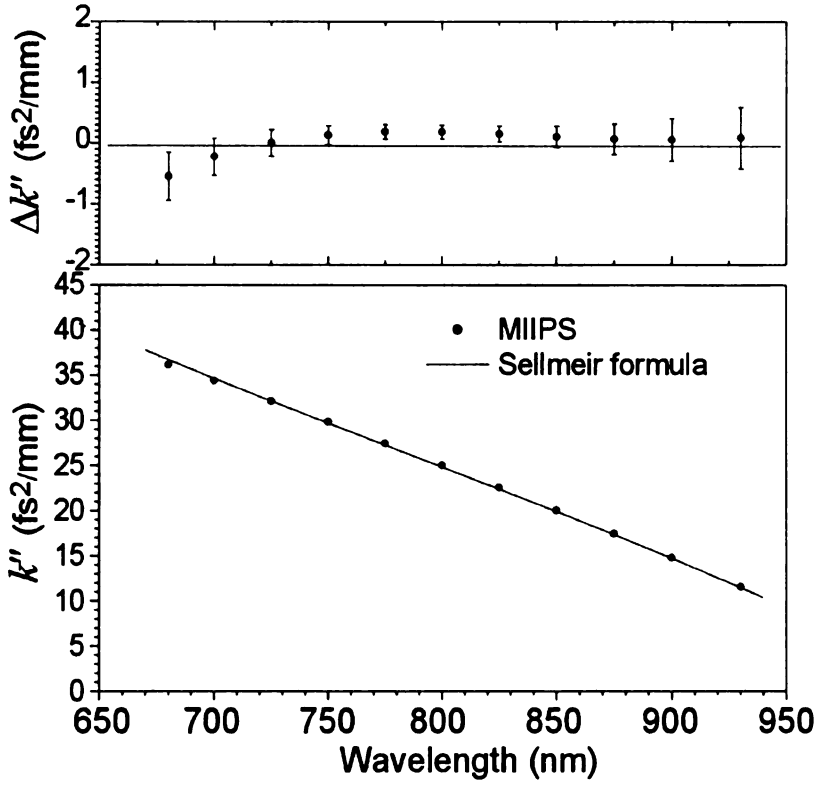

Figure 4.8. Comparison of k'' for the vitreous humor measured by MIIPS and k'' for water calculated using the Sellmeier dispersion formula for distilled water. The upper graph shows the deviation of the vitreous humor measurements with respect to the calculated values for water.

$$k''(\lambda) = C_0 + C_1\lambda + C_2\lambda^2, \qquad (4.4)$$

Table 4.3. Vitreous humor parameters for Equation 4.4 in the range 660-930 nm.

C_0	76.04648 ± 1.52198 fs^2mm^{-1}
C_1	-0.02954 ± 0.00382 $fs^2mm^{-1}nm^{-1}$
C_2	-4.27553x10^{-5} ± 0.239476x10^{-5} $fs^2mm^{-1}nm^{-2}$

The measured chromatic dispersion φ'' of a cornea-lens complex is shown in Figure 4.9. For this experiment we were not able to use different path lengths. The data presented come from a set of three measurements on the same tissue. Values of φ'' for the cornea-lens complex at selected wavelengths are shown in table 4.4. From our data we obtain a value of 33 fs^2/mm for $k''(\lambda=800\ nm)$

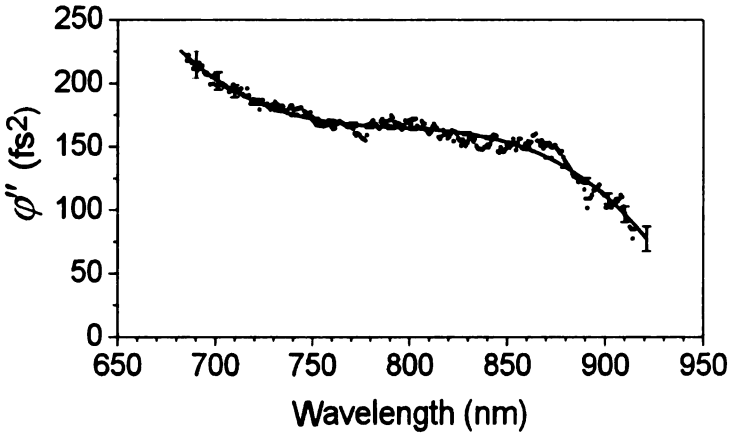

Figure 4.9. Measured chromatic dispersion φ'' of a cornea-lens complex. The dots correspond to the experimental points. The line corresponds to a third-order polynomial fit of the data.

Table 4.4. Experimental dispersion measurements for water, seawater and eye components.

Wavelength (nm)	Water k'' (fs^2/mm)	Seawater k'' (fs^2/mm)	Vitreous humor k''(fs^2/mm)	Cornea-Lens φ'' (fs^2)
660	38.62 ± 0.33	39.85±0.31	-	-
675	37.14 ± 0.26	38.42 ± 0.26	36.63 ± 0.42	-
700	34.67 ± 0.15	36.03 ± 0.19	34.42 ± 0.31	203 ± 7
725	32.20 ± 0.06	33.61 ± 0.14	32.16 ± 0.22	183 ± 2
750	29.72 ± 0.02	31.18 ± 0.09	29.84 ± 0.16	172 ± 1
775	27.25 ± 0.08	28.72 ± 0.06	27.47 ± 0.12	167 ± 2
800	24.76 ± 0.13	26.25 ± 0.04	25.05 ± 0.11	164 ± 1
825	22.28 ± 0.16	23.75 ± 0.03	22.58 ± 0.13	161 ± 1
850	19.79 ± 0.18	21.23 ± 0.03	20.05 ± 0.18	153 ± 1
875	17.29 ± 0.20	18.69 ± 0.05	17.47 ± 0.25	137 ± 1
900	14.80 ± 0.21	16.14 ± 0.09	14.83 ± 0.35	111 ± 4
930	11.79 ± 0.24	13.04 ± 0.14	11.60 ± 0.51	-

4.4. Discussion

4.4.1. Chromatic dispersion of deionized water and seawater

Analysis of our experimental results for water clearly shows excellent agreement with the calculations based on the Sellmeier model (Equation 4.2). The deviation between our measurements and the calculated values based on this model are smaller than 0.2 fs^2/mm within the measured wavelength range, and for some of the points, the deviation is even lower than 0.1 fs^2/mm. Note that using the refractive index formula adopted by NIST to calculate the second-order dispersion leads to values which considerably deviate from experimental measurements and calculations based on Equation 5. We conclude that MIIPS provides precision and accuracy at least two times better than white-light interferometry.

There is also a surprisingly good agreement between our experimental measurements for seawater and the calculations based on the formula for the refractive index of seawater in [79], considering that this was derived for a different range of wavelengths and for a much smaller range of salinity.

4.4.2. Chromatic dispersion of the vitreous humor and the cornea-lens complex

Having measured the chromatic dispersion of the ocular components, we can now predict pulse broadening. If an initial TL Gaussian pulse of time duration τ_0 and centered at λ_0 acquires a chromatic dispersion $\varphi''=\varphi''(\lambda_0)$ after propagating through a dispersive medium, then its final pulse duration is

$$\tau = \tau_0 \left[1 + \left(4\varphi'' \tau_0^{-2} \ln 2 \right)^2 \right]^{0.5}, \qquad (4.4)$$

[73]. For a human eyeball we estimate that $\varphi'' = k_h'' z + \varphi''_c$, where k''_h is the second-order dispersion of the vitreous humor, $z = 20$ mm is the path length that light travels inside the vitreous humor, and φ''_c is the chromatic dispersion of the cornea-lens complex. For initial 10-fs and 50-fs TL pulses centered at 800 nm, using Table 4.4 and Equation 4.4, we find that $\varphi'' \approx 665$ fs^2 and that the pulse durations at the retina would be 185 fs and 62 fs respectively. From this, we can also learn that sub-50-fs pulses with $\varphi'' \approx -665$ fs^2 pose the greatest eye laser safety risk.

Pulse broadening is important because peak power densities at the target are inversely proportional to the time duration of the pulses. For example, if one focuses a 10-fs 1-μJ pulse to 10 μm^2, the peak power density would be 10^{15} W/cm^2. This extreme power density causes the desired localized ablation without collateral damage. If the time duration increases ten times, the peak intensity is reduced in an order of magnitude, and the ablation ability of the pulses decreases.

We want to point out that we performed calculations of k'' for human vitreous humor based on several proposed refractive index formulas [82-84]. These calculations lead to values of $k''(\lambda=800nm)$ that deviate from 7 fs^2/mm to 20 fs^2/mm from our experimental measurements at 800 nm. The difference between measured and calculated values comes from the fact that the k'' calculation is highly dependent on the formula used to fit the refractive index data (see formula 1).

4.5. Conclusions

We introduced a new direct method to measure the chromatic dispersion of transparent media. Comparison of our data with other measurements suggests that the accuracy and precision of our method are the most reliable to date. Knowledge of the reported chromatic dispersion measurements of water and seawater is necessary for laser propagation models in these media. The chromatic dispersion for ocular components will be useful for laser eye surgery and laser safety data guidelines. The measurement and elimination of chromatic dispersion (second and higher orders) as shown here, using MIIPS, is highly recommended for the highest reliability and reproducibility of applications using femtosecond pulses.

Chapter 5

High-resolution two-photon fluorescence excitation spectroscopy by pulse shaping ultrabroad-bandwidth femtosecond laser pulses

A fast and automated approach to measure two-photon fluorescence excitation (TPE) spectra of fluorophores with high resolution (~5 nm) by pulse shaping ultrabroad-bandwidth femtosecond laser pulses is demonstrated. Selective excitation in the range 680-990 nm was achieved imposing a series of specially designed phase-amplitude masks on the pulses using a Fourier-transform pulse shaper. The method eliminates the need of laser wavelength tuning and is thus suitable for non-laser-expert use. The TPE spectra of the pH-sensitive dye 8-hydroxypyrene-1,3,6-trisulfonic acid (HPTS) in acidic and basic environments were measured for the first time using this approach.

5.1. Introduction

Simultaneous two-photon absorption (TPA) by an atom or molecule was first predicted by Maria Goeppert-Mayer in 1931 [85], although the first experimental demonstration of this phenomenon had to wait 30 years until the development of lasers [3]. Two-photon (TP) spectroscopy has been of interest to study the electronic structure of molecular excited states [86] because TPA selection rules are different than those for the one-photon case. TP induced fluorescence resulted very valuable in the biological imaging field. In 1990, Denk and Webb developed two-photon laser scanning fluorescence microscopy (TPLSM) [5], a technique that takes advantage of the high photon density required to overcome the low probability for the simultaneous absorption of two photons. In TPLSM, TPA and fluorescence emission occur only at the beam focus. Consequently, intrinsic three-dimensional resolution is obtained, out-of-focus

background fluorescence is eliminated, and photobleaching is reduced, among other advantages over wide-field and one-photon confocal laser scanning fluorescence microscopy [6, 87]. TPLSM has become a widely used tool for medical and biological research and as a result commercial TP microscopes have been available for a number of years. The TP spectra of fluorophores are required to determine which are suitable for this technique and for quantitative TPLSM studies. More recently, TPA is also becoming relevant for photodynamic therapy [88-90]. The development of new compounds with tailored TPA properties and well-characterized TP spectra is of outmost importance for the development of these applications. Consequently, the measurement of TP cross sections has become critically important. For instance, a high TP cross section indicates that the compound absorbs a relatively high fraction of the light focused on the sample, minimizing possible photodamage to the surroundings.

The techniques commonly used to measure TP cross-sections of materials can be divided in two groups. One group is based on nonlinear transmission measurements [91-93]. These techniques directly yield the TPA cross-section σ_{TPA} and can be applied to non-fluorescent materials, but their implementation is often difficult given that only a very small fraction of photons from the excitation beam is absorbed as it passes through the sample. The second group relies on TP induced fluorescence measurements and provides better sensitivity [9, 94-98]. In most cases, these techniques yield the TPE cross-section σ_{TPE}, which is directly proportional to the TPA cross-section σ_{TPA} with the constant of proportionality being the fluorescence quantum efficiency η (i.e., $\sigma_{TPE}=\eta\sigma_{TPA}$). Although Fourier-transform methods have been reported [99, 100], the measurement of TPE spectra has been typically performed by selectively exciting the

sample with a narrow-bandwidth laser source, recording the resulting TP induced fluorescence, tuning the laser wavelength and repeating the process for all the desired wavelengths. Using this approach, a valuable database of TPE spectra of several commercial organic dyes widely used in TPLSM was reported in the late 1990's using a tunable femtosecond laser for selective excitation from 690 to ~1000 nm [8, 94]. More recently, an extended collection of spectra have been measured in a broader spectral range using an optical parametric amplifier (OPA) [9]. Determination of TPE spectra can be significantly simplified using a standard calibration sample with well-known TPE cross-sections. In this case, several measurements of experimental parameters required for absolute cross-section measurements are avoided [8, 101, 102].

Here, a fast and automated approach able to measure TPE spectra of fluorophores with high resolution is demonstrated. The method employs shaped ultrabroad-bandwidth femtosecond laser pulses to achieve selectively excitation of the sample. The approach eliminates the need of laser wavelength tuning and is thus suitable for non-laser-expert use, especially now that Fourier-transform pulse shapers are commercially available.

5.2. Experimental part

5.2.1. Optical setup

For these experiments we used the ultrabroad-bandwidth femtosecond laser oscillator (section 2.1.1) together with pulse shaper I (section 2.2). This laser system covers the most relevant wavelength region for TPLSM (620-1050 nm).

The second-order nonlinear spectrum $S^{(2)}(\omega)$ of the shaped pulses was characterized by measuring the corresponding second-harmonic generation (SHG) spectrum [16]. For

this purpose, the SHG generation, separation and detection device described in section 3.1 was used.

To measure the TP induced fluorescence, the beam from the pulse shaper was focused on the sample solution, which was placed in a 2-mm-path-length quartz cell, using a 50-mm-focal-length spherical mirror. The fluorescence was collected at 90° by a 40×, 0.6 NA microscope objective and was then focused on a silicon-avalanche-photodiode-based single-photon-counting module (SPCM-AQR-12, PerkinElmer) connected to a gated photon counter (Model SR400, Stanford Research Systems). A bandpass filter allowing the transmission of light in the fluorescence wavelength region (400-600 nm) was also used to filter light from other sources, including scattering of the fundamental pulses (Figure 5.1).

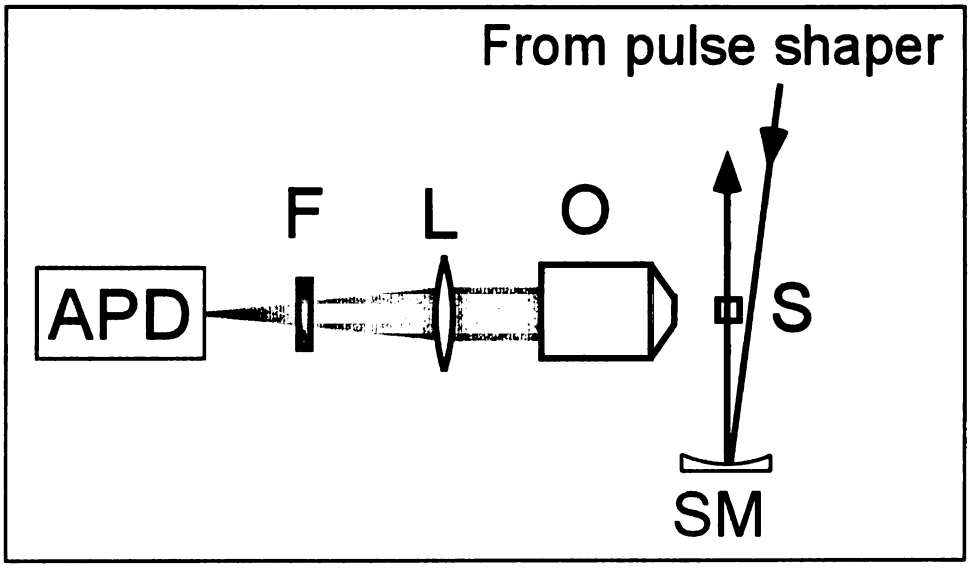

Figure 5.1. Two-photon induced fluorescence generation, collection and detection setup. The beam from the pulse shaper is focused onto the fluorescent solution (S), placed in a 2-mm-path-length quartz cell, using a spherical mirror (SM). The fluorescence signal was collected with a 40× objective (O) at 90° and focused onto the avalanche photodiode (APD) detection unit with a lens (L). A bandpass filter (F) allowing the transmission of fluorescence light was placed before the detection system.

For all the experiments, spectral phase distortions of the optical system were measured and corrected at the sample position using MIIPS before the designed phase-amplitude masks were imposed on the pulses using the shaper. Uncorrected phase distortions, such as those introduced by the 40× microscope objective, would reduce the generated TP induced fluorescence due to the effect of phase modulation on $S^{(2)}(\omega)$ (see Section 1.2). Furthermore, variations in the phase distortions-, for instance, due to different oscillator settings or shaper alignment, require frequent phase correction procedures to ensure reproducibility in the measurements.

5.2.2. Sample preparation

HPTS 100 μM solutions at pH 6, 7, 8, 9 and 10, and a Fluorescein 100 μM solution at pH 13 were prepared by diluting ~10 mM stock solutions of the dye (Fluorescein and HPTS sodium salts, Fluka) in a buffer at the corresponding pH. Sodium tetraborate (EM Science) was used to prepare 50 mM buffers at pH 9 and 10(±0.1), and potassium phosphate monobasic (Mallinckrodt) was used to prepare 50 mM buffers at pH 6, 7, 8, and 13(±0.1). The pH of the solutions was measured with a pH-meter (Accumet Basic, Fisher Scientific) and adjusted using hydrocloric acid or sodium hydroxide solutions. Deionized water was used in all cases.

5.3. Results and discussion

Selective TP excitation in the range 680-990 nm was achieved with narrow-bandwidth laser pulses obtained by amplitude shaping. For this purpose, the pulse shaper was used to block all the wavelengths in the fundamental laser spectrum except those in a narrow spectral window around the desired excitation wavelength. Such a spectral

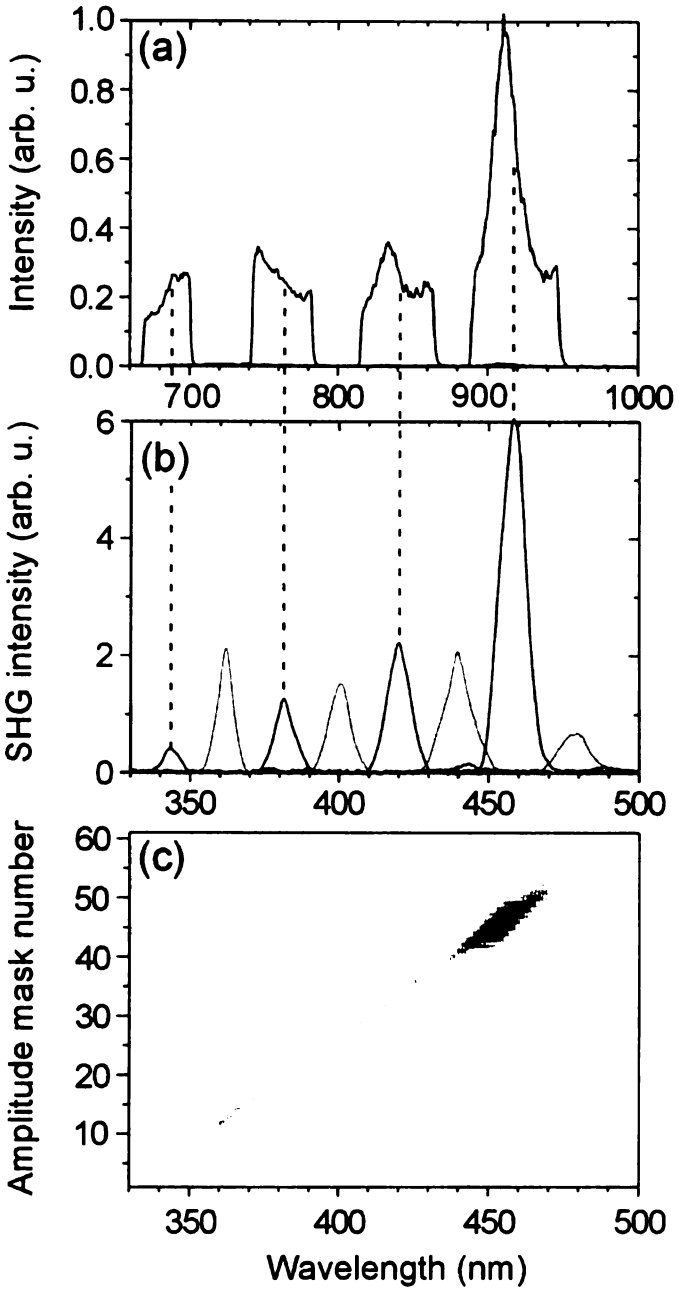

Figure 5.2. Selective two-photon excitation by amplitude shaping of ultrabroad-bandwidth femtosecond laser pulses. In this experiment the goal was to generate narrow-bandwidth second-order nonlinear spectra suitable for selective TP excitation. Experimental SHG spectra were used to characterize the second-order nonlinear spectra. Sixty amplitude masks evenly spaced across the fundamental spectrum of the pulses were used to generate the same number of narrow-bandwidth fundamental spectra. (a) Four of such spectra. (b) Eight of the narrow-bandwidth SHG spectra. The dashed lines indicate the correspondence between four of the fundamental and SHG spectra. (c) 2D contour plot showing the SHG spectra corresponding to the whole set of amplitude masks.

window is called an amplitude mask. Figure 5.2 illustrates the amplitude shaping approach. In this experiment, sixty amplitude masks evenly spaced across the available fundamental spectrum bandwidth were applied to the pulses. Figure 5.2a shows four of the resulting amplitude-shaped fundamental spectra, while Figure 5.2b shows eight experimental SHG spectra, which characterize the second-order nonlinear spectra of the pulses. Dashed lines indicate the correspondence between four of the fundamental and SHG spectra. The SHG spectra corresponding to the whole set of amplitude shaped pulses is shown in Figure 5.2c. A very high contrast ratio (CR) of ~13 (the ratio between the integral of the signal peak and the integral over the entire background) was achieved with this approach.

For the TP induced fluorescence experiments, narrower amplitude masks were used to obtain ~5 nm FWHM peaks in $S^{(2)}(\omega)$ that ensure high spectral resolution. For each amplitude mask centered at wavelength λ, the resulting TP induced fluorescence intensity $F(\lambda)$ was recorded. Figure 5.2 clearly shows that the intensity of $S^{(2)}(\omega)$ varies significantly due to the different fundamental spectral intensities and shapes. For this reason, a normalization procedure was used to obtain the relative cross-section $\sigma_{TPE}(\lambda)$ according to $\sigma_{TPE}(\lambda)=F(\lambda)/S^{(2)}(\lambda)$, where $S^{(2)}(\lambda)$ is the integrated intensity of the corresponding SHG spectrum. Absolute cross-sections, which are typically expressed in Goeppert-Mayer units (1 GM=10^{-50} cm^4 s/photon), can be obtained by comparison with a calibration standard [8].

First, fluorescent dyes with reported TPE spectra were studied. Figure 5.3 shows a comparison of TPE spectra of two commonly used fluorescent dyes measured using this

method and independently measured with a tunable femtosecond laser [8, 103]. The good agreement between the measurements reveals the accuracy of this approach.

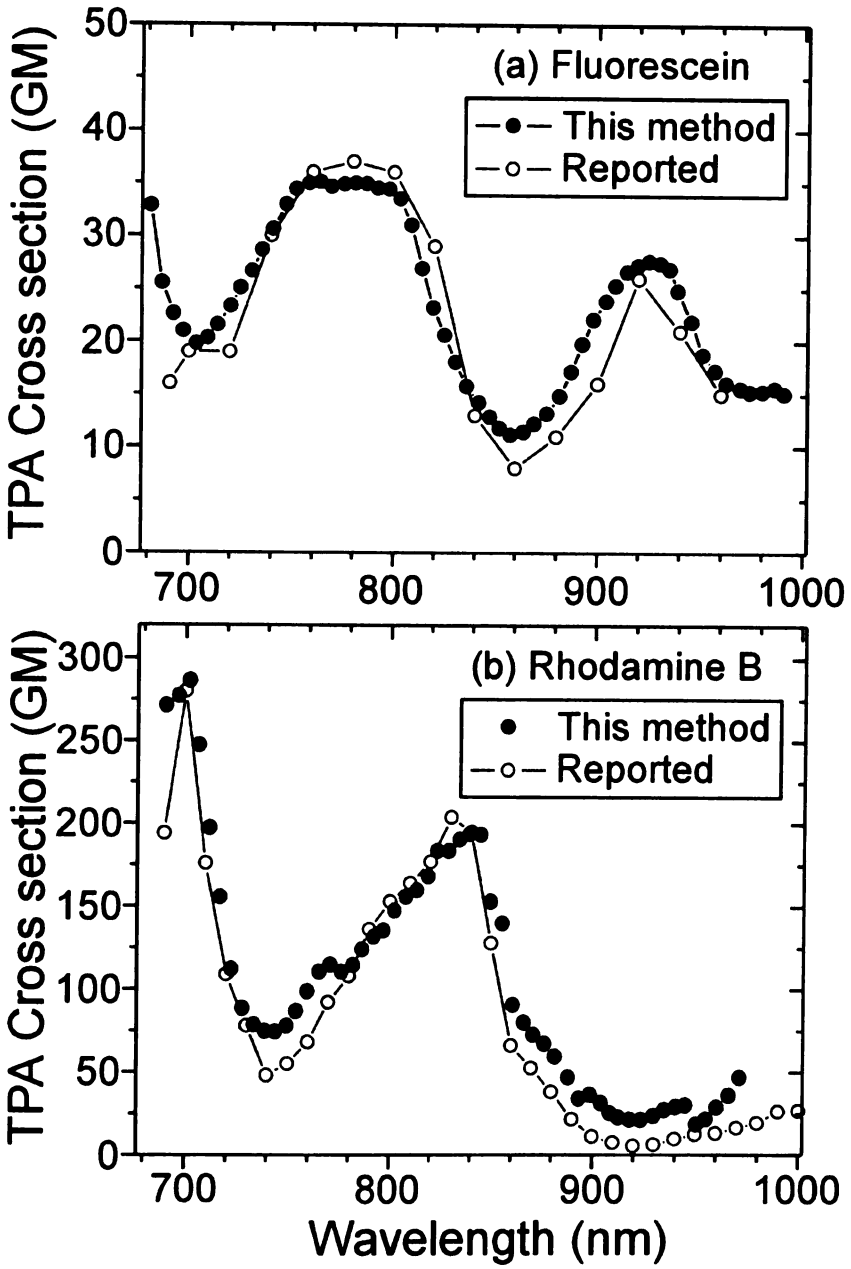

Figure 5.3. TPE spectra of Fluorescein and Rhodamine B. TPE spectra of (a) Fluorescein at pH 13 and (b) Rhodamine B in methanol measured with the method described here (black circles) and measured with a tunable femtosecond laser system as reported in [8] and [103], respectively (white circles). The agreement demonstrates the accuracy of this approach.

The fluorescent dye 8-hydroxypyrene-1,3,6-trisulfonic acid, commonly referred to as HPTS or pyranine (Figure 5.4a), exhibits (one-photon) absorption spectra highly dependent on pH (Figure 5.4b). Interestingly, the fluorescence spectra maximum occurs at 515 nm regardless of the pH because the pKa of the excited state decreases dramatically upon photoexcitation resulting in fast deprotonation. Thus, emission occurs only from the ionized form of the molecule. HPTS is stable, commercially available, highly soluble in various solvents and its pKa≈7.7 is conveniently near the pH of neutral aqueous solutions. These properties, in addition to its large Stokes' shift and high fluorescence quantum yield, make HPTS a useful pH-sensitive probe molecule [104, 105]. Nevertheless, HPTS pH dependent TPE spectra have not been reported yet.

In Figure 5.4c, the TPE spectra of HPTS at pH's 6, 7, 8 and 10 are shown. The data show very good agreement with a preliminary independent study [31] that measured the TPE spectra of HPTS at pH's 6 and 10, but in a much narrower spectral range (770-840 nm). Some correlations can be made between the peaks in the one-photon absorption spectra and those in the TPE spectra. The transition at 375 nm, characteristic the acidic form of HPTS, clearly appears at 750 nm in the TPE spectra. The transition at 405 nm, also characteristic the acidic form, can be observed at 810 nm in the TPE spectrum at pH 6. Finally, the transition at 455 nm, characteristic of the basic form of HPTS, clearly appears at 910 nm in the TPE spectra.

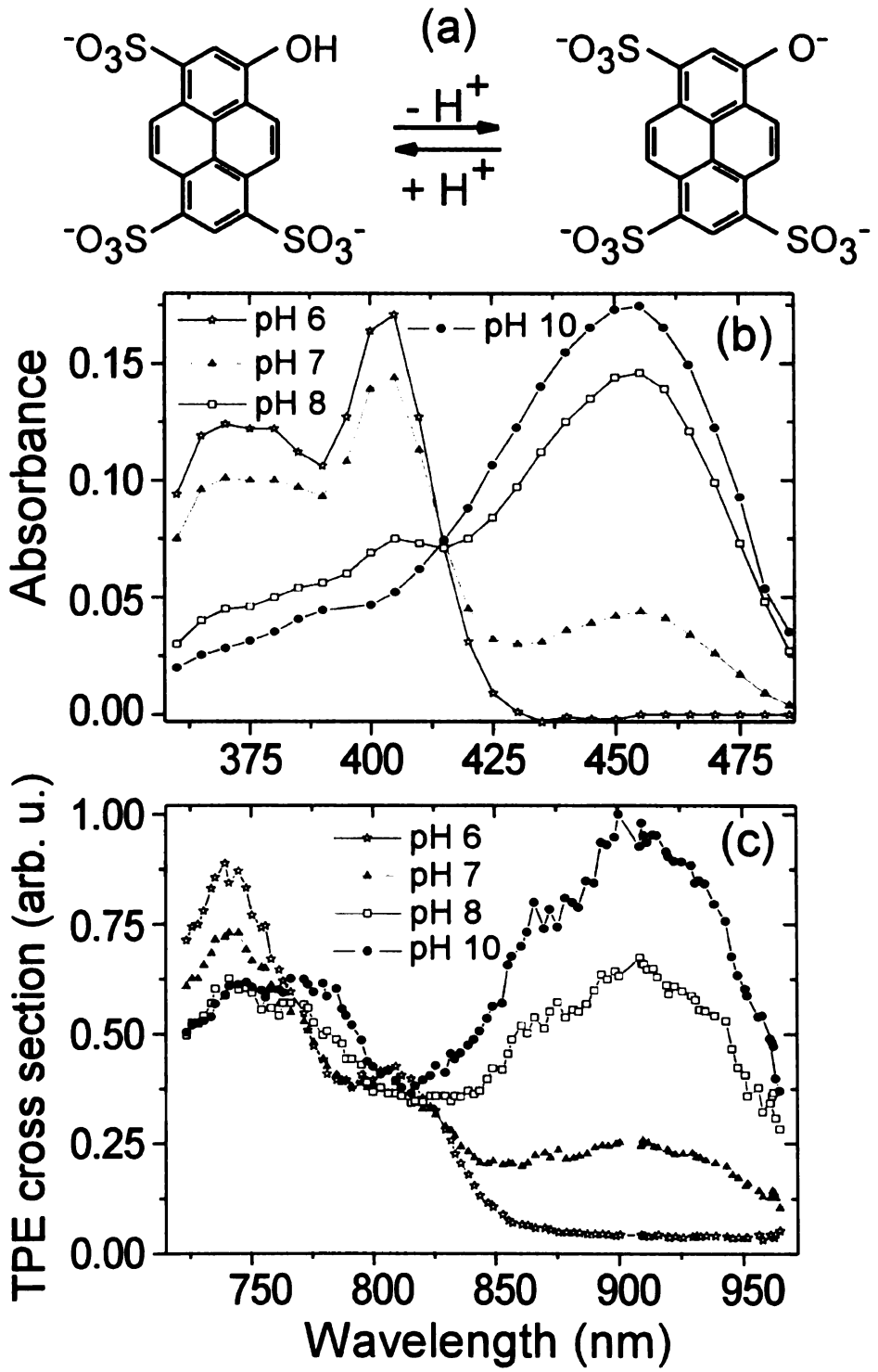

Figure 5.4. TPE spectra of HPTS in acidic and basic aqueous environments. (a) Acid-base equilibrium reaction of HPTS. (b) UV-visible absorption spectra of HPTS at pH's 6, 7, 8 and 10. The absorption maximum of HPTS changes from ~400 to ~450 nm upon deprotonation. (c) TPE spectra of HPTS at pH's 6, 7, 8 and 10. The one-photon transitions at ~375 and ~450 nm are clearly observed in the TPE spectra at 750 and 900 nm, respectively.

The spectrum acquisition time of this method is significantly shorter than that required by conventional approaches based on laser wavelength tuning. At the wavelength resolution used for these measurements (~5 nm) the acquisition of a TPE spectrum takes ~2 min, including the time required for SHG characterization.

The wavelength resolution of the presented measurements (~5 nm) is already higher than that of most reported TPE spectra measurements (10-20 nm). However, if a higher resolution were required, narrower peaks in $S^{(2)}(\omega)$ would have to be generated. These can be obtained using narrower amplitude masks. However, the amplitude shaping approach will become experimentally impractical when peaks in $S^{(2)}(\omega)$ with insufficient intensity are obtained. This will necessarily happen for all amplitude masks narrower than some critical spectral width given that the fundamental spectral intensity outside the amplitude mask is blocked and thus do not contribute to generation of $S^{(2)}(\omega)$. A more efficient approach, although also more involved, is to apply specially designed spectral phase functions able to generate constructive interference at the desired excitation frequency and simultaneously generate destructive interference everywhere else. Such phase functions can be designed guided by MII principles. For instance, sinusoidal spectral phases generate a peak in $S^{(2)}(\omega)$ at the frequency corresponding to the inversion center of the phase and low spectral intensity elsewhere (Section 1.2). Unfortunately, sinusoidal phase modulation cannot provide CRs greater than 0.5, and as the phase is tuned away from the central frequency the CR drops below 0.1 [106]. This CR may be insufficient for high-resolution TPE spectroscopy. A powerful phase shaping approach suitable for high-resolution nonlinear spectroscopy is briefly described next.

Narrow peaks in $S^{(2)}(\omega)$ can be generated using binary phase (BP) shaping, in which the spectral phase is limited to 0 and π values [31, 106, 107]. For an arbitrary phase, a peak in the SHG spectrum reaching maximum intensity will occur at a frequency $2\omega_c$ such that $\varphi(\omega_c-\omega)=-\varphi(\omega_c+\omega)$, as was demonstrated in Section 1.2. For BPs, the conditions $\varphi(\omega_c-\omega)=-\varphi(\omega_c+\omega)$ (antisymmetric phase) or $\varphi(\omega_c-\omega)=\varphi(\omega_c+\omega)$ (symmetric phase) are enough to maximize constructive interference and the SHG spectrum at $2\omega_c$ according to Equation 1.6. While any symmetric or antisymmetric BP will maximize the SHG spectrum at $2\omega_c$, the BPs required for selective TP excitation have to simultaneously maximize destructive interference in order to minimize the SHG spectrum at all frequencies different than $2\omega_c$. Destructive interference can be maximized using BPs with minimum autocorrelation [31]. To understand this point, assume that the magnitude of the field is unity for all frequencies and that the BP contains N bits. Then, the electric field E_j (j=1,2,...N) can only take −1 or +1 values and Equation 1.6 can then be rewritten as

$$S^{(2)}{}_k \propto \left| \sum_{i=0} E_{k-i} E_{k+i} \right|^2 \tag{5.1}$$

for k=1,2,...N, k-i≥1 and k+i≤N. Minimum autocorrelation BPs minimize the sum simply by introducing a similar number of +1 and −1 values into it. As a consequence, $S^{(2)}(\omega)$ is minimized at all frequencies. While the design of minimum-autocorrelation binary sequences requires significant effort, they are freely available thanks to research in the fields of communications engineering and statistical mechanics [108].

Figure 5.5 illustrates this BP approach applied to ultrabroad-bandwidth femtosecond laser pulses for the first time. First, a binary sequence with minimum autocorrelation is selected. In this case, the 13-bit binary sequence $\pi 0\pi 0\pi\pi 00\pi\pi\pi\pi\pi$ was used [108]. After symmetrization, the 26-bit binary sequence $\pi 0\pi 0\pi\pi 00\pi\pi\pi\pi\pi\pi\pi\pi\pi\pi 00\pi\pi 0\pi 0\pi$ is obtained. By imposing this 26-bit binary sequence over certain wavelength range in the fundamental spectrum and blocking all other wavelengths outside such a range via amplitude shaping, maximum intensity at the frequency corresponding to the center of symmetry of the phase and minimum intensity everywhere else in $S^{(2)}(\omega)$ are obtained, exactly as required for selective TP excitation. Shifting the center of symmetry of the phase across the spectrum, the peak in $S^{(2)}(\omega)$ can be tuned. Following this approach, sixty BP-amplitude masks evenly spaced across the available fundamental spectrum bandwidth were imposed to the pulses to generate the same number of SHG spectra. Figure 5.5a shows two of the applied phases, while Figure 5.5b shows five SHG spectra. Dashed lines indicate the correspondence between two of the BPs and SHG spectra. Note that the peaks occur at the wavelength corresponding to the symmetry point of the BP. The SHG spectra corresponding to the whole set of BPs are shown in Figure 5.5c. The CR is ~1.5, but can be further improved following the procedure described in [31]. The FWHM of the peaks is ~1.8 nm. Therefore, the wavelength resolution in TPE spectra measurements is expected to increase using the BP shaping approach. By using a BP with more bits, the resolution can be reduced to ~1 nm, which corresponds to the optical resolution of a single SLM pixel [31]. Without MIIPS spectral phase correction, accurate delivery of the BPs and thus high-resolution second-order nonlinear excitation would be impossible.

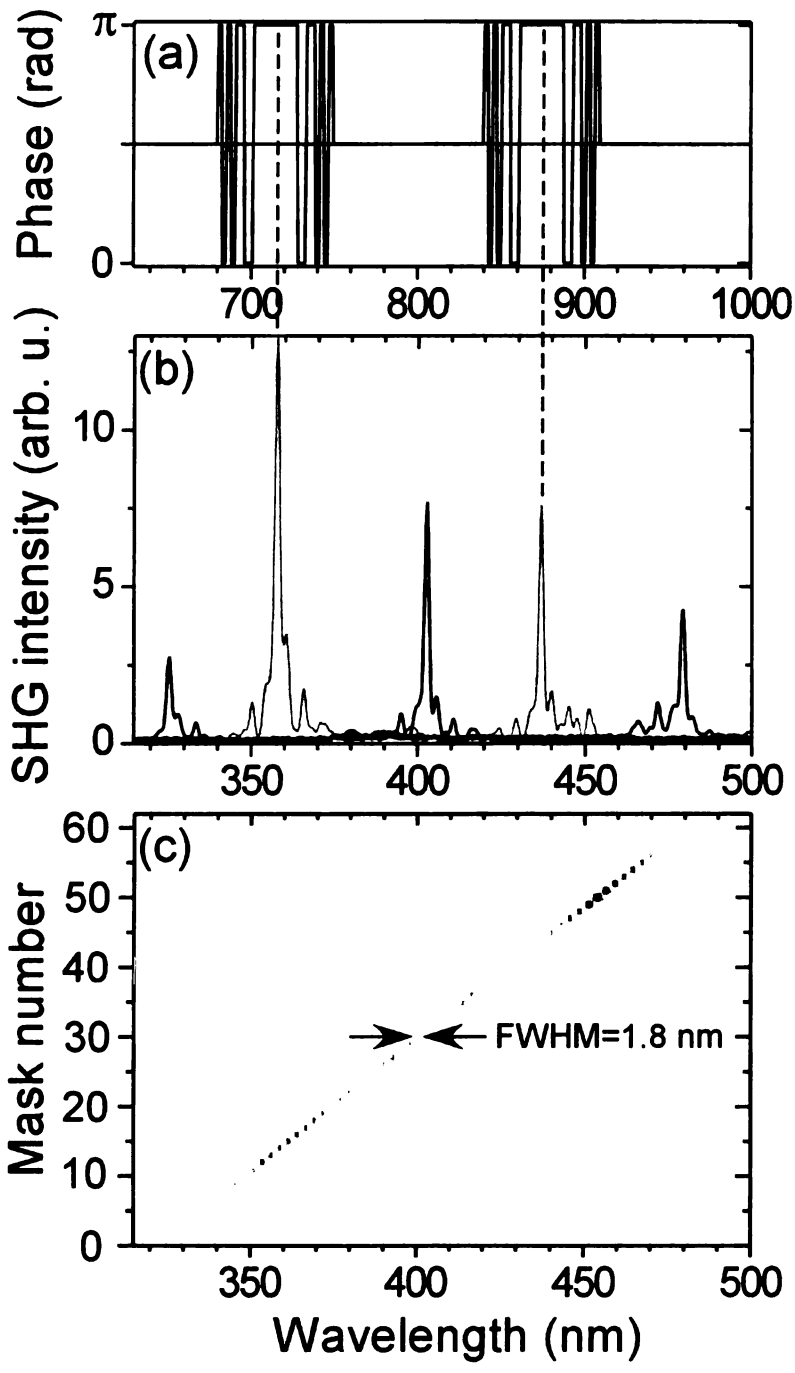

Figure 5.5. Selective two-photon excitation using binary phase shaping on ultrabroad-bandwidth femtosecond laser pulses. In this experiment the goal was to generate narrow-bandwidth second-order nonlinear spectra suitable for selective TP excitation. Sixty BP-amplitude masks evenly spaced across the fundamental spectrum of the pulses were used for such a purpose. (a) Two of the BPs. (b) Five of the narrow-bandwidth SHG spectra. The dashed lines indicate the correspondence between BPs and SHG spectra. (c) 2D contour plot showing the SHG spectra corresponding to the whole set of BP-amplitude masks

5.4. Conclusions

Selective TP excitation by Fourier-transform pulse shaping ultrabroad-bandwidth femtosecond laser pulses was successfully applied to TPE spectroscopy. This pulse shaping approach represents a valuable alternative to the conventional laser wavelength tuning method commonly employed to measure TPE spectra of fluorophores. The presented approach is fully automated given that no source wavelength tuning and hence no laser tweaking are required. Consequently, it is significantly faster and suitable for most potential interested users, who are not laser experts.

TPE spectra with ~5 nm resolution were obtained using amplitude shaping. Although this resolution is higher than that of most reported TPE spectra and sufficient for the majority of purposes, a phase-amplitude shaping approach based on minimum-autocorrelation binary phases expected to provide ~1 nm resolution was presented.

Chapter 6

Atmospheric pressure femtosecond laser desorption ionization imaging mass spectrometry

The content of this chapter, except section 6.3, has been adapted from Y. Coello, A. Daniel Jones, T. C. Gunaratne and M. Dantus. "Atmospheric pressure femtosecond laser imaging mass spectrometry". Anal. Chem. 82, 2753 (2010) [109].

A novel atmospheric pressure imaging mass spectrometry approach that offers improved lateral resolution (10 μm) using near-infrared femtosecond laser pulses for non-resonant desorption and ionization of sample constituents without the need of a laser-absorbing matrix is demonstrated. As a proof of concept the method was used to image a two-chemical pattern in paper. To demonstrate the ability of the approach to analyze biological tissue, a monolayer of onion epidermis was imaged allowing the chemical visualization of individual cells using mass spectrometry at ambient conditions for the first time. As the spatial resolution is currently limited by the limit of detection of the setup (~500 fmol limit of detection for citric acid), improvements in sensitivity will increase the achievable spatial resolution.

6.1. Introduction

Imaging mass spectrometry (IMS) [110, 111] has become an important tool in the life sciences because of its ability to localize specific analytes, from small metabolites to proteins, in biological samples. There are two different ways to obtain the spatial information in an IMS experiment. Typically a tightly focused ionization beam is used to examine a small region of the sample from where a mass spectrum is obtained. This process is repeated until the whole sample area has been analyzed and a mass spectrum

for each position has been stored. Chemical images can then be obtained from the set of mass spectra and the corresponding spatial coordinates. This approach, called microprobe mode, requires the sample to be probed point by point and therefore is relatively slow because it is limited by the rate of data acquisition and/or repetition rate of the laser beam. In addition, the spatial resolution is limited by the size of the focused ionization beam. Although much less popular than the microprobe mode a powerful approach that overcomes the previous limitations has been demonstrated. In the microscope mode [112, 113] the tightly focused ionization beam is replaced by one that illuminates a relatively large area of the sample (~200 μm), and ion detection is spatially resolved. However, the microscope mode can only be applied in vacuum conditions to preserve the ion trajectories from multiple locations in the sample to the detector.

Secondary ion mass spectrometry (SIMS) [114, 115] and matrix-assisted laser desorption/ionization (MALDI) [116, 117] are currently the most popular techniques used for obtaining chemically resolved images. In SIMS a beam of primary ions is used to bombard the sample surface and generate secondary ions. SIMS provides the highest spatial resolution available (typically >50 nm), however it has only proved useful for identifying elements and low mass molecules (*ca.* <1000 Da) because the ionization method leads to fragmentation that is more pronounced for higher mass analytes. SIMS requires vacuum conditions and is therefore, incompatible with the analysis of live cells and tissues. To analyze the distribution of macromolecules such as proteins ($1000 < m/z < 50\ 000$), ultraviolet (UV) MALDI remains the method of choice. This technique requires treating the sample with an external matrix that absorbs the radiation, which makes sample preparation a critical step. Most UV MALDI imaging experiments have been

performed under vacuum conditions providing typical spatial resolutions of 25-200 μm as limited by laser spot size and perturbation of analyte localization during matrix addition. Several atmospheric pressure (AP) ionization techniques have been developed in the past years to overcome incompatibility with the analysis of live tissues and other limitations imposed by a vacuum environment [118]. Some of these AP ionization techniques, laser ablation inductively coupled plasma (LA-ICP) [119, 120], laser ablation electrospray ionization (LAESI) [121, 122], infrared (IR) MALDI [123, 124], and desorption electrospray ionization (DESI) [125, 126] have already been applied to IMS. In contrast to the rest of these methods, LA-ICP does not provide molecular information and can only be used for elemental analysis of the sample because ICP is an atomic ion source. IR MALDI has employed a 2940 nm wavelength laser for both desorption and ionization of chemicals using the inherent water content present in biological samples as a matrix. LA-ICP and LAESI use a laser to ablate the sample while a postionization method, ICP and electrospray ionization (ESI) respectively, is employed to generate the ions. In LAESI the use of a postionization process following laser desorption (ablation) leads to higher ionization efficiencies compared to IR MALDI because laser ablation typically produces a significant proportion of neutral species in addition to ions and clusters. Although ink mock patterns have been analyzed with 40 μm spatial resolution using AP IR MALDI [123] and DESI [127], imaging biological samples at AP with a spatial resolution better than ~200 μm has not been reported yet.. A higher spatial resolution would be desirable, as it would allow studying, for instance, the distribution of chemicals in cellular and subcellular structures.

The spatial resolution of a laser ablation IMS experiment depends on the laser spot size and the step size [111], which is the distance the laser focal spot moves to analyze an adjacent sample location. Typically, the step size is larger than the laser spot and thus is the limiting factor in determining the lateral resolution of the imaging experiment. However, a step size smaller than the laser spot can be used in an approach known as oversampling [128]. This method requires complete removal of the analyte within the laser ablation volume by the desorption process or the use of data processing algorithms. With oversampling the step size becomes the limiting factor in determining the spatial resolution and is itself referred to as the pixel resolution of the experiment. In this situation, decreasing the step size leads to a higher spatial resolution but also to a smaller sampled volume and thus to lower signal. Using oversampling, an AP IR-MALDI chemical image of a dye mock pattern with 40 μm resolution has been demonstrated [123]. Recently, significant progress towards chemical imaging with cellular resolution has been reported using LAESI [129]. This experiment demonstrated *in situ* metabolic profiling of single large cells (~50 μm width) with a 2940 nm laser beam coupled to a glass fiber. However, no actual chemical image was presented.

Near IR (NIR) femtosecond laser pulses coupled with mass spectrometry have been used to demonstrate improved gas-phase molecular identification, including isomer differentiation [130, 131], and laser-controlled molecular fragmentation [28]. More recently, femtosecond-laser induced ionization/dissociation (fs-LID) of protonated peptides has been shown to provide greater sequence information than conventional ion activation methods [132]. Femtosecond laser pulses have also been used for ablation with ion-trap MS [133], LA-ICP [134], ESI [135] and as a postionization method for

molecular imaging after ion beam desorption [136] and laser ablation [137] of molecular thin films. MALDI experiments using femtosecond laser pulses in different wavelength regions have showed very similar results to those using nanosecond pulsed lasers [138]. NIR femtosecond laser (800 nm) MALDI mass spectra using standard matrices with absorption bands in the UV spectrum have been recently demonstrated [139]. However, due to the very high peak power densities achieved by focused femtosecond laser pulses ($\sim 10^{14}$ W/cm^2) direct non-resonant ablation and ionization of the analytes can occur [140]. Here we use such an approach for IMS at AP conditions. Focused NIR femtosecond laser pulses are used to ablate and ionize the sample without using a laser-absorbing matrix, either native or external, making sample preparation and handling significantly simpler. Due to its AP implementation the method is a promising imaging technique for *in vivo* studies. Finally, the spatial resolution provided by our AP femtosecond laser desorption ionization (fs-LDI) IMS approach is significantly higher than that of other AP IMS techniques. Here we demonstrate 10 μm spatial resolution in a biological tissue sample (onion epidermis monolayer) allowing the chemical visualization of individual cells using mass spectrometry under atmospheric pressure conditions for the first time.

6.2. Experimental section

6.2.1. Mass spectrometer and laser system

For these experiments we used the Ti:Sa regenerative amplifier and pulse shaper II, described in sections 2.1.2 and 2.2, respectively. The output pulses (1 kHz, centered at 800 nm) were focused on the sample using a 5X objective. The pulses were previously compressed using MIIPS, as described in section 3.2.2, to ensure efficient and

reproducible ablation and ionization within focal volume. As a result of MIIPS compression, 45 fs TL pulses were obtained at the focal plane after the objective.

For the "S" character, onion tissue and limit of detection experiments 3, 15 and 3 μJ pulses were used, respectively. The focused laser pulses had a spot diameter of ~20 μm, determined from the optical image of the ablation craters produced by the laser on the onion epidermis tissue. The ion source of a time-of-flight mass spectrometer (Micromass LCT, Waters) was replaced with a custom made AP femtosecond laser ion source containing a motorized XY stage (MAX200, Thorlabs) which holds the sample ~5 mm from the sample cone of the mass spectrometer. For the "S" character and limit of detection experiments a copper surface with a -200 V DC offset was used as a sample holder. For the onion tissue experiments the sample was free standing, only held to the XY stage from the upper edge. For all the experiments, the sample was positioned between the sample cone (±65V DC) and a repeller electrode (±1 kV DC) so that the potential difference helped to direct the ion plume toward the inlet (Figure 6.1), where the + and - signs apply for positive and negative ion mode experiments, respectively. The mass scale was calibrated periodically using MassLynx 4.1 software (Waters Corp.) and electrospray ionization of a commercial NaCsI solution (Waters Corp.). The accuracy of measured *m/z* values was better than 100 mDa over the studied range (*m/z*<500) over multiple days between calibrations.

6.2.2. Imaging

The motorized stage was computer-controlled to move the sample surface laterally. Mass spectra were averaged for ~2s for every spot on the sample and were stored as a function of time. Data acquisition for each imaging experiment took ~80 minutes. A

computer program then converted spectrum acquisition time to the corresponding spatial coordinates. Finally, chemical images were obtained by plotting two-dimensional distributions of the different chemical species. To obtain the optical images, the sample was illuminated with a USB-powered diode and the light collected by the objective was reflected by an 800 nm-transmitter / 400 nm-reflector and directed to a monochromatic CCD camera (Apogee Alta, Apogee Instruments, Inc.). A BG40 filter was placed before the CCD camera to block the remaining scattered laser light (Figure 6.1).

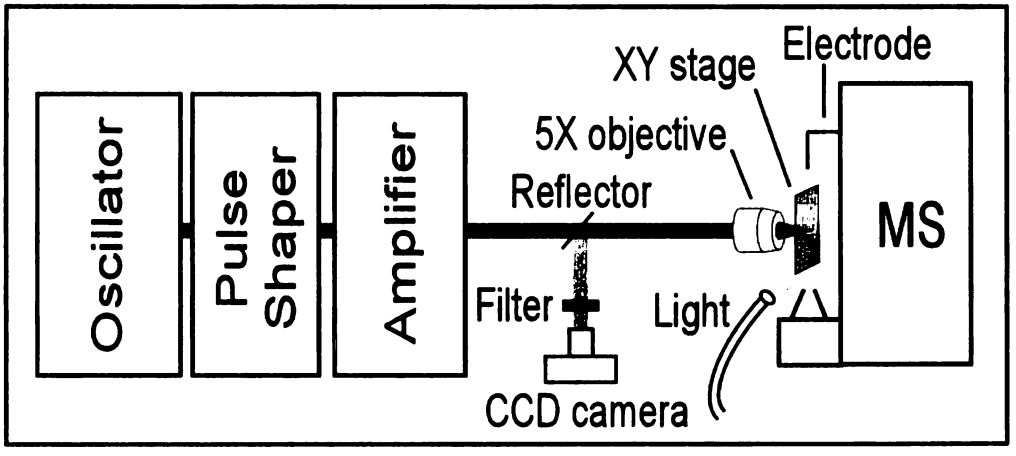

Figure 6.1. Atmospheric pressure femtosecond laser desorption ionization imaging mass spectrometry (AP fs-LDI IMS) setup. Femtosecond laser pulses from a Ti:Sa oscillator were regeneratively amplified and focused on the sample by a 5X objective. The pulse shaper was used to compress the pulses at the focus. The sample was placed on a motorized XY stage close to the sample cone of the mass spectrometer (MS) and a counter-electrode was used to direct the ions to the sample cone. To obtain the optical images the light illuminating the sample was collected by the objective and directed to a CCD camera. A filter before the camera was used to block the scattered laser light.

6.2.3. Materials and sample preparation

All solutions were prepared in deionized water. Citric acid (monohydrate) was purchased from J.T. Baker. The iodide/iodine dye solution was prepared by dissolving 10 mg of iodine and 175 mg of potassium iodide (Mallinckrodt) in 1 mL of water. For the "S" experiment the handwritten marks were produced on bond paper using a 0.25 mm

diameter wire. The paper sample was then glued to the copper sample holder and transferred to the translation stage. Fresh red onions were purchased from a local supermarket. Onion epidermis tissue sections were obtained with a razor blade, transferred to the translation stage and analyzed without any pretreatment. In the partially-stained tissue experiment, iodine/iodide dye was deposited on a region of an onion tissue section by a 0.25 mm diameter wire before transferring the sample to the translation stage. For the limit of detection experiment, 1 μL of an aqueous 10 mM solution of citric acid was deposited on the copper sample holder and the solution was allowed to dry under ambient conditions. The deposited material covered an area of ~6 mm^2.

6.2.4. Metabolite identification

Confirmations of metabolite annotation were performed on extracts (methanol:water, 1:1 v/v) of onion tissue (1.0 mL of solvent per 100 mg of tissue, wet weight) using an LCT Premier (Waters) mass spectrometer that was coupled to a Shimadzu LC-20AD ternary pump. Extracts were analyzed using negative mode ESI following separation on an Ascentis Express C18 column (2.1 x 50 mm, Supelco) using a gradient described previously [141]. Accurate mass assignments were aided by use of a lock mass reference (N-butylbenzenesulfonamide) and comparisons of retention times and ion masses to authentic standards (Sigma-Aldrich).

6.3. Optimization of ion source parameters and preliminary results

Initial experiments were aimed at detecting molecular or fragment ions from molecules in the gas phase. The pure solid or liquid was placed below the focal spot of the objective (Figure 6.1) so that the vapor diffused toward the focal volume. Several

compounds were used for this purpose, including 2-pentanone, 4-nitrotoluene and 2,4-dinitrotoluene. The intensity of the molecular ion peak was monitored to optimize the ion source geometry and several parameters. For instance, the alignment of the electrode and location of the focal spot were found to have a significant effect on ion transport from ion source to mass spectrometer. Optimal signal was observed when the electrode was aligned with the axis of the sample cone and the focal spot was placed on this axis. The following ion source parameters were also found to have a significant effect on ion transport. The set of values that provided optimal signal are indicated next.

Electrode: (±1000 V)

Sample cone: (±65 V)

Extraction cone: ±5 V

RF lens: 100 V,

where the + and - signs apply for positive and negative ion mode experiments, respectively. The values in parentheses were measured with a multimeter with respect to ground, but do not correspond to those indicated by the instrument, which had a different reference.

The source temperature was set to 80°C to reduce the formation of water clusters. The microchannel plate (MCP) detector voltage was set to the minimum voltage that provided optimum sensitivity, typically ~2750 V. In addition, the noise threshold (Stop) for the MCP detector was set to the maximum possible value that did not filter any chemical signal, typically ~20 mV.

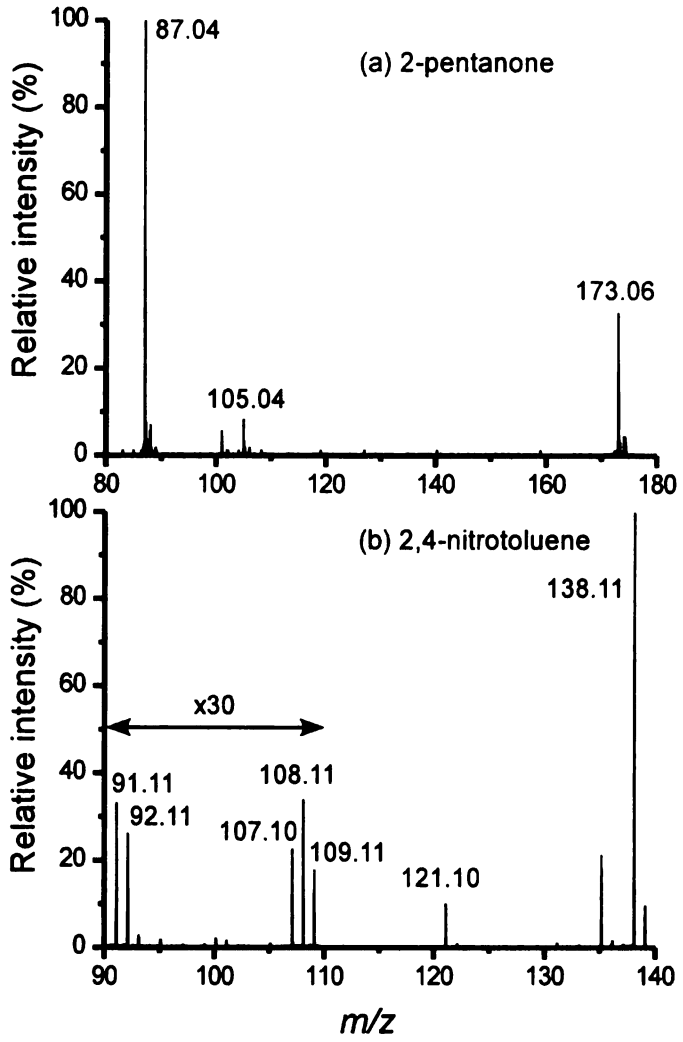

Figure 6.2. Atmospheric pressure femtosecond laser ionization mass spectra of molecules in the gas phase. (a) Mass spectrum of 2-pentanone in positive ion mode. The annotated peaks at *m/z* 87.04, 105.04 and 173.06 correspond to $[M+H^+]^+$, $[M+H^++H_2O]^+$ and $[2M+H^+]^+$ of pentanone. (b) Mass spectrum of 4-nitrotoluene in positive ion mode. The annotated peaks at *m/z* 91.11, 92.11, 107.10, 108.11, 109.11, 121.10 and 138.11 correspond to $[M-NO_2^-]^+$, $[M-NO_2+H^+]^+$, $[M-NO^-]^+$, $[M-NO+H^+]^+$, $[M-NO_2^-+H_2O]^+$, $[M-O^-]^+$ and $[M+H^+]^+$ of nitrotoluene.

The positive ion mode mass spectra of 2-pentanone and 4-nitrotoluene are shown as an example in Figures 6.2a and 6.2b, respectively. For these experiments, data were averaged over ~1 min. The annotated peaks were identified as molecular or fragment ions of the corresponding molecules. In Figure 6.2a the peaks at *m/z* 87.04, 105.04 and 173.06

correspond to $[M+H^+]^+$, $[M+H^++H_2O]^+$ and $[2M+H^+]^+$ of pentanone (theoretical monoisotopic *m/z* 87.09, 105.09 and 173.15, respectively). In Figure 6.2b the peaks at *m/z* 91.11, 92.11, 107.10, 108.11, 109.11, 121.10 and 138.11 correspond to $[M-NO_2^-]^+$, $[M-NO_2+H^+]^+$, $[M-NO^-]^+$, $[M-NO+H^+]^+$, $[M-NO_2^-+H_2O]^+$, $[M-O^-]^+$ and $[M+H^+]^+$ of nitrotoluene (theoretical monoisotopic *m/z* 91.05, 92.06, 107.05, 108.06, 109.07, 121.05 and 138.06, respectively).

A number of unexpected peaks frequently appeared in mass spectra (not shown) taken in positive ion mode even in the absence of a sample. Many of these peaks, appearing at *m/z* 149, 279 and 391, were found to come from the plasticizer bis-(2-ethylhexyl) phthalate, a common laboratory contaminant.

A sample holder was used for solid samples, as shown in Figure 6.1. No significant signal was observed unless a potential was applied to the holder. For this reason, a copper sample holder was used. For the ion source parameters given above, the optimal sample holder potential was found to be ±65 V, where the + and - signs apply for positive and negative ion mode experiments, respectively. Shorter distances between the tip of the electrode and the sample cone vertex (or longer electrodes, see Figure 6.1) were also found to increase the signal intensity. A ~1 cm distance was used to let sufficient space to move the sample during imaging experiments. Finally, different repulsive electrodes were evaluated including sharp pins and flat electrodes. While the optimal electrode voltage changed for the different electrodes, the maximum signal level did not vary significantly.

A first imaging experiment, shown in Figure 6.3, was performed with a set of tyrosine needles crystallized from a saturated solution of tyrosine in aqueous ammonia. The femtosecond laser desorption ionization mass spectrum showed the protonated

molecular ion $[M+H]^+$ at *m/z* 182.06 almost exclusively (theoretical monoisotopic *m/z* 182.08). The optical image of the sample was not taken given that no camera was available at that time.

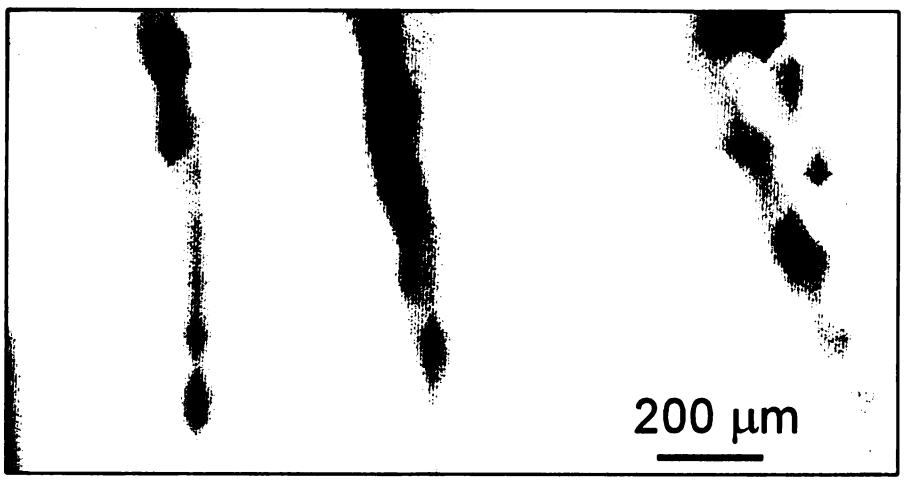

Figure 6.3. Chemical image of tyrosine crystals. The plot shows the distribution of *m/z* 182, the protonated molecular ion $[M+H]^+$. A step size of 50µm was used. The area imaged is about 1.7mm×0.9mm.

6.4. Results and discussion

The motivation for developing improved IMS instrumentation is to obtain chemical-species resolved images. In order to demonstrate this capability we analyzed an "S" character drawn with iodide/iodine dye. An optical image of the sample is shown in Figure 6.4a. Also present, although not visible in the optical image, is a diagonal mark across the "S" character produced with an aqueous ~5% (w/v) solution of citric acid. The mass spectrum of the dye showed the presence of peaks at *m/z* 126.91, 253.77 and 380.64 corresponding to I^-, I_2^- and I_3^-, respectively (theoretical monoisotopic *m/z* 126.90, 253.81 and 380.71, respectively). The spatial distribution of triiodide (*m/z* 380.64) shows excellent agreement with the "S" character, as shown in Figure 6.4b. The distribution of $[M-H]^-$ from citric acid (*m/z* 191.09, theoretical monoisotopic *m/z* 191.02) shows the

optically invisible diagonal mark drawn on the sample. The imaging experiment was performed using a step size of 25 μm under atmospheric conditions.

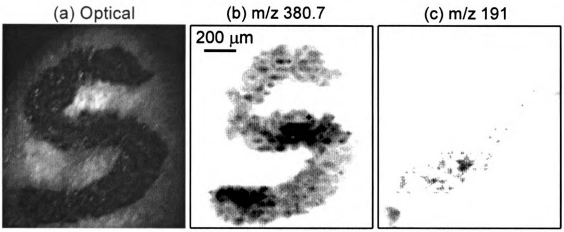

Figure 6.4. Chemical image of a dye pattern obtained under atmospheric conditions. (a) Optical image of the sample. The "S" character was drawn with iodine/iodide dye. Although not visible, a diagonal line drawn across the "S" with citric acid is also present in the sample. (b) The distribution of triiodide (*m/z* 380.64), which shows an excellent agreement with the "S" character. (c) The distribution of citrate (*m/z* 191.09), invisible in the optical image, shows the diagonal line drawn across the "S" character with citric acid. The step size is 25 μm.

Imaging biological samples is one of the most promising applications of IMS. We selected onion epidermis tissue, a classic sample in optical microscopy, to demonstrate the ability of our method to image biological samples with unprecedented spatial resolution at atmospheric pressure using mass spectrometry. This tissue was selected because it contains cells of appropriate sizes (~50 μm width) to be resolved with the current spatial resolution of our system. Figure 6.5 shows the laser-induced mass spectra in negative and positive ion modes obtained after a 100 μm step of the sample across the laser focal spot. The spectra show the presence of common plant metabolites. The peaks at *m/z* 179.05, 225.05, 341.09 and 387.10 in Figure 6.5a correspond to the $[M-H]^-$ of glucose (with possible contribution from other isomeric hexoses), $[M+formate]^-$ of

glucose, $[M-H]^-$ of sucrose, and $[M+formate]^-$ of sucrose. These assignments were

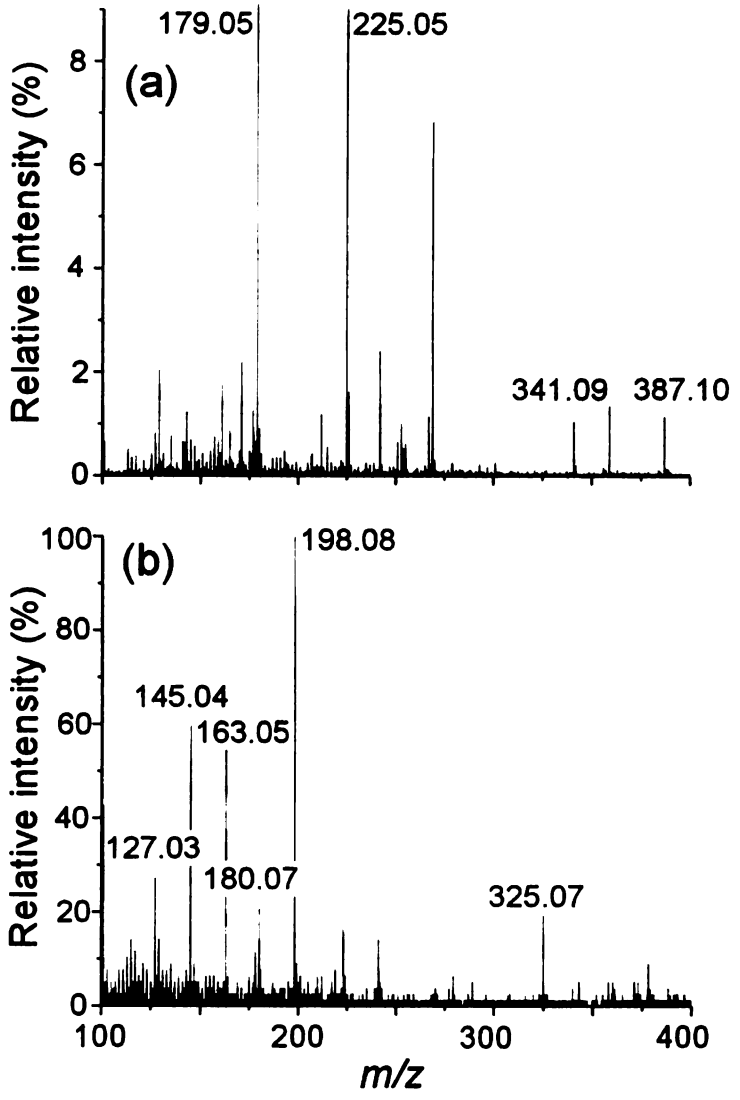

Figure 6.5. Mass spectra of onion epidermis tissue generated using femtosecond laser desorption ionization. Common plant metabolites were identified. (a) Negative ion mode. The annotated peaks at *m/z* 179.05, 225.05, 341.09 and 387.10 correspond to the $[M-H]^-$ of glucose, $[M+formate]^-$ of glucose, $[M-H]^-$ of sucrose, and $[M+formate]^-$ of sucrose, respectively. (b) Positive ion mode. The annotated peaks at *m/z* 127.03, 145.04, 163.05, 180.07, 198.08 and 325.07 are consistent with $[M+H^+-3H_2O]^+$ of glucose, $[M+H^+-2H_2O]^+$ of glucose, $[M+H^+-H_2O]^+$ of glucose, $[M+NH_4^+-H_2O]^+$ of glucose, $[M+NH_4^+]^+$ of glucose and $[M+H^+-H_2O]^+$ of sucrose, respectively.

confirmed by coincident retention times and accurate mass measurements from LC/MS analyses of onion extracts (see Metabolite identification) which detected glucose as a

minor constituent (*m/z* 179.0553, theoretical monoisotopic *m/z* 179.0561) and sucrose as an abundant metabolite (*m/z* 341.1078, theor. *m/z* 341.1089). In Figure 6.5b the peaks at *m/z* 127.03, 145.04, 163.05, 180.07, 198.08 and 325.07 are consistent with $[M+H^+-3H_2O]^+$ of glucose, $[M+H^+-2H_2O]^+$ of glucose, $[M+H^+-H_2O]^+$ of glucose, $[M+NH_4^+-H_2O]^+$ of glucose, $[M+NH_4^+]^+$ of glucose and $[M+H^+-H_2O]^+$ of sucrose (theor. *m/z* 127.04, 145.05, 163.06, 180.09, 198.10 and 325.11, respectively).

Imaging experiments were performed in the negative ion mode. Given that the width of the tissue cells in our experiments was ~50 μm, a resolution higher than ~20 μm was necessary to resolve individual cells. At these resolutions, obtained by decreasing the step size, only the peaks at *m/z* 179.06 and 225.06 were detected and both showed similar spatial distributions. To enhance chemical contrast, a portion of the sample was stained with an iodine/iodide dye which is commonly used to stain starch. Figure6.4a shows the optical image (false color) of the sample. The stained region of the sample appears at the lower right region and is slightly darker than the rest of the tissue. The horizontal mark at the lower left region was intentionally produced by ablating the tissue with the laser. Figures 6.6b and 6.6c correspond to chemical images obtained using a 15 μm step size. Figure 6.6b shows the spatial distribution of deprotonated glucose ions (*m/z* 179.06). Note that higher *m/z* 179 regions (darker blue) match the location of the cell walls in the tissue, and thus the glucose ions are probably produced by fragmentation of cellulose from the cell walls. The ablated region also appears clearly in the chemical image. The spatial distribution of triiodide (*m/z* 380.64), from the dye solution, is shown in Figure 6.6c and agrees well with the location of the stained region.

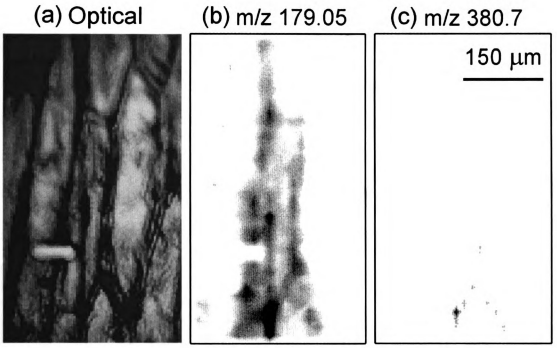

Figure 6.6. Chemical image of onion epidermis cells obtained under atmospheric conditions in negative ion mode. (a) Optical image (false color) of the tissue analyzed. The lower right region was partially stained with an iodine/iodide dye and appears slightly darker than the rest of the tissue. The horizontal mark was produced by ablating the tissue with the laser to determine the sampling width of the laser spot. (b) Chemical image of the same region showing the spatial distribution of deprotonated glucose (*m/z* 179.06). Note the excellent agreement with the optical image. (c) Chemical image of the same region showing the spatial distribution of triiodide (*m/z* 380.64). The step size for both chemical images was 15 μm.

The single pixel resolution of an experiment (step size) does not necessarily agree with the experimental spatial resolution of an image (the length scale that can be distinguished), which depends also on other factors such as the spatial distribution of analytes in the sample and the signal intensity per pixel [111]. A way to estimate the experimental spatial resolution is by examining a line across a feature of interest and measuring the distance required to move from 20% to 80% of the maximum intensity value of the feature [142]. To estimate the experimental spatial resolution of our system, we recorded another chemical image of onion epidermis using a 10 μm step size. Smaller step sizes compromised reproducibility of signal intensities across the sample in the

present configuration of our setup. Figure 6.7a shows the chemical image of the tissue showing the spatial distribution of *m/z* 179 (deprotonated glucose). The inset shows the corresponding optical image (false color). The experimental spatial resolution was calculated as ~10 μm from the analysis of several line scans across the image. An example of such line scans is shown as a red dashed line in Figure 6.7a and its corresponding intensity profile is shown in Figure 6.7b. To our knowledge, this is the highest spatial resolution chemical image obtained at AP conditions.

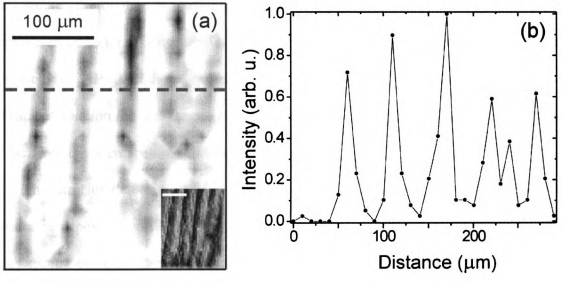

Figure 6.7. Chemical image of onion epidermis cells demonstrating the highest spatial resolution under atmospheric pressure conditions. (a) Chemical image generated in negative ion mode showing the spatial distribution of *m/z* 179 generated by probing the onion epidermis tissue. The inset shows the corresponding optical image. The scale bar in the inset is 100 μm. (b) Intensity distribution of *m/z* 179 corresponding to the red dashed line shown in (a). The analysis of several line scans such as the one shown indicated an experimental spatial resolution of ~10 μm.

The cell monolayers analyzed previously were completely ablated during the imaging experiment. However, the damage inflicted by the laser on thicker biological samples is superficial and most plant and animal tissue samples can survive the analysis. *In vivo* chemical imaging experiments are therefore possible with AP fs-LDI IMS.

While the identified peaks in the mass spectra of onion skin epidermis (Figure 6.5) likely correspond to cellulose fragments, the molecular ion is typically present in the AP fs-LDI mass spectrum of low molecular weight (<400 Da) solid samples of metabolite standards. The $[M-H]^-$ of the analyte is observed for acidic metabolites analyzed in negative ion mode such as in the case of citric acid. Similarly, the $[M+H]^+$ of the analyte is observed for molecules analyzed in positive ion mode such as tyrosine and 2,4-dinitrotoluene (not shown). The ionization of heavier molecules with AP fs-LDI has not been studied thoroughly, but molecular ions of molecules heavier than 400 Da have not been observed so far. As it is also suggested by the mass spectra shown in Figure 6.5 the ion yield of AP fs-LDI seems to decrease with increasing mass probably due to inefficient ablation for heavier fragments or inefficient transport of ions from the sample surface into the mass spectrometer using the present source configuration.

The limit of detection (LOD) of the method was calculated analyzing a layer of citric acid deposited on the sample holder (see Materials and sample preparation). The mass spectra corresponding to ten different laser spots (20 μm diameter) were averaged yielding a signal-to-noise ratio (S/N) of 5:1 for the citrate ion *(m/z* 191). Assuming that all the deposited material was ablated from the illuminated area, each laser spot would provide ~500 fmol of citric acid molecules. Other AP IMS techniques including DESI, LAESI and IR MALDI have limits of detection of a few fmol [121]. Note that in IR MALDI a laser-absorbing matrix present in high concentration resonantly absorbs the laser radiation [123]. In contrast, non-resonant laser-analyte interaction with no matrix occurs in fs-LDI. This difference may explain the higher LOD observed for fs-LDI. Laser desorption experiments have shown to produce a significant amount of neutrals together

with ions.[118, 121] Therefore, the introduction of a secondary ionization method such as ESI after laser desorption[121, 135] is expected to increase the ionization efficiency of fs-LDI. Additional improvements in the sensitivity of AP fs-LDI can be expected by optimizing several of the AP ion source parameters including the potentials on the sample cone, sample holder and electrode; and the distances between the electrode, sample holder, laser focal spot and sample cone. No effort was made here to synchronize the ion packets generated by the laser with the pusher pulses in the mass spectrometer. Such synchronization together with the use of an analog-to-digital converter, rather than the time-to-digital electronics in the current detection system offer opportunities to significantly increase the sensitivity and dynamic range of the method.

6.5. Conclusions

A novel IMS approach using near-IR femtosecond laser pulses for direct sample desorption and ionization at AP conditions has been presented. Given that ablation and ionization occur via nonlinear laser-analyte interactions the presence of a laser-absorbing matrix is not required. Consequently, sample preparation and handling are significantly simplified compared to AP MALDI IMS techniques.

In its current level of development AP fs-LDI IMS offers a limited *m/z* range (*m/z*<400) and sensitivity compared to other AP IMS techniques. Both figures of merit can be improved by adding a secondary ionization method following laser desorption to improve the ionization efficiency, by optimizing several of the AP ion source parameters to enhance ion collection, and by introducing ion packet-pusher pulse synchronization with new ADC detectors.

In contrast to the established vacuum IMS techniques MALDI and SIMS, AP fs-LDI IMS allows the analysis of biological samples in their natural state. Improvements in the sensitivity of the setup, as described before, will minimize damage to the sample and make *in vivo* investigations more feasible.

While no AP IMS technique can compete with SIMS imaging in terms of spatial resolution yet, the 10 μm spatial resolution for biological tissue demonstrated here with AP fs-LDI IMS represents an improvement over other AP IMS techniques and a step towards mass spectrometric chemical imaging at the cellular level. Efforts to increase resolution will also require improvements in the sensitivity in order to maintain an acceptable S/N. The resolution of the system could then be improved by reducing the laser focal spot diameter and the step size. The laser pulses used here can be focused to ~1 μm using a higher magnification objective. In theory, the smallest possible focal spot diameter would be determined by the diffraction limit ~λ/2, 400 nm in this case. Because the ionization and ablation processes produced by focused femtosecond pulses are highly nonlinear, it is conceivable that sub-diffraction-limit focal spot diameters could be ablated. This would allow, for instance, imaging subcellular structures.

References

(1) Zewail, A. H. *J. Phys. Chem. A* **2000**, *104*, 5660-5694.

(2) Franken, P. A.; Weinreich, G.; Peters, C. W.; Hill, A. E. *Phys. Rev. Lett.* **1961**, *7*, 118-&.

(3) Kaiser, W.; Garrett, C. G. B. *Phys. Rev. Lett.* **1961**, *7*, 229 LP - 231.

(4) Campagnola, P. J.; Loew, L. M. *Nat. Biotechnol.* **2003**, *21*, 1356-1360.

(5) Denk, W.; Strickler, J.; Webb, W. *Science* **1990**, *248*, 73-76.

(6) Diaspro, A.; Chirico, G.; Collini, M. *Quarterly Reviews of Biophysics* **2005**, *38*, 97-166.

(7) Xi, P.; Andegeko, Y.; Weisel, L. R.; Lozovoy, V. V.; Dantus, M. *Opt. Commun.* **2008**, *281*, 1841-1849.

(8) Albota, M. A.; Xu, C.; Webb, W. W. *Appl. Opt.* **1998**, *37*, 7352-7356.

(9) Makarov, N. S.; Drobizhev, M.; Rebane, A. *Opt. Express* **2008**, *16*, 4029-4047.

(10) Wollenhaupt, M.; Assion, A.; Baumert, T. In *Springer Handbook of Lasers and Optics*; Träger, F., Ed.; Springer: New York, 2007, pp 937-983.

(11) Walmsley, I.; Waxer, L.; Dorrer, C. *Rev. Sci. Instrum.* **2001**, *72*, 1-29.

(12) Broers, B.; Vandenheuvell, H. B. V.; Noordam, L. D. *Optics Communications* **1992**, *91*, 57-61.

(13) Broers, B.; Noordam, L. D.; Vandenheuvell, H. B. V. *Physical Review A* **1992**, *46*, 2749-2756.

(14) Meshulach, D.; Silberberg, Y. *Nature* **1998**, *396*, 239-242.

(15) Meshulach, D.; Silberberg, Y. *Physical Review A* **1999**, *60*, 1287-1292.

(16) Walowicz, K. A.; Pastirk, I.; Lozovoy, V. V.; Dantus, M. *J. Phys. Chem. A* **2002**, *106*, 9369-9373.

(17) Lozovoy, V. V.; Pastirk, I.; Walowicz, K. A.; Dantus, M. *Journal of Chemical Physics* **2003**, *118*, 3187-3196.

(18) Dela Cruz, J. M.; Pastirk, I.; Lozovoy, V. V.; Walowicz, K. A.; Dantus, M. *J. Phys. Chem. A* **2004**, *108*, 53-58.

(19) Lozovoy, V. V.; Dantus, M. *Chemphyschem* **2005**, *6*, 1970-2000.

(20) Shank, C. V.; Ippen, E. P. *Appl. Phys. Lett.* **1974**, *24*, 373-375.

(21) Maiman, T. H. *Nature* **1960**, *187*, 493-494.

(22) Fork, R. L.; Cruz, C. H. B.; Becker, P. C.; Shank, C. V. *Opt. Lett.* **1987**, *12*, 483-485.

(23) Moulton, P. F. *J. Opt. Soc. Am. B* **1986**, *3*, 125-133.

(24) Spence, D. E.; Kean, P. N.; Sibbett, W. *Opt. Lett.* **1991**, *16*, 42-44.

(25) Ell, R.; Morgner, U.; Kartner, F. X.; Fujimoto, J. G.; Ippen, E. P.; Scheuer, V.; Angelow, G.; Tschudi, T.; Lederer, M. J.; Boiko, A.; Luther-Davies, B. *Opt. Lett.* **2001**, *26*, 373-375.

(26) Binhammer, T.; Rittweger, E.; Ell, R.; Kartner, F. X.; Morgner, U. *IEEE J. Quantum Elect.* **2005**, *41*, 1552-1557.

(27) Coello, Y.; Lozovoy, V. V.; Gunaratne, T. C.; Xu, B. W.; Borukhovich, I.; Tseng, C. H.; Weinacht, T.; Dantus, M. *J. Opt. Soc. Am. B* **2008**, *25*, A140-A150.

(28) Lozovoy, V. V.; Zhu, X.; Gunaratne, T. C.; Harris, D. A.; Shane, J. C.; Dantus, M. *J. Phys. Chem. A* **2008**, *112*, 3789-3812.

(29) Strickland, D.; Mourou, G. *Optics Communications* **1985**, *56*, 219-221.

(30) Backus, S.; Durfee, C. G.; Murnane, M. M.; Kapteyn, H. C. *Rev. Sci. Instrum.* **1998**, *69*, 1207-1223.

(31) Lozovoy, V. V.; Xu, B. W.; Shane, J. C.; Dantus, M. *Physical Review A* **2006**, *74*.

(32) Ogilvie, J. P.; Debarre, D.; Solinas, X.; Martin, J. L.; Beaurepaire, E.; Joffre, M. *Opt. Express* **2006**, *14*, 759-766.

(33) Dantus, M.; Lozovoy, V. V. *Chemical Reviews* **2004**, *104*, 1813-1859.

(34) Lozovoy, V. V.; Dantus, M. *Annu. Rep. Prog. Chem., Sect. C: Phys. Chem.* **2006**, *102*, 227 - 258.

(35) Verluise, F.; Laude, V.; Cheng, Z.; Spielmann, C.; Tournois, P. *Opt. Lett.* **2000**, *25*, 575-577.

(36) Weiner, A. M. *Rev. Sci. Instrum.* **2000**, *71*, 1929-1960.

(37) Zeek, E.; Bartels, R.; Murnane, M. M.; Kapteyn, H. C.; Backus, S.; Vdovin, G. *Opt. Lett.* **2000**, *25*, 587-589.

(38) Zeek, E.; Maginnis, K.; Backus, S.; Russek, U.; Murnane, M.; Mourou, G.; Kapteyn, H.; Vdovin, G. *Opt. Lett.* **1999**, *24*, 493-495.

(39) Hillegas, C. W.; Tull, J. X.; Goswami, D.; Strickland, D.; Warren, W. S. *Opt. Lett.* **1994**, *19*, 737-739.

(40) Dugan, M. A.; Tull, J. X.; Warren, W. S. *J. Opt. Soc. Am. B* **1997**, *14*, 2348-2358.

(41) Weiner, A. M.; Leaird, D. E.; Patel, J. S.; Wullert, J. R. *IEEE J. Quantum Elect.* **1992**, *28*, 908-920.

(42) Weiner, A. M.; Leaird, D. E.; Patel, J. S.; Wullert, J. R. *Opt. Lett.* **1990**, *15*, 326-328.

(43) Wefers, M. M.; Nelson, K. A. *Opt. Lett.* **1995**, *20*, 1047-1049.

(44) Brixner, T.; Gerber, G. *Opt. Lett.* **2001**, *26*, 557-559.

(45) Oron, D.; Dudovich, N.; Silberberg, Y. *Phys. Rev. Lett.* **2003**, *90*.

(46) Brixner, T.; Krampert, G.; Pfeifer, T.; Selle, R.; Gerber, G.; Wollenhaupt, M.; Graefe, O.; Horn, C.; Liese, D.; Baumert, T. *Phys. Rev. Lett.* **2004**, *92*.

(47) Yelin, D.; Meshulach, D.; Silberberg, Y. *Opt. Lett.* **1997**, *22*, 1793-1795.

(48) Baumert, T.; Brixner, T.; Seyfried, V.; Strehle, M.; Gerber, G. *Appl. Phys. B-Lasers O.* **1997**, *65*, 779-782.

(49) Naganuma, K.; Mogi, K.; Yamada, H. *IEEE J. Quantum Elect.* **1989**, *25*, 1225-1233.

(50) Trebino, R.; Kane, D. J. *J. Opt. Soc. Am. A* **1993**, *10*, 1101-1111.

(51) Trebino, R. *Frequency-resolved optical gating : the measurement of ultrashort laser pulses*; Kluwer Academic: Boston, 2000.

(52) Iaconis, C.; Walmsley, I. A. *Opt. Lett.* **1998**, *23*, 792-794.

(53) Iaconis, C.; Walmsley, I. A. *IEEE J. Quantum Elect.* **1999**, *35*, 501-509.

(54) Baum, P.; Lochbrunner, S.; Gallmann, L.; Steinmeyer, G.; Keller, U.; Riedle, E. *Appl. Phys. B-Lasers O.* **2002**, *74*, S219-S224.

(55) Yamane, K.; Zhang, Z. G.; Oka, K.; Morita, R.; Yamashita, M.; Suguro, A. *Opt. Lett.* **2003**, *28*, 2258-2260.

(56) Miao, H. X.; Weiner, A. M.; Langrock, C.; Roussev, R. V.; Fejer, M. M. *Opt. Lett.* **2007**, *32*, 424-426.

(57) Dantus, M.; Lozovoy, V. V.; Pastirk, I. *OE Magazine* **2003**, *9*, 15-17.

(58) Lozovoy, V. V.; Pastirk, I.; Dantus, M. *Opt. Lett.* **2004**, *29*, 775-777.

(59) Xu, B. W.; Gunn, J. M.; Dela Cruz, J. M.; Lozovoy, V. V.; Dantus, M. *J. Opt. Soc. Am. B* **2006**, *23*, 750-759.

(60) Lozovoy, V. V.; Xu, B.; Coello, Y.; Dantus, M. *Opt. Express* **2008**, *16*, 592-597.

(61) Li, H.; Harris, D. A.; Xu, B.; Wrzesinski, P. J.; Lozovoy, V. V.; Dantus, M. *Opt. Express* **2008**, *16*, 5499-5504.

(62) Zhu, X.; Gunaratne, T. C.; Lozovoy, V. V.; Dantus, M. *Opt. Express* **2007**, *15*, 16061-16066.

(63) Baltuska, A.; Kobayashi, T. *Appl. Phys. B-Lasers O.* **2002**, *75*, 427-443.

(64) Yamashita, M.; Yamane, K.; Morita, R. *IEEE J. Sel. Top. Quant.* **2006**, *12*, 213-222.

(65) Xu, B. W.; Coello, Y.; Lozovoy, V. V.; Harris, D. A.; Dantus, M. *Opt. Express* **2006**, *14*, 10939-10944.

(66) Coello, Y.; Xu, B. W.; Miller, T. L.; Lozovoy, V. V.; Dantus, M. *Appl. Opt.* **2007**, *46*, 8394-8401.

(67) Toyran, S.; Liu, Y. M.; Singha, S.; Shan, S.; Cho, M. R.; Gordon, R. J.; Edward, D. P. *Exp. Eye Res.* **2005**, *81*, 298-305.

(68) Johnson, T. M.; Glaser, B. M. *Graefes Arch. Clin. Exp. Ophthalmol.* **2005**, *243*, 570-575.

(69) Wang, B. G.; Riemann, I.; Schubert, H.; Halbhuber, K. J.; Koenig, K. *Cell Tiss. Res.* **2007**, *328*, 515-520.

(70) Blum, M.; Kunert, K.; Nolte, S.; Riehemann, S.; Palme, M.; Peschel, T.; Dick, M.; Dick, H. B. *Ophthalmologe* **2006**, *103*, 1014-1019.

(71) Gerten, G.; Ripken, T.; Breitenfeld, P.; Krueger, R. R.; Kermani, O.; Lubatschowski, H.; Oberheide, U. *Ophthalmologe* **2007**, *104*, 40-46.

(72) Cain, C. P.; Thomas, R. J.; Noojin, G. D.; Stolarski, D. J.; Kennedy, P. K.; Buffington, G. D.; Rockwell, B. A. *Graefes Arch. Clin. Exp. Ophthalmol.* **2005**, *243*, 101-112.

(73) Siegman, A. E. *Lasers*; University Science Books: Mill Valley, CA, 1986.

(74) Daimon, M.; Masumura, A. *Appl. Opt.* **2007**, *46*, 3811-3820.

(75) Diddams, S.; Diels, J. C. *J. Opt. Soc. Am. B* **1996**, *13*, 1120-1129.

(76) Cohen, L. G. *J. Lightwave Technol.* **1985**, *3*, 958-966.

(77) Van Engen, A. G.; Diddams, S. A.; Clement, T. S. *Appl. Opt.* **1998**, *37*, 5679-5686.

(78) Harvey, A. H.; Gallagher, J. S.; Sengers, J. *J. Phys. Chem. Ref. Data* **1998**, *27*, 761-774.

(79) Quan, X. H.; Fry, E. S. *Appl. Opt.* **1995**, *34*, 3477-3480.

(80) Austin, R. W.; Halikas, G.; Scripps Institution of Oceanography: San Diego, 1976.

(81) Hammer, D. X.; Welch, A. J.; Noojin, G. D.; Thomas, R. J.; Stolarski, D. J.; Rockwell, B. A. *J. Opt. Soc. Am. A* **1999**, *16*, 2092-2102.

(82) Atchison, D. A.; Smith, G. *J. Opt. Soc. Am. A* **2005**, *22*, 29-37.

(83) Navarro, R.; Santamaria, J.; Bescos, J. *J. Opt. Soc. Am. A* **1985**, *2*, 1273-1281.

(84) Le Grand, Y. *Form and space vision*, Rev. ed.; Indiana University Press: Bloomington, 1967.

(85) Goppert-Mayer, M. *Ann. Phys.-Berlin* **1931**, *9*, 273-294.

(86) Ashfold, M. N. R.; Howe, J. D. *Annual Review of Physical Chemistry* **1994**, *45*, 57-82.

(87) Helmchen, F.; Denk, W. *Nat. Methods* **2005**, *2*, 932-940.

(88) Fisher, W. G.; Partridge, W. P.; Dees, C.; Wachter, E. A. *Photochem. Photobiol.* **1997**, *66*, 141-155.

(89) Kim, S.; Ohulchanskyy, T. Y.; Pudavar, H. E.; Pandey, R. K.; Prasad, P. N. *J. Am. Chem. Soc.* **2007**, *129*, 2669-2675.

(90) Kuimova, M. K.; Collins, H. A.; Balaz, M.; Dahlstedt, E.; Levitt, J. A.; Sergent, N.; Suhling, K.; Drobizhev, M.; Makarov, N. S.; Rebane, A.; Anderson, H. L.; Phillips, D. *Org. Biomol. Chem.* **2009**, *7*, 889-896.

(91) Oulianov, D. A.; Tomov, I. V.; Dvornikov, A. S.; Rentzepis, P. M. *Optics Communications* **2001**, *191*, 235-243.

(92) Sengupta, P.; Balaji, J.; Banerjee, S.; Philip, R.; Kumar, G. R.; Maiti, S. *Journal of Chemical Physics* **2000**, *112*, 9201-9205.

(93) Tian, P. F.; Warren, W. S. *Opt. Lett.* **2002**, *27*, 1634-1636.

(94) Xu, C.; Webb, W. W. *J. Opt. Soc. Am. B* **1996**, *13*, 481-491.

(95) Xu, C.; Guild, J.; Webb, W. W.; Denk, W. *Opt. Lett.* **1995**, *20*, 2372-2374.

(96) Kaatz, P.; Shelton, D. P. *J. Opt. Soc. Am. B* **1999**, *16*, 998-1006.

(97) Kapoor, R.; Friend, C. S.; Patra, A. *J. Opt. Soc. Am. B* **2003**, *20*, 1550-1554.

(98) Kauert, M.; Stoller, P. C.; Frenz, M.; Ricka, J. *Opt. Express* **2006**, *14*, 8434-8447.

(99) Ogilvie, J. P.; Kubarych, K. J.; Alexandrou, A.; Joffre, M. *Opt. Lett.* **2005**, *30*, 911-913.

(100) Isobe, K.; Suda, A.; Tanaka, M.; Kannari, F.; Kawano, H.; Mizuno, H.; Miyawaki, A.; Midorikawa, K. *Physical Review A* **2008**, *77*.

(101) Blab, G. A.; Lommerse, P. H. M.; Cognet, L.; Harms, G. S.; Schmidt, T. *Chem. Phys. Lett.* **2001**, *350*, 71-77.

(102) Huang, S. H.; Heikal, A. A.; Webb, W. W. *Biophysical Journal* **2002**, *82*, 2811-2825.

(103) *http://www.drbio.cornell.edu/cross_sections.html*.

(104) Dela Cruz, J. M.; Pastirk, I.; Comstock, M.; Lozovoy, V. V.; Dantus, M. *Proc. Natl. Acad. Sci. USA* **2004**, *101*, 16996-17001.

(105) Spry, D. B.; Goun, A.; Bell, C. B.; III; Fayer, M. D. *J. Chem. Phys.* **2006**, *125*, 144514.

(106) Comstock, M.; Lozovoy, V. V.; Pastirk, I.; Dantus, M. *Opt. Express* **2004**, *12*, 1061-1066.

(107) Lozovoy, V. V.; Shane, J. C.; Xu, B. W.; Dantus, M. *Opt. Express* **2005**, *13*, 10882-10887.

(108) *http://www.chemistry.msu.edu/faculty/dantus/merit_factor_records.html*.

(109) Coello, Y.; Jones, A. D.; Gunaratne, T. C.; Dantus, M. *Anal. Chem.* **2010**, *82*, 2753-2758.

(110) Heeren, R. M. A.; Smith, D. F.; Stauber, J.; Kukrer-Kaletas, B.; MacAleese, L. *J. Am. Soc. Mass Spectrom.* **2009**, *20*, 1006-1014.

(111) McDonnell, L. A.; Heeren, R. M. A. *Mass Spec. Rev.* **2007**, *26*, 606-643.

(112) Luxembourg, S. L.; Mize, T. H.; McDonnell, L. A.; Heeren, R. M. A. *Anal. Chem.* **2004**, *76*, 5339-5344.

(113) Luxembourg, S. L.; McDonnell, L. A.; Mize, T. H.; Heeren, R. M. A. *J. Proteome Res.* **2005**, *4*, 671-673.

(114) Boxer, S. G.; Kraft, M. L.; Weber, P. K. *Ann. Rev. Biophys.* **2009**, *38*, 53-74.

(115) Winograd, N. *Anal. Chem.* **2005**, *77*, 142A-149A.

(116) Franck, J.; Arafah, K.; Elayed, M.; Bonnel, D.; Vergara, D.; Jacquet, A.; Vinatier, D.; Wisztorski, M.; Day, R.; Fournier, I.; Salzet, M. *Mol. Cell. Proteomics* **2009**, *8*, 2023-2033.

(117) Cornett, D. S.; Reyzer, M. L.; Chaurand, P.; Caprioli, R. M. *Nat. Methods* **2007**, *4*, 828-833.

(118) Van Berkel, G. J.; Pasilis, S. P.; Ovchinnikova, O. *J. Mass Spectrom.* **2008**, *43*, 1161-1180.

(119) Becker, J. S.; Zoriy, M. V.; Pickhardt, C.; Palomero-Gallagher, N.; Zilles, K. *Anal. Chem.* **2005**, *77*, 3208-3216.

(120) Wu, B.; Zoriy, M.; Chen, Y. X.; Becker, J. S. *Talanta* **2009**, *78*, 132-137.

(121) Nemes, P.; Vertes, A. *Anal. Chem.* **2007**, *79*, 8098-8106.

(122) Nemes, P.; Barton, A. A.; Vertes, A. *Anal. Chem.* **2009**, *81*, 6668-6675.

(123) Li, Y.; Shrestha, B.; Vertes, A. *Anal. Chem.* **2007**, *79*, 523-532.

(124) Li, Y.; Shrestha, B.; Vertes, A. *Anal. Chem.* **2008**, *80*, 407-420.

(125) Wiseman, J. M.; Ifa, D. R.; Song, Q. Y.; Cooks, R. G. *Angew. Chem.-Int. Edit.* **2006**, *45*, 7188-7192.

(126) Wiseman, J. M.; Ifa, D. R.; Zhu, Y. X.; Kissinger, C. B.; Manicke, N. E.; Kissinger, P. T.; Cooks, R. G. *Proc. Natl. Acad. Sci. USA* **2008**, *105*, 18120-18125.

(127) Kertesz, V.; Van Berkel, G. J. *Rapid Commun. Mass Spectrom.* **2008**, *22*, 2639-2644.

(128) Jurchen, J. C.; Rubakhin, S. S.; Sweedler, J. V. *J. Am. Soc. Mass Spectrom.* **2005**, *16*, 1654-1659.

(129) Shrestha, B.; Vertes, A. *Anal. Chem.* **2009**, *81*, 8265-8271.

(130) Pastirk, I.; Zhu, X.; Lozovoy, V. V.; Dantus, M. *Appl. Opt.* **2007**, *46*, 4041-4045.

(131) Dela Cruz, J. M.; Lozovoy, V. V.; Dantus, M. *J. Mass Spectrom.* **2007**, *42*, 178-186.

(132) Kalcic, C. L.; Gunaratne, T. C.; Jones, A. D.; Dantus, M.; Reid, G. E. *J. Am. Chem. Soc.* **2009**, *131*, 940-942.

(133) Samek, O.; Margetic, V.; von Wiren, N.; Michels, A.; Niemax, K.; Hergenroder, R. *Appl. Phys. A-Mater. Sci. Process.* **2004**, *79*, 957-960.

(134) Fernandez, B.; Claverie, F.; Pecheyran, C.; Donard, O. F. X. *Trends Anal. Chem.* **2007**, *26*, 951-966.

(135) Brady, J. J.; Judge, E. J.; Levis, R. J. *Rapid Commun. Mass Spectrom.* **2009**, *23*, 3151-3157.

(136) Willingham, D.; Kucher, A.; Winograd, N. *Chem. Phys. Lett.* **2009**, *468*, 264-269.

(137) Savina, M. R.; Lykke, K. R. *Anal. Chem.* **1997**, *69*, 3741-3746.

(138) Papantonakis, M. R.; Kim, J.; Hess, W. P.; Haglund, R. F. *J. Mass Spectrom.* **2002**, *37*, 639-647.

(139) Wichmann, J. M.; Lupulescu, C.; Woste, L.; Lindinger, A. *Rapid Commun. Mass Spectrom.* **2009**, *23*, 1105-1108.

(140) Gamaly, E. G.; Rode, A. V.; Luther-Davies, B.; Tikhonchuk, V. T. *Phys. Plasmas* **2002**, *9*, 949-957.

(141) Schilmiller, A.; Shi, F.; Kim, J.; Charbonneau, A. L.; Holmes, D.; Jones, A. D.; Last, R. L. *The Plant Journal, "Accepted Article"; doi: 10.1111/j.1365-313X.2010.04154.x.*

(142) Colliver, T. L.; Brummel, C. L.; Pacholski, M. L.; Swanek, F. D.; Ewing, A. G.; Winograd, N. *Anal. Chem.* **1997**, *69*, 2225-2231.